Master of Science thesis

Investigating the drag sensitivity parameters and lateral dynamic response of a road vehicle in cross-wind flow

A.D. Fokker

December 2015

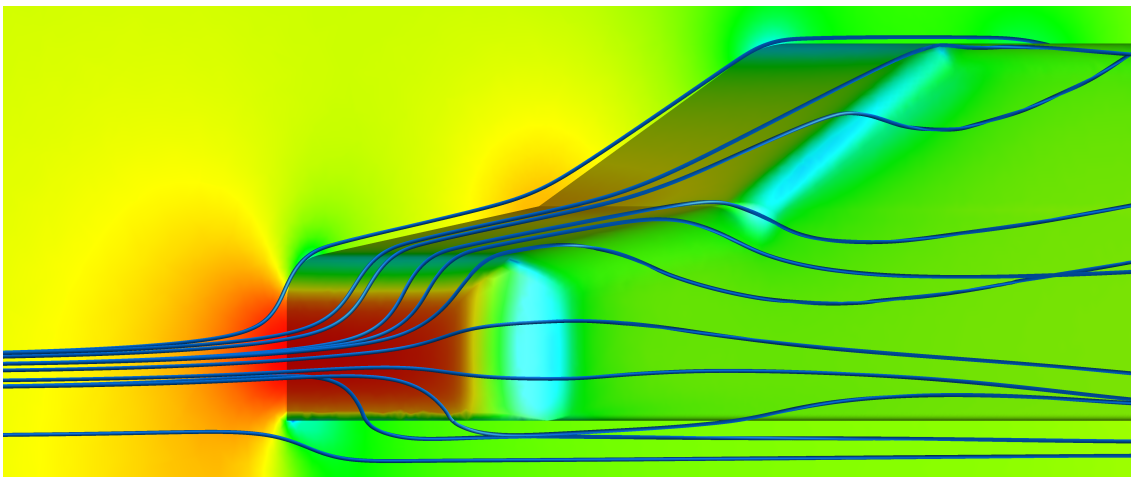

Faculty of Aerospace Engineering · Delft University of Technology

Investigating the drag sensitivity parameters and lateral dynamic response of a road vehicle in cross-wind flow

Master of Science thesis

For obtaining the degree of Master of Science in Aerospace Engineering at Delft University of Technology

A.D. Fokker

December 2015

Faculty of Aerospace Engineering · Delft University of Technology

Thesis registration number:
063 # 15 # MT # FPP

Delft University Of Technology
Department Of
Flight Performance and Propulsion

The undersigned hereby certify that they have read and recommend to the Faculty of Aerospace Engineering for acceptance a thesis entitled

"Investigating the drag sensitivity parameters and lateral dynamic response of a road vehicle in cross-wind flow"

written by

A.D. Fokker

in partial fulfillment of the requirements for the degree of **Master of Science**.

Dated: December 2015

Head of department: _____
Prof.dr.ir. L.L.M. Veldhuis

Supervisor: _____
Dr.ir. A.H. van Zuijlen

Reader: _____
Dr.ir. M. Voskuijl

Reader: _____
Dr.ir. M.A. Arat

Preface

Writing a Master thesis concludes the master "Flight Performance and Propulsion" at Delft University of Technology. First of all a thorough literature study needs to be performed in order to assess the current state of affairs in the specified research area. Within two months the author should be well aware of the available studies, after which the research objective is established.

The second and final stage of the master thesis comprises all the required research needed in order to answer the proposed research objective. The documentation of this part is published within this document. The author performed an internship within the California based company Tesla Motors, which designs and produces high-end electric vehicles. During this internship the first discussions started with the Aerodynamics design department staff members within this company, in order to explore the possibilities for performing a Master thesis research. Tesla's Aerodynamic design department has a strong interest in designing future vehicle models such that their dynamic and aerodynamic performance would be more robust while operating the vehicle in realistic cross-wind flows. The author has accepted this opportunity to enhance the aerodynamic performance of Tesla vehicles, within the framework of a Master of Science thesis.

The author would like to thank the supervisors Prof.dr.ir. L.L.M. Veldhuis, Dr.ir. A.H. van Zuijlen and Tesla's aerodynamic staff, Rob Palin, Luke Rebbeck and Andrew D'Hooge for their valuable discussions and this opportunity in general.

Daan Fokker, December 2015

Do what is worth the effort, with an enthusiasm that inspires

Summary

Recent trends in the automobile industry focus towards enhancing the operating efficiency of the road vehicle. One can achieve this by a combination of increasing the powertrain efficiency, reducing the weight and increasing the aerodynamic performance. The scope of this study is on the latter, i. e. enhancing the aerodynamic performance.

Most cars are optimized for minimum drag in idealized conditions, driving engineers to design for *the test* rather than for to optimize for actual flow encountered in real world conditions. These realistic conditions include (un)steady cross-wind flows encountered by the vehicle, rather than a perfectly aligned flow as is the case in an idealized situation. Different researchers studied the effect of these real world conditions on the performance of a vehicle. Many of these studies focussed upon the vehicle stability rather than the potential to reduce aerodynamic drag. This is because typical drag reducing means (such as radiused edges) tend to have a detrimental effect on the cross-wind stability and comfort of the vehicle.
The introduction of the fully electric Tesla Model S created new opportunities within this conception. This 2500 kg vehicle has an 800 kg battery underneath the car, which results in a different - relatively flexible - position of the center of gravity, total mass and corresponding mass moments of inertia.

As a result it is questioned if this difference in vehicle specifications allow for drag reducing shape modifications on a vehicle which is then still stable during cross-wind flows. After a careful trade-off it was chosen to use the recently launched open-source CFD software suite SU^2 in order to find an answer to the following research objective:

What design modifications reduce the drag coefficient of a simplified vehicle model which experiences a cross-wind flow, and how does this affect the lateral dynamic performance?

An interesting follow-up question on this would be to identify which design variables are (most) sensitive to drag increments in realistic crosswind flows. This document describes the process of solving the research objective within the framework of a Master of Science thesis.

A thorough vehicle dynamics study was performed in order to assess the most influential parameters which affect the lateral deviation of a vehicle. Within this study it was found that the cross-wind induced lateral deviation with a longitudinal velocity of $30m/s$ and a cross-wind flow of $3.15m/s$ or 6 degrees is roughly similar to the situation where the steering wheel angle is set to 1 degree. This implies that the lateral deviation during cross-wind flows is not much of an issue during steady cross-wind flows of up to 6 degrees.

Experiments were designed for three different cross-wind flows; 0 degrees, 3 degrees and 6 degrees cross-wind flow for both conventional and electric vehicles. The most important findings are summarized within table 1, where the C_D reduction reflects the cross-wind flow averaged (0°, 3°, 6°) reduction of the drag coefficient.

Design modification	**Unit**	**Initial value**	**Proposed value**	C_D **reduction**
Arrowing angle	[degrees]	0	15	5%
Tapering angle	[degrees]	0	15	27%
Tumblehome angle	[degrees]	0	15	10%
Front window angle	[degrees]	30	25	2%
Rear window angle	[degrees]	25	15	16%
A-pillar radius	[m]	0.10	0.15	4%
C-pillar radius	[m]	0.15	0.15	0%

Table 1: Summary on the effect of different design modifications on the drag coefficient

When these design modifications are simultaneously applied it was found that the drag coefficient is reduced by 17% for symmetric flow conditions, and as much as 43% during 6 degrees during cross-wind flow conditions.

Contents

Preface iv

Summary vii

List of Figures xiv

List of Tables xvi

Introduction 1

I Bluff body aerodynamics 5

1 Introduction to vehicle (aero)dynamics 7
- 1.1 Forces and moments upon a vehicle . . . 11
- 1.2 Crosswind flow phenomena and sensitivity . . . 14
- 1.3 Vehicle dynamics during cross-wind flows . . . 17

2 Principles of experimental and numerical methods 19
- 2.1 Computational Fluid Dynamics . . . 19
- 2.2 Windtunnel experiments . . . 21
- 2.3 Road testing . . . 22

3 CFD software 23
- 3.1 CFD Software suites . . . 23
- 3.2 Pre-processing the simulation . . . 24
- 3.3 Solving the system . . . 26

3.4 Selecting CFD software . . . 27
3.5 Stanford University Unstructured . . . 28
3.6 Validating the CFD software . . . 32

II Vehicle Dynamics **35**

4 Vehicle dynamics model **37**
4.1 Introduction to vehicle dynamics . . . 37
4.2 Governing equations of motion . . . 43
4.3 Vehicle mass moments of inertia . . . 46
4.4 Implementation in MATLAB . . . 48
4.4.1 Main: Run me . . . 48
4.4.2 Simulations . . . 49
4.4.3 Movements . . . 51

III Results **53**

5 Results **55**
5.1 Reference vehicle simulations . . . 56
5.2 Vehicle dynamics sensitivity study . . . 70
5.3 Arrowing the vehicle front end . . . 79
5.4 Tapering of the vehicle rear end . . . 85
5.5 Variations of the tumblehome angle . . . 90
5.6 Variations of the front window angle . . . 92
5.7 Variations of the rear window angle . . . 94
5.8 Variations of the A-pillar radius . . . 98
5.9 Variations of the C-pillar radius . . . 100
5.10 Towards an optimized vehicle geometry . . . 104

IV Synthesis **107**

6 Conclusions and recommendations **109**

V Appendices **113**

Appendix A: ANSYS Meshing **115**

References **123**

List of Figures

1 Preliminary workflow indicating the validation and analysis phase. . 4

1.1 Rotational viscous - and inviscid irrotational regions around a bluff body [46] 7
1.2 Velocity profiles of different boundary layer states [46] 9
1.3 Typical regions of separated and reattached flow [23] 10
1.4 Reference frame for vehicles as will be used in this study 11
1.5 Visualization of the ground effect at different distances from the ground 13
1.6 Resultant incoming flow vector V_A in a cross-wind environment of angle β 14
1.7 Three predominant effects of a crosswind flow upon a vehicle [18] . 15
1.8 Notchback (L), fastback (M) and a estate back vehicle (R). Courtesy of Ford 16
1.9 Visualization of 7 important vehicle dynamics definitions for a typical car [35] 17
1.10 Subjective comfort rating for different configurations during cross-winds [35] 18

2.1 FKFS Aero-acoustic wind tunnel of University of Stuttgart. P = 3200 kW [53] 21

3.1 Overview of available mathematical flow models [20] 26
3.2 Onera M6 testcase within the SU^2 environment 31
3.3 The SAE Reference vehicle is used for validation of the CFD software 32
3.4 The SAE Reference vehicle within the digital domain 33
3.5 Close-up of the SAE Reference vehicle in the digital domain 33
3.6 SAE Reference vehicle surface pressure distribution 34

4.1 SAE Vehicle fixed reference frame 38
4.2 Trajectory of a vehicle within the Earth fixed reference frame 38
4.3 The traditional 2 DOF bicycle model is used as basis [5] 43
4.4 Free body diagram of the vehicle 44
4.5 Vehicle inertia CAD model - Conventional (L), Electric (M), 3D view (R) 46
4.6 Vehicle dynamics MATLAB model structure 48

5.1 Reference vehicle geometry 57
5.2 3D view of the mesh 59
5.3 Detailed view of the mesh at the XZ-plane 59
5.4 0, 3 and 6 degrees pressure coefficient plots on the leeside front of the vehicle 61
5.5 Stream traces aft of the vehicle inside the vehicle wake 62
5.6 Pressure contours along the ZX - plane of the control volume 63
5.7 Skin friction distribution on the vehicle front during 3 different cross-wind flow angles 64
5.8 Skin friction distribution rear of the vehicle during 3 different cross-wind flow angles 66
5.9 Lateral displacement of electric and conventional vehicles moving at $30m/s$ during 0, 3 and 6 degrees of cross-wind flow 67
5.10 Vehicle dynamics log of three reference vehicles moving at 30m/s . . 68
5.11 Discrepancy in trajectories between reference and C_S set to zero . . 71
5.12 Discrepancy in trajectories between reference and C_{Mz} set to zero . 71
5.13 Electric vehicle trajectories where the vehicle weight is reduced and enhanced by 50% 72
5.14 Electric vehicle trajectories where the longitudinal position of the center of gravity is reduced and enhanced by 10% 73
5.15 Electric vehicle trajectories where the longitudinal position of the center of gravity is reduced and enhanced by 20% 74
5.16 Electric vehicle trajectories with different longitudinal velocities - 1.58 and $3.15m/s$ cross-wind 75
5.17 Conventional vehicle trajectories with different longitudinal velocities - 1.58 and $3.15m/s$ cross-wind 76
5.18 Izz trajectories 77
5.19 Arrowing modification performed on the vehicle front end 79
5.20 Surface pressure (left, center) and skin friction (right) distribution plots of 4 different arrowing configurations during 6° cross-wind flow 81
5.21 Electric vehicle trajectories with arrowing during 0°, 3° and 6° cross-wind 82
5.22 Conventional vehicle trajectories with arrowing during 0°, 3° and 6° cross-wind 82

5.23 Averaged (0°, 3° and 6° cross-wind) yaw moment - and side force coefficient versus averaged drag coefficient 83
5.24 Arrowing has a positive effect on the drag coefficient and lateral displacement for electric cars 84
5.25 Arrowing has a positive effect on the drag coefficient, and combined effect on the lateral displacement for conventional cars 84
5.26 Tapering modification performed on the vehicle rear end 85
5.27 Pressure plots of 4 different tapering configurations during 0° cross-wind flow 86
5.28 Pressure plots of 4 different tapering configurations during 6° cross-wind flow 88
5.29 Drag coefficient and lateral displacement improvement due to tapering electro 89
5.30 Drag coefficient and lateral displacement improvement due to tapering ICE 89
5.31 Tumblehome angle applied on the simplified vehicle geometry . . . 90
5.32 Drag coefficient and lateral displacement improvement due to tumblehome modifications applied to an electric vehicle 91
5.33 Drag coefficient and lateral displacement improvement due to tumblehome modifications applied to a conventional vehicle 91
5.34 Front window angle variations on the simplified vehicle geometry . . 92
5.35 Drag coefficient and lateral displacement improvement on electric vehicles due to front window angle variation 93
5.36 Drag coefficient and lateral displacement improvement on conventional vehicles due to front window angle variation 93
5.37 Rear window slant angle variations on the simplified vehicle geometry 94
5.38 Pressure plots of 3 rear window configurations during 0° cross-wind flow 95
5.39 Pressure plots of 3 rear window configurations during 6° cross-wind flow 96
5.40 Drag coefficient and lateral displacement improvement due to rear window angle variation electric 97
5.41 Drag coefficient and lateral displacement improvement due to rear window angle variation conventional 97
5.42 A-pillar radius applied the simplified vehicle geometry 98
5.43 Drag coefficient and lateral displacement improvement due to A-pillar radius variation for electric vehicles 99
5.44 Drag coefficient and lateral displacement improvement due to A-pillar radius variation for conventional vehicles 99
5.45 C-pillar radius applied the simplified vehicle geometry 100
5.46 Surface pressure and skin friction distribution plots of 3 different C-pillar radii - 0° cross-wind flow 101
5.47 Surface pressure and skin friction distribution plots of 3 different C-pillar radii during 6° cross-wind flow 102

5.48 Drag coefficient and lateral displacement improvement due to C-pillar radius variation for electric vehicles 103
5.49 Drag coefficient and lateral displacement improvement due to C-pillar radius variation for conventional vehicles 103
5.50 Proposed iteration of the vehicle geometry with various shape modifications 104
5.51 Surface pressure and skin friction distribution plots of both the reference and optimized vehicle during 6° cross-wind flow 105
5.52 Reference and optimized vehicle trajectories with arrowing during 0° and 6° cross-wind flows 106

6.1 Model of the Tesla geometry inside ANSYS Meshing 115
6.2 Digital control volume with the vehicle geometry inside 116
6.3 Meshing control settings used in ANSYS Meshing 117
6.4 Result of the mesh 120
6.5 Implementing a body of influence for local higher resolution of the mesh 121

List of Tables

1 Summary on the effect of different design modifications on the drag coefficient . . . viii

2.1 Advantages and disadvantages for using CFD software . . . 20
2.2 Advantages and disadvantages for wind tunnel systems . . . 21
2.3 Advantages and disadvantages for road testing . . . 22

3.1 Considered options for CFD software . . . 28
3.2 Validating SU^2 by comparing results with Toppinga's study . . . 33
3.3 Mesh dependance study results . . . 34

4.1 Combustion vehicle mass moment of inertia breakdown . . . 47
4.2 Electric vehicle mass moment of inertia breakdown . . . 47
4.3 Available ODE solvers within MATLAB . . . 50

5.1 Baseline geometry metrics . . . 58
5.2 Aerodynamic force and moment coefficients for different cross-wind flows . . . 66
5.3 When the cross-wind velocity is kept fixed, the incident cross-wind flow angle changes with longitudinal velocity . . . 75
5.4 Aerodynamic metrics for different arrow angles - 0° cross-wind flow 79
5.5 Aerodynamic metrics for different arrow angles - 6° cross-wind flow 80
5.6 Aerodynamic metrics for different taper angles - 0° cross-wind flow 85
5.7 Aerodynamic metrics for different taper angles - 6° cross-wind flow 87
5.8 Aerodynamic metrics for different tumblehome angles - 0° cross-wind flow . . . 90
5.9 Aerodynamic metrics for different tumblehome angles - 6° cross-wind flow . . . 91

5.10 Aerodynamic metrics for different front window angles - 0° cross-wind flow . . . 92
5.11 Aerodynamic metrics for different front window angles - 6° cross-wind flow . . . 92
5.12 Aerodynamic metrics for different rear window angles - 0° cross-wind flow . . . 94
5.13 Aerodynamic metrics for different rear window angles - 6° cross-wind flow . . . 95
5.14 Aerodynamic metrics for different A-pillar radii - 0° cross-wind flow 98
5.15 Aerodynamic metrics for different A-pillar radii - 6° cross-wind flow 98
5.16 Aerodynamic metrics for different C-pillar radii - 0° cross-wind flow 100
5.17 Aerodynamic metrics for different C-pillar radii - 6° cross-wind flow 102
5.18 Optimized geometry optimal values with a drag weight factor of 0.5 104
5.19 Aerodynamic metrics for the reference vehicle and the optimized vehicle during 0° cross-wind flow . . . 105
5.20 Aerodynamic metrics for the reference vehicle and the optimized vehicle during 6° cross-wind flow . . . 105

6.1 Summary on the effect of different design modifications on the drag coefficient . . . 110

Introduction

The automobile has established a very important role in today's world. It allows people to be mobile, and forms a vital condition for our current economy. Recent trends in the automobile world focus greatly on enhancing the operating efficiency such that the use of fossil fuels can be limited, resulting in lower costs and a healthier environment. There are many options being evaluated nowadays in order to achieve this goal, which extend many disciplines. The most obvious aspect of a vehicle to consider is the powertrain. Among others, these are higher efficiency internal combustion engines, (plug-in) hybrid powertrains, but also hydrogen - and fully electric powertrains. Reducing the total weight of the vehicle is also an effective way for reducing the required energy to operate a vehicle, and therefore increasing the operating efficiency. Another very important discipline which allows for an enhanced operating efficiency is the aerodynamic design of the vehicle, because during cruise conditions the only forces that need to be overcome by the power train are the rolling resistance and the aerodynamic drag.

One could argue that from a technical point of view, it would be optimal to have a vehicle which has a minimal resistive force to motion, and zero emissions. The vehicle should also be safe, and should require no maintenance and be available and affordable for everyone. In today's world however, this would be unrealistic to pursue. There are however some companies that push harder than others in order to reach this goal. One of these companies is Tesla Motors, founded in 2003 as a spin-off company from Stanford University's solar race car team. Over the last decade the company designed and built over 30.000 fully electric Tesla vehicles, and powertrains for e.g. Daimler and Toyota. Depending upon the power source of the charging station, Tesla Motors' vehicles feature arguably one of the least emitting mass-production powertrains currently available. On top of this, the latest design was awarded "Highest safety rating ever tested". It is possible to travel up to 500 kilometres on a single charge, and the only periodic maintenance required are new tires. An important aspect of current Tesla Motors vehicles is that the initial purchase price is high, starting from €66.000, but can exceed €120.000 [43]. The shift towards a less expensive Tesla vehicle will inherently implicate a battery pack with a smaller energy capacity, because of the high individual cell cost. In order to still achieve a high range of at least 500 kilometers the need for a high operating efficiency is important. Because an electric powertrain is already very efficient, reducing aerodynamic drag could yield a more substantial improvement.

Most road cars are optimized for minimal drag in idealised conditions, and cross-wind flow is only really considered with respect to vehicle stability.[43] Part of the reason for this is that the means by which aerodynamic efficiency is ultimately evaluated relies on the quantification of a road load curve under calm wind conditions. This drives engineers to design for the test, but this does not necessarily yield the best performance for the aerodynamic conditions the vehicle is likely to experience in service. The aerodynamic contribution to the real world performance of the vehicle is magnified due to the fact that it is directly related to the range of the vehicle. The aerodynamic contribution to the real world performance of the vehicle is magnified due to the fact that it is directly related to the range of the vehicle. Because charging a battery is not always as easy as refuelling, enhancing the range is crucial for mass implementation of the electric vehicle. This makes it even more important to consider the influence of various factors from the natural wind environment on the behaviour of the vehicle.

Tesla Motors has been investigating the effects of realistic free-stream turbulence on the aerodynamic characteristics of the vehicle, and discovered that there is a commonality between the design solutions for optimal performance in both turbulent and steady cross-wind flow fields. Here turbulence can be interpreted as a reduced timescale of the cross-wind flow condition, where each individual design feature on the car is temporarily immersed in each of a range of cross-wind flow angles. The vehicle may for example experience air approaching sequentially at +5 degrees, then -2 degrees, in a random distribution. The suggestion is that by optimizing the vehicles features in this highly turbulent flow, the design solutions are the same as if they had been tested in steady-state cross-wind flow. The general conclusion on optimizing a vehicle geometry for cross-wind flow is that any drag reducing solutions, such as radiused edges of an "A-pillar" tend to decrease the vehicle's stability beyond satisfaction. For electric vehicles this effect could be different than conventional cars since both the position of the center of gravity is lower, as well as a higher total weight. This is because of the presence of a battery which is generally located underneath the vehicle, which is typically much heavier (up to $800kg$) than a conventional powertrain. These different mass properties for electric cars require further investigation in order to justify the efforts for the end goal, i.e. further reducing the aerodynamic drag in realistic conditions, where the vehicle stability is included in the trade-off.

Project scope and research objective

This report contains the documentation of the study towards the following research objective: *What design modifications reduce the drag coefficient of a simplified vehicle model which experiences a cross-wind flow, and how does this affect the lateral dynamic performance?* The project is decomposed into four predominant parts, which together form the structure for this thesis in order to meet the research objective:

1. Bluff body aerodynamics
2. Vehicle Dynamics
3. Results
4. Synthesis

The flow field around the vehicle results which are discussed in part I eventually into aerodynamic forces and moments. These forces and moments can be used in order to assess the vehicle response in terms of vehicle dynamics, as is described in part II. Within this part the vehicle dynamic theory is discussed together with an outline for a custom design tool which is used for assessing the vehicle dynamic response. In order to achieve the research objective there are a number of subquestions which breaks down the problem, which allows for selecting an useful methodology and aid in the project planning.

Research subquestions

The subquestions are divided into two sets; the first set contains questions that concern with Aerodynamics, and the second set lists questions that refer to Vehicle Dynamics. The Aerodynamics related questions include the following:

- What will be the baseline geometry of the vehicle shape?
- What simplifications can be applied which yield useful results?
- Which design modifications are proposed in order to reduce the drag?
- What is the influence of the mesh density and domain size?
- What is the influence of the different options within the CFD software suite?
- What is the cross-wind flow spectrum that needs to be simulated?

The second set research subquestions applies to vehicle dynamics:

- What are the input and output requirements for the vehicle dynamics tool?
- What simplifications can be applied which yield useful results?
- What will be the stability criterions?
- What vehicle parameters such as mass moments of inertia will be used?
- Which suspension settings (such as roll stiffness and damping) will be employed?

Methodology

The research objective and the corresponding subquestions are combined in order to propose a preliminary methodology which is presented in figure 1. There are two predominant phases; the validation and the analysis phase.

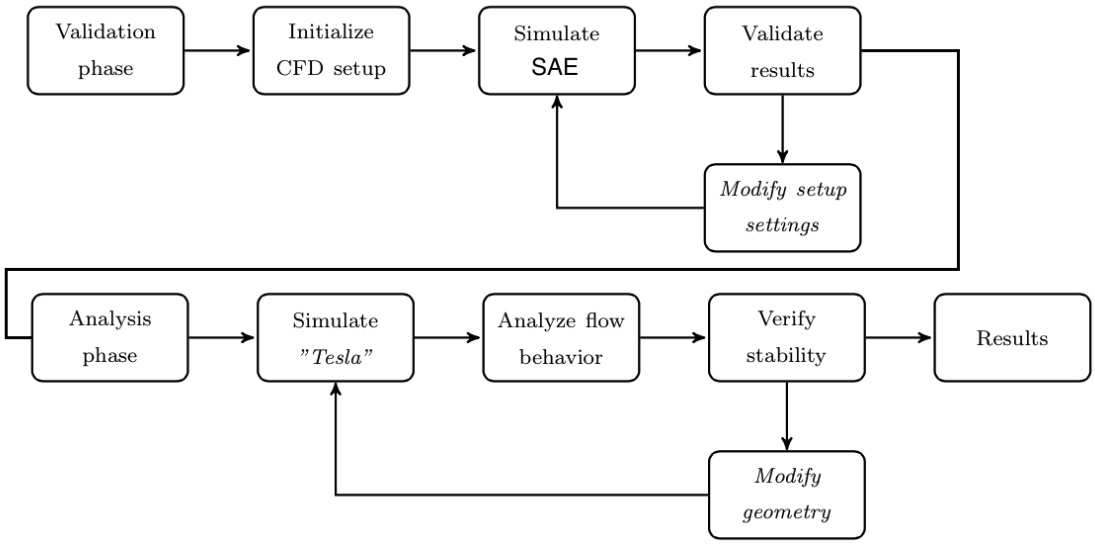

Figure 1: Preliminary workflow indicating the validation and analysis phase.

The **validation phase** consists of the validation of the CFD software by utilizing the SAE reference body and its aerodynamic results which stem from available literature. The **analysis phase** comprises the simulation runs of the simplified *"Tesla"* vehicle shape geometry, followed by a vehicle stability assessment. This analysis is within an iteration loop in order to assess the impact of various shape modifications.

Part I

Bluff body aerodynamics

Chapter 1

Introduction to vehicle (aero)dynamics

Bluff bodies such as modern vehicles typically feature many regions with separated flow due to the steep gradient of the contour in all directions x, y, z. [26] The corresponding adverse pressure gradient is generally such that it is impossible for the flow to remain attached to the surface. One of the most pronounced regions where this occurs is at the vehicle base (near the back of the vehicle), which is generally blunt for practical reasons. In this area large turbulent flow zones are present which have detrimental effects for the vehicle drag.

There are essentially two main flow phenomena of interest for a bluff body such as a vehicle. [46] Close to the vehicle and within the wake the flow is typically viscous, where zones of separated and rotational flow occur. Further away from the vehicle and outside the wake the flow is generally inviscid and irrotational. This distinction between the two flow mechanisms are shown in figure 1.1:

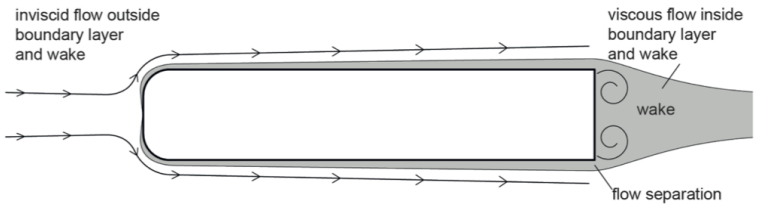

Figure 1.1: Rotational viscous - and inviscid irrotational regions around a bluff body [46]

Within figure 1.1 three important concepts are visualized i.e. the boundary layer, viscous flow and inviscid flow. In order to explain these three concepts in more detail it is necessary to first discuss the physical model of the flow.

Physical model of the flow

There are many different physical models of the flow available for varying purposes. These different models are discussed in-depth in chapter 4. For now it suffices to assume that due to the relatively low speed (typically $< 80m/s$) of the considered vehicles the general flow characteristics can be described by the incompressible Navier-Stokes (NS) equations, which are presented in section 3.5.
Near the end of the 18^{th} century mr. Reynolds related the influence of the flow velocity, a characteristic length of the flow scenario and the molecular viscosity in studying the flow in a channel (Reynolds 1883). This allowed for classification of different existing flow regimes by the so-called Reynolds number, which can be calculated using equation 1.1:

$$Re = \frac{\rho V L_{ref}}{\mu} \tag{1.1}$$

In equation 1.1 ρ represents the density, V indicates the flow velocity, L_{ref} is the characteristic length of the considered geometry (e.g. vehicle length) and μ represents the dynamic viscosity of the considered fluid or medium. The Reynolds number can be interpreted as the ratio between inertial forces and viscous forces, where the flow can be assumed to be inviscid when the Reynolds number exceeds the number 1.0 x 10^7[3].

In order to calculate the Reynolds number, it follows that the value for μ needs to be computed. This can be done using Sutherlands law, which relates μ to the temperature and the density. For sea level conditions, Sutherlands equation can be rewritten as equation 1.2, which is valid for temperatures in the range $100K \leqslant T \leqslant 800K$ [18]:

$$\mu = \frac{T^{1.5} \cdot 1.458 \cdot 10^{-6}}{T + 110.4} Nm^{-2}s \tag{1.2}$$

Within the International Standard Atmosphere (ISA) it is assumed that the mean temperature $T = 288.16K$, which results in a μ of $1.789 \cdot 10^{-5} Nm^{-2}s$.

It follows from equation 1.1 that the Reynolds number is 8.5 x 10^6 for a vehicle which has a length L of around 4 meters cruising at 30 m/s. This has several implications for the boundary layer, as will be discussed in the next subsection.

The boundary layer

Anderson concludes that if the local Reynolds number exceeds $1.0 \cdot 10^7$, the flow can be assumed inviscid, implying that viscous effects can be neglected.[3] This is not the case for the flow adjacent to the body surface, as the flow will decelerate due to friction and viscous effects within a certain domain, known as the boundary layer. Within the boundary layer the velocities are lower and the reference scales are smaller, causing the flow to become viscid.

Analogous to the large-scale flow the boundary layer will generally be laminar at the front of the vehicle, where it will transition towards a turbulent boundary layer at a certain critical distance.[26] This critical distance is subject to different factors such as the distance from the front of the body and the local pressure gradient.

The velocity profile of the boundary layer is different for either a laminar or the turbulent case, as is depicted within figure 1.2. The velocity at the no-slip wall is always equal to zero, and the state is determined by the shape of the velocity profile from zero until the free stream velocity U_∞.

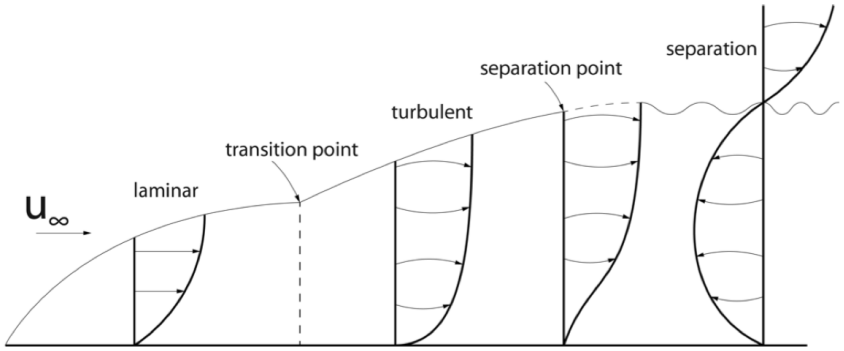

Figure 1.2: Velocity profiles of different boundary layer states [46]

As can be seen in figure 1.2, the velocity profiles are different within each boundary layer state. The flow conditions can be studied using the velocity profiles from a converged CFD solution.

The velocity profiles provide information on the state of the flow inside the boundary layer, which is either laminar, turbulent or separated. The flow within the boundary layer tends to separate when the flow is unable to follow the contour of the body for the given conditions.

Separation of the flow is generally undesirable since it is accompanied with an increase in pressure drag. Because separated flow is important within the analysis of bluff bodies, the next subsection is devoted to additional information regarding separated flow.

Separated flow

Due to the typically steep gradient of vehicle contours the adverse pressure gradients are such that the flow is unable to remain attached. [26] The most pronounced zones where this occurs are just beyond the "leading edge" at the hood of the vehicle, both front corners and in particular the interaction with the wheels and the wheel houses, the junction between the hood and the windshield, the A-pillars and at the rear "trailing edge" of the vehicle where eventually all separated and attached flows combine into the vehicle wake. This regions are visualized in figure 1.3, together with a detailed view on the A-pillar vortex:

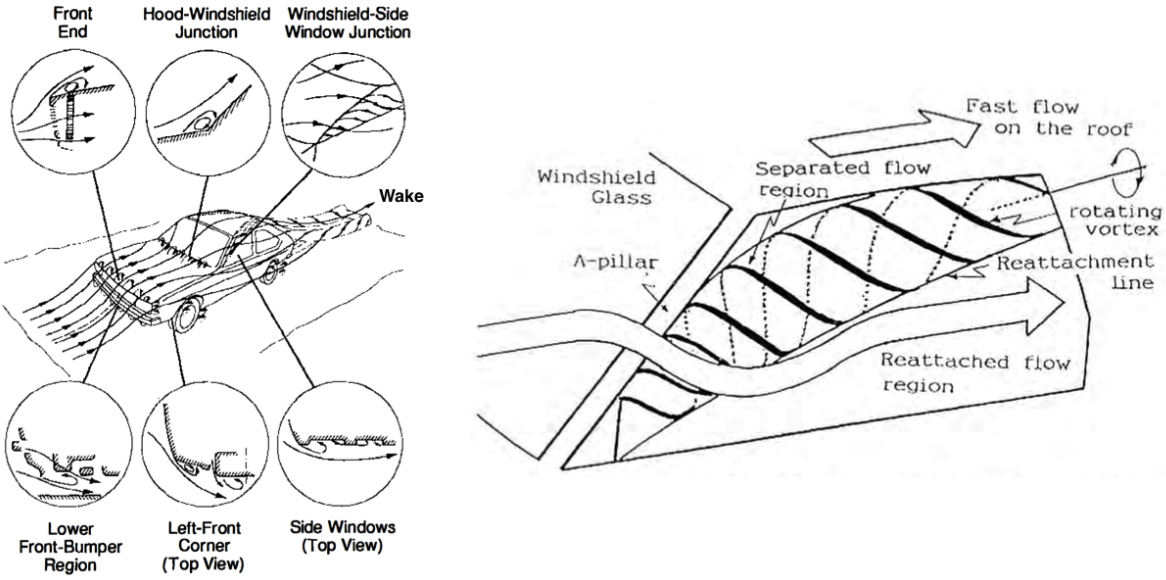

Figure 1.3: Typical regions of separated and reattached flow [23]

Reducing the total amount of separated flow is desired, as separated flow generally results in both pressure drag and noise penalties. [2] [39] This can be done by amongst others minimizing the wake aft of the vehicle, since the wake is the result of all flow phenomena which occur at the entirety of the vehicle. Hucho points out that the C-pillars are most important for the size and impact of the vehicle wake as can be seen in figure 1.3 [26]. This is because the vortex which originates here compresses - and thereby reduces the wake further down. This is one of the main reasons why the aft section of a vehicle should be designed carefully, since this has a positive effect on the pressure drag which is the most important drag contribution for the total aerodynamic drag according to Katz and Tamai. [28] [54]

The flow field around a vehicle is continuously changing due to the dynamical environment around a ground vehicle. The respective implications on the total drag, lift and other flow quantities are discussed within the next sections.

1.1 Forces and moments upon a vehicle

When a vehicle moves through a fluid, both the change of pressure around the vehicle as well as the friction force which the flow exerts on the vehicle contour generate the aerodynamic forces. Since the resultant of the forces in x, y and z direction occur at the continuously changing vehicle center of pressure, three additional moments around the vehicle center of gravity are introduced. These three forces and moments are established within the reference frame in figure 1.4:

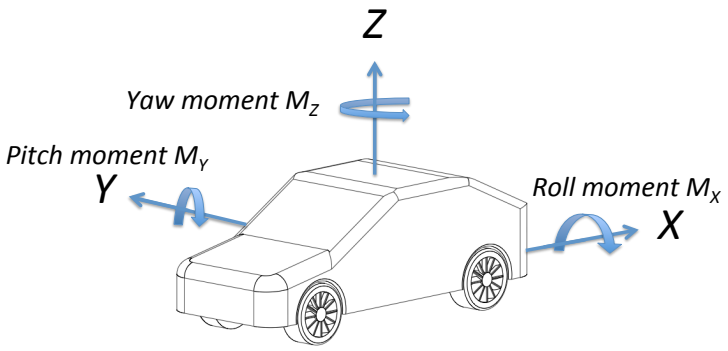

Figure 1.4: Reference frame for vehicles as will be used in this study

The forces and moments in the three directions are frequently used for (aero)dynamic performance analysis, resulting in a distinct name for all three directions:

- The stream wise force in the x-direction is the drag
  The moment around the x-direction is is the rolling moment M_X
- The lateral force in the y-direction is the side force
  The moment around the y-direction is the pitching moment M_Y
- The vertical force in the z direction is to as the lift
  The moment around the z direction is the yawing moment M_Z

The corresponding non-dimensional force and moment coefficients C_F and C_M are calculated using equation 1.5 and 1.6:

$$C_F = \frac{F}{(0.5 \cdot \rho \cdot V_r^2 \cdot A)} \tag{1.3}$$

$$C_M = \frac{M}{(0.5 \cdot \rho \cdot V_r^2 \cdot A \cdot L)} \tag{1.4}$$

In these equations the force F can be either one of the three forces (i.e. lift, drag and side force), and the moment M can also be any of the three moments (i.e. roll, pitch and yaw moment). Next to this ρ represents the density of air whereas A indicates the projected frontal area of the vehicle and V_r is the incident velocity (i.e. $\sqrt{V_X^2 + V_W^2}$ as can be seen in figure 1.6).

The two most important aerodynamic parameters of a vehicle are the vehicle drag and lift, which are discussed in the next subsection.

Drag and Lift

The two prominent aerodynamic vehicle performance metrics are the vehicle drag and lift force. The drag force is defined as the force parallel to the incoming flow in the vehicle x direction, which is in the opposite direction of the vehicle's forward motion causing the vehicle to slow down. The vehicle powertrain ensures that the various drag contributions are overcome, allowing the vehicle to move.

The lift force is the force acting perpendicular to the incoming flow, which as the name suggests is able to either lift the vehicle off the ground, or force the vehicle towards the ground even more. The latter case is called downforce, which allows for extra grip and therefore typically enhanced vehicle handling performance at the expense of additional aerodynamic drag.

The total aerodynamic drag consists of multiple sub drag contributions, which are the pressure, lift-induced, cooling, viscous and internal flow drag. [28]

The first and most important drag contribution is the pressure - or form drag. This drag term originates from separated flows around the vehicle, where the sum of all the associated induced drags defines the total pressure drag.

The pressure drag is caused by the pressure difference due to the high pressure zone in front of the vehicle in combination with the low pressure wake aft of the vehicle. Depending upon the aerodynamic requirements and quality of the design, solely the pressure drag can contribute up to $C_d = 0.45$ for typical passenger vehicles shapes. The flow around the wheels of typical passenger vehicles accounts for up to 50% of the pressure drag for streamlined vehicles. This is because of the typically yawed flow around the wheel due to the vehicle body and interaction effects of the rotating wheels and their wheel wells and suspension components. [26]

The second most important drag contribution is the lift induced drag, which is the result of all the either lift or downforce generating components of the vehicle. Depending upon the segment of the vehicle this drag contribution is typically in the order of $C_d = 0.10$ for passenger vehicles, but can account up to $C_d = 0.60$ for Formula type vehicles.

The cooling drag consists of the drag associated with the cooling of vehicle systems, where radiators and ducts play an important role in reducing the momentum of the incoming flow. Depending upon the cooling requirements this drag contribution typically accounts for up to $C_d = 0.06$.

Viscous drag is defined as the drag which is present as a result of the viscous effects caused by friction of the incoming flow with the body surface. The friction of the flow with the surface is higher when the flow is still attached, which is why this drag contribution can mainly be found in regions where no separation is present. For typical passenger vehicles this drag contribution accounts for up to $C_d = 0.05$.

Next to the reduction in aerodynamic drag the lift force has been an important area of study as well. In recent years more use has been made of the so called ground effect, which can be used to alter the lift or downforce of the vehicle by careful design of the underbody of the vehicle. [60]

Ground effect

Vehicles operate in close proximity to the ground which allows for using the so-called ground effect. In short, this means that the flow around the vehicle is constrained by the ground which can be used to an advantage for creating downforce or reducing drag. This flow is restricted due to the presence of the ground, which makes the flow behave as if the vehicle was "mirrored" around the ground plane. [60] This effect is visualized using an airfoil section in figure 1.5, where it can be seen that the closer a contour gets to the ground, the higher the lift force becomes and the smaller the associated induced drag becomes. [8]

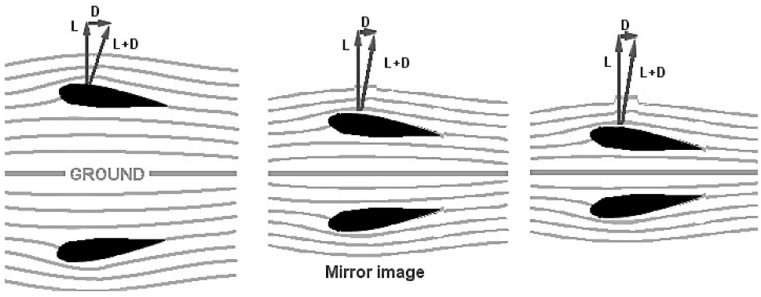

Figure 1.5: Visualization of the ground effect at different distances from the ground

The ground effect can be used in several ways, where wings and curved underbodies called diffusers are the most prominent examples. The extent with which these components are used depends upon the handling requirements for the respective vehicles. Diffusers are more and more being used due to their simplicity, where wings are typically used for Formula type racing vehicles because of practical reasons. Their operating principle is similar, both devices are designed to deliver downforce which is typically used in order to enhance the dynamic performance of the vehicle.

The diffuser is designed in order to induce a low pressure underneath the vehicle, which results in a distributed continuous downforce of the vehicle. Different pressures resulting from different geometries and operating height from the ground result in different drag penalties and downforce values [28].

One important aspect which alters the underbody flow and therefore also diffusers or wings close to the ground is the presence of the four rotating wheels, and the interaction with their wheel wells and the supporting suspension components.

The wheels tend to act as an aerodynamical fence, but also introduce very unsteady flow structures within the underbody flow. The rotating wheels also provide lift, which complicate the interaction effects even further [43]. As was mentioned in the section about pressure drag this results in drag penalties of up to 50% of the pressure drag for a streamlined vehicle [26].

1.2 Crosswind flow phenomena and sensitivity

Natural flows originate from different sources such as the weather, traffic, and the topology of the environment. Depending on the trajectory of the vehicle these natural flows can result into cross-wind flows, where the combination and intensity of these phenomena form the type of cross-wind flow. The (un)steady resultant incoming flow vector V_A depends on the local (within this study orthogonal) cross-wind flow V_W and the velocity of the vehicle V_X. Using these three distinct velocities the cross-wind flow angle β can be deduced as is depicted within figure 1.6:

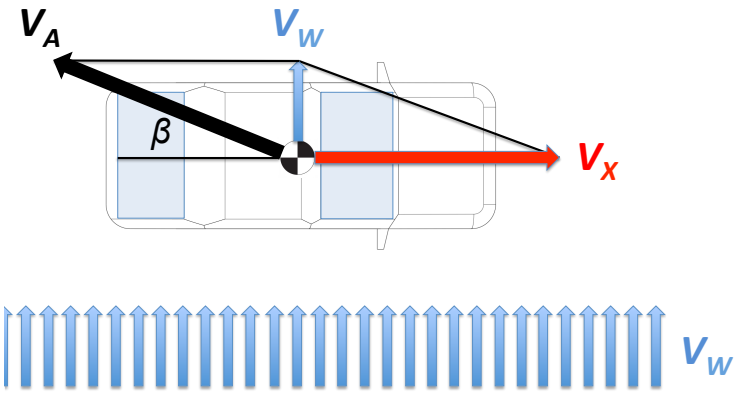

Figure 1.6: Resultant incoming flow vector V_A in a cross-wind environment of angle β

When a vehicle experiences a cross-wind flow environment, the large scale flow phenomena change compared to the symmetric longitudinal flow environment. The cross-wind component of the flow creates a pressure difference between the wind - and the leeward side of the vehicle, where the leeward side typically features large areas of separated flow. This pressure difference results in aerodynamic forces and moments which need to be overcome by means of counter steering the vehicle. The cross-wind flow spectrum and the considered geometry determine the extent of which the motion of the vehicle is affected, which is referred to in literature as the vehicle cross-wind sensitivity.

The cross-wind flow can be mathematical represented as shown in equation 1.5 [18].

$$\frac{D\vec{U}}{Dt} = \frac{\partial\vec{U}}{\partial t} + \frac{\partial\vec{W}}{\partial t} + U\frac{\vec{W}}{\partial x} \tag{1.5}$$

With a constant speed $\frac{\partial\vec{U}}{\partial t} = 0$ the cross-wind can originate from the time varying side wind $\frac{\partial\vec{W}}{\partial t}$ due to the gusts, or from the topology of the environment $\frac{\vec{W}}{\partial x}$.

There are three predominant effects when a cross-wind flow encounters a vehicle. The effects include a rolling motion, side-slipping motion and lastly the rotation of a vehicle due to the difference in center of pressure and center of gravity. These three effects are illustrated in figure 1.7.

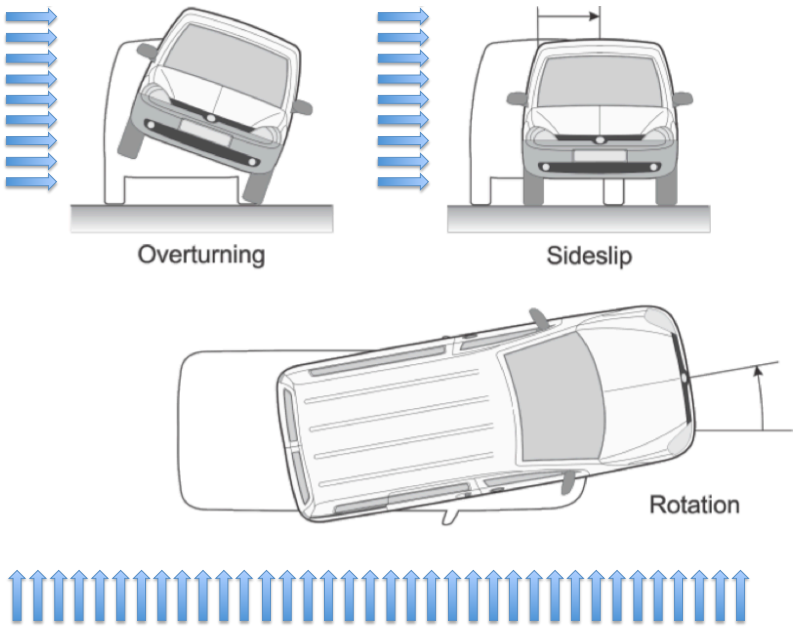

Figure 1.7: Three predominant effects of a crosswind flow upon a vehicle [18]

The magnitude of these three effects depend on the (cross-wind) flow intensity and direction, the vehicle geometry and suspension characteristics. The physics behind these dynamic effects of the vehicle are studied in chapter 4.2, where the governing equations are derived. Using these equations of motion the dynamic effects are presented in chapter 5, where the combination of the three effects is documented.

There have been several efforts to assess the intensity of cross-wind flows, where usually on-road measurements were conducted. [29] [58] In these studies it was found that single peak gusts occur at 63% of the collected data, where trapeze peaks occur 28% of the time. The wind speeds typically carried between 4 and 8 m/s, where the length scale of a cross wind gust is in the order of 20-40m, or to 5 to 10 typical vehicle lengths.

The resultant incident flow angle β varies depending on the speed of the vehicle. Road testing experiments conducted by Tesla Motors showed that the incident cross-wind flow angle β of up to ± 6 degrees is most typical during cruising velocities of $30 m/s$. [43] Therefore within this study a steady cross-wind flow of zero to $+6$ degrees of cross-wind flow is employed upon the vehicle. When a vehicle travels with $30 m/s$ this corresponds to a 90 degree crosswind flow of up to 3.15 m/s during 6 degrees cross-wind flow, and 1.58 m/s during 3 degrees cross-wind flow.

Typical vehicle types in cross-wind flow

Over the years different researchers studied the cross-wind flow phenomena for different basic vehicle shapes in order to draw conclusions with respect to the corresponding yaw moment and yaw rate as a measure of performance. Howell also investigated the change in drag for different geometries under cross-wind flow conditions, and concluded that the outcome for an optimal vehicle handling conflicted with the outcome for a decrease in vehicle aerodynamic drag. [25]

All researchers agree that typically estate back vehicles or square back vehicles have a lower yaw moment compared to either fastback (also called hatchback) or notchback vehicles. This is because the difference in center of pressure (CoP) between these vehicles due to their different geometry. These three types of vehicles are shown in figure 1.8:

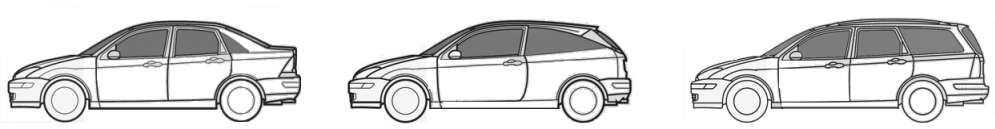

Figure 1.8: Notchback (L), fastback (M) and a estate back vehicle (R). Courtesy of Ford

It has to be noted here that the difference in performance between the fastback and notchback is small. Two independent researchers have contradictory results, as Gilhaus and Renn concluded that the fastback has a lower yaw moment, whereas Howell concludes the opposite. [21] [25] One explanation for this is that within both studies the value for the angle between the roof and the rear window (the so called slant angle), which is an important value for both the yaw angle and the drag coefficient was not specified [18].

Favre reports that any radiusing of the rear C- or D-pillars typically enhance the yaw moment experienced during cross-wind flow conditions. [18] These studies indicate that design parameters such as the radius and angle of the A-pillars have a large influence on both the yaw rate and moment and the drag coefficient as well.

It can be concluded that different typical vehicle types have different yaw rates and moments during cross-wind flow conditions.This is the result of a difference in the CoP locations and vehicle parameters such as the location and magnitude of the center of gravity. Within a single vehicle type there is a dependency with other vehicle parameters as well, which together form the vehicle cross-wind flow sensitivity. The next section discusses this cross-wind sensitivity of vehicles, where the influence of the driver interaction and vehicle dynamic parameters such as suspension settings and center of gravity locations is explored.

1.3 Vehicle dynamics during cross-wind flows

The cross-wind sensitivity of a vehicle is determined by the interaction between vehicle aerodynamics, vehicle dynamics and driver interaction. The outcome of the combination of these three factors is of great importance for the (perceived) stability and therefore safety of the vehicle during cross-wind conditions. Milliken is one out of many researchers to study the vehicle cross-wind sensitivity. [38] In his research Milliken concludes that next to the driver interaction there are four dominating factors for vehicle stability, in particular for cross-wind sensitivity. These four factors form the basis for the directional yaw, pitch and the roll stability, and are listed below:

- The location in x, y and z direction if the center of gravity (CoG)
- The location in x, y and z direction if the center of pressure (CoP)
- The neutral steer point (NSP) or the "center of tire forces"
- Suspension settings, in particular the roll-compliance

The vehicle dynamics definitions and their positions for a typical car are visualised in figure 1.9, where the suspension settings are not shown. These are determined by internal components of the car such as the used springs, dampers and the roll-bar.

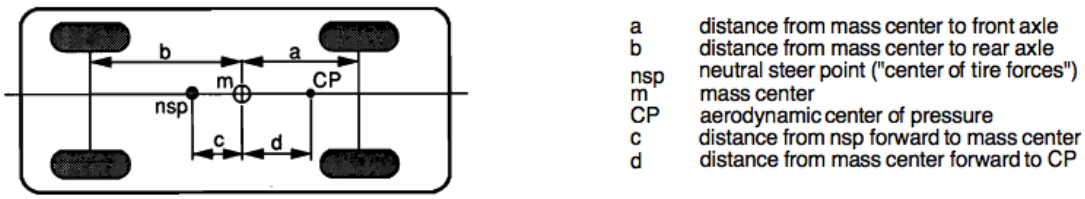

Figure 1.9: Visualization of 7 important vehicle dynamics definitions for a typical car [35]

Road test experiments conducted by mr. Macadam show that the mentioned four factors for vehicle stability are indeed very sensitive to the (perceived) comfort and performance of a vehicle experiencing cross-wind flow. [35] This conclusion was drawn after multiple drivers evaluated a vehicle, which could be changed after a baseline run in terms of CoP, CoG and different roll-bar settings on a "Gauntlet-like" track. At this track a vehicle travels at around 150 km/h, where it encounters cross-wind flow originating from rotating fans, changing from left and right at a $17m$ interval for a total length of $70m$.

It was also found that moving the CoP $0.25m$ forward compared to a baseline vehicle already results in a perceived comfort decrement of around 30%, whereas moving the CoP $0.75m$ backwards increases the comfort with around 20%. Changing the position of the CoG by adding $160kg$ ballast in the trunk decreases the perceived comfort up to 25%.

An other insight from this experiment was that a decrement of 35% in the roll stiffness is also undesired for cross-wind performance, yielding decrements of up to 10% in the perceived comfort.

Macadam reports that in general a forward placed CoP, an aft placed CoG and a reduced roll-stiffness are all undesired in terms of perceived comfort during cross -wind situations. The combination of these three factors result in a vehicle which is perceived as almost uncontrollable, as can be seen in figure 1.10:

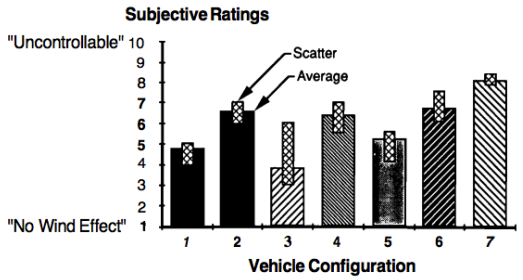

Configuration	Description
1	Baseline Vehicle
2	Aerodynamic CP Moved Forward 10 inches from Baseline
3	Aerodynamic CP Moved Rearward 30 inches from Baseline
4	320 lb Ballast Load Added to Rear Trunk of Baseline Vehicle
5	Baseline Vehicle with Roll Stiffness Reduced 35%
6	Configuration #2 with Roll Stiffness Reduced 35%
7	Configuration #2, with 320 lb Ballast, and Reduced Roll Stiffness

Figure 1.10: Subjective comfort rating for different configurations during cross-winds [35]

Next to the perceived comfort, it can be stated that the most dangerous aspect about cross-wind flow is the resulting yaw-rate, since a change of direction might lead to a traffic collision. In general one can state that overturning and side-slipping for passenger cars are not significant with respect to wind disturbances [18].

Howell investigated the cross-wind flow sensitivity differently, i.e. by characterizing the cross-wind sensitivity by studying the yaw rate response to a given wind input. [25] Howell found that the yaw rate increases inversely with the tyre cornering stiffness, the wheelbase and the vehicle mass. The report concludes that the aerodynamic yawing moment is the most important parameter to be optimized.

It can be concluded that the cross-wind stability might be assessed by an analysis of the vehicle's weight, the position of the CoG, the suspension characteristics and the CoP together with the corresponding forces and moment coefficients. The driver interaction is of importance for the total vehicle cross-wind response, but for the study at hand it is decided to not include this aspect. This is because the additional variable will inherently complicate the design study, without adding much value at this stage of the development process. [9]

Chapter 2

Principles of experimental and numerical methods

The aerodynamic design of the external shape is typically done via a standard three step procedure. [55] Computational Fluid Dynamics (CFD) is first employed in order to simulate the flow in a digital domain. This enables the designer to obtain a first impression of the flow over the vehicle shape.
Once the conceptual design matures, the detailed design begins where usually wind tunnel testing is involved. The obtained data from the wind tunnel runs can be used to validate the CFD results, which results in the first validation stage.
When the design evolves even more the first prototypes are generally thoroughly tested on the road, resulting in even more aerodynamic data.
In this chapter these three aerodynamic measurement techniques will be discussed.

2.1 Computational Fluid Dynamics

Recent trends in the computer industry resulted in lower costs for computationally powerful systems, enabling designers to simulate new designs faster than before.

One of the applications that benefits greatly from this trend is the computationally demanding engineering tool called CFD [3]:

CFD is the art of replacing the integrals or the partial derivatives (as the case may be) in the governing equations of fluid motion with discretized algebraic forms, which in turn are solved to obtain numbers for the flow field values at discrete points in time and/or space.

So essentially what a CFD suite does is convert the analytical equations into values at given discrete points in time or space. The position and layout of these discrete points is dictated by the mesh, which directly defines the quality of the solution.

Constructing the mesh is therefore of high importance and should be performed with corresponding care. For high quality results the distance between the points within the mesh is close to zero and the control volume extends multiple times the

length of the considered geometry upwind, downwind and vertically of the model. The downside of this method is that computational cost constraints generally do not allow these computationally expensive operations. The trick is to find the balance such that depending upon the required accuracy and computational resources the corresponding mesh is created. Here it is essential to bear in mind that not all regions within the control volume require equal accuracy of the flow phenomena. Usually the regions which are adjacent to the considered geometry require the highest accuracy and therefore small distances between the individual points. This is because the flow is most affected in this region due to the pronounced curvature which result in large pressure gradients.

CFD comprises more than the definition stated by Anderson, as there are also more simplified flow-solving methods available such as panel methods which have different principles [3].

CFD has distinct advantages and disadvantages compared to wind tunnels and road testing, which are presented in table 2.1.

Advantages	**Disadvantages**
Study system's performance beyond its practical limits	Since CFD is an approximation there will always be discretization and modelling errors
Analyze problems whose experiments are difficult or dangerous	Danger of straightforward believing the CFD results
Reduces cost and time for new designs	It is easy to overlook real world effects such as turbulence and disturbances
Unlimited level of detail	
Easily updates in geometry	
Easy variations on the flow parameters	
Individual flow components and effects can be identified	

Table 2.1: Advantages and disadvantages for using CFD software

Many of the mentioned disadvantages can be overcome by increasing the computational power, by enhancing the mesh or using a CFD method with a lower modelling error. This approach will usually decrease the discretization error, but comes at a price in the form of either longer processing times or increased hardware requirements.

The ideal situation in CFD for a typical vehicle being simulated within a steady flow would require over 10^{13} discrete points. This idealized performance of CFD is called Direct Numerical Simulation (DNS). The hardware requirements for a DNS are so extensive that simulating a full 3-D vehicle these are probably not met for several decades.

It is concluded that CFD is a very powerful and effective engineering tool throughout the entire design process for aerodynamic analysis.

2.2 Windtunnel experiments

The outcome of the CFD simulations can be validated using a wind tunnel. A (full) scale model of the geometry can be placed within this engineering tool's test section, where the model is subject to an incoming flow. Depending upon the desired simulation, the flow parameters within the wind tunnel can be set accordingly. The model can be inclined under various (transient) attitudes in order to model either cross-wind flow or aerodynamic effects due to the vehicle motion. Usually a force-balance system is used in order to assess for the resultant forces and moments around all body axes. A typical closed loop (Göttingen) advanced wind tunnel is shown in figure 2.1:

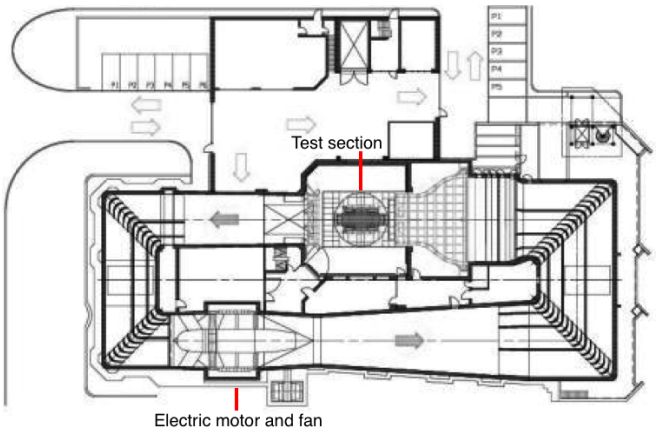

Figure 2.1: FKFS Aero-acoustic wind tunnel of University of Stuttgart. P = 3200 kW [53]

Within figure 2.1 one can see the counter-clockwise rotating flow architecture. In the top right corner one can see that a throat is installed just before the test section, which is used to accelerate the flow. Within each corner metal vanes are applied for guiding the flow and to remove turbulence.

The main advantages and disadvantages of wind tunnels are listed in table 2.2 [49]:

Advantages	Disadvantages
Wind tunnels deal with real flow	Experimental errors are still present
Virtually any flow can be produced	Setup time and operating cost are high
Easy to incline the model under different (transient) attitudes	Post processing and analysis time are required
Possible to interchange components with different geometries	Difficult to measure the complete flow field
	Moving ground complex and expensive
	Scaling issues when scale models are used

Table 2.2: Advantages and disadvantages for wind tunnel systems

One can conclude that a wind tunnel is a very useful engineering tool, where its inherent advantages and disadvantages need to be taken into account.

2.3 Road testing

The third and last discussed aerodynamic measurement method involves actual test drives on the road. This method can only be done when the design of the vehicle is advanced up to a level that the first prototypes are constructed. During these tests the in-service environments can be experienced, making this the most accurate method in terms of environment of all available methods. There are however several shortcomings to this method, among others the acquiring data points from the measurements. A popular technique is called the coast down method [7], where the vehicle travels at a certain velocity after which powertrain is disconnected. During the coasting of the vehicle, the only two forces acting upon the vehicle are the aerodynamic drag and the rolling resistance.

In the past efforts have been done [44] where the vehicle was surrounded by a protective casing, such that the rolling resistance could be determined. After subtraction the rolling resistance from the scenario without the protective casing, one can obtain the aerodynamic drag.

The main advantages and disadvantages are concluded by amongst others Scarano [49] and Hucho [26] and are listed in table 2.3:

Advantages	**Disadvantages**
Close resemblance with in-service flow conditions	Difficult to measure (individual) flow-field properties
Unpredicted side-effects become apparent	Time consuming
No computational or wind tunnel induced errors	Subject to local environmental boundary conditions such as ambient winds

Table 2.3: Advantages and disadvantages for road testing

Using road testing as a measuring method obviously requires a working prototype vehicle, which is not available at this stage for this thesis work.

Conclusions on analysis and measurement techniques

Given the research objective and the available resources it is concluded that CFD is the most suitable aerodynamic analysis method within this research scope. Where the other techniques are more suitable for detailed design, CFD allows for relatively easy simulations of vehicle designs which are subject to change all within an easy to transfer digital domain. This is especially useful for continuation of this work after the research performed within this thesis.

Chapter 3

CFD software

It was concluded in chapter 4 that CFD was selected to be the most feasible method within the research scope. In order to use CFD, it is of great importance that the fundamental principles of the flow solving principles are well understood.

This chapter includes a brief overview of the available fundamental principles for computational models of a physical process. Together with these basics a typical layout of a CFD software suite is presented. This chapter also includes theory behind the validation and verification process of the available CFD computational models. At the end of this chapter a selection is made for both the pre-processing software which will deliver the mesh and the actual flow solver software suite.

3.1 CFD Software suites

There are three important steps which need to be taken in effort of computational modelling of physical processes, which are the problem definition, the mathematical model and the computer simulation. [45] The first step is to define a representation of the problem of interest, where a set of desired relevant parameters are identified. Here it should be accepted that it is not always possible to guarantee the fidelity of the simulations because of an incomplete understanding of the physical process. The second step in computational modelling is to find a mathematical model which is able to capture the real world physics. These mathematical models should reflect the governing equations of the problem. There are different governing equations of physical processes available, such as the Navier-Stokes equations for fluid dynamics. Most governing equations are complex and therefore typically difficult to solve both analytically and computationally. For this reason well defined and correctly argued simplifications of the problem at hand are implemented if possible.

A CFD software suite is a design tool which allows the user to model physical processes in the computational fluid dynamics realm. Since there are different software suites available, the general structure on how these suites allow the user to complete the three steps are discussed in the next subsection.

The typical procedure for performing CFD simulations consist out of three distinct parts. In short, first the simulation is pre-processed by constructing the mesh. The mesh presented to a CFD solver which solves the simulation according to a pre-defined mathematical model. Using the data from this simulations different post processing tools are available for interpreting the results. These three main aspects of a CFD are elaborated within the next subsections.

3.2 Pre-processing the simulation

The pre-processing stage includes data processing of the systems flow input environment. Here the user can define the computational domain, as well as establishing the mesh around the considered geometry. As was mentioned before in chapter 4, in general it holds that the better the cells are distributed, in combination with the total amount of cells, the higher the accuracy will be of the solution. In general one can state that optimal meshes are non-uniform, where finer areas are present at locations where large variations of the geometry occur. Another aspect which the user should do is select the physical and chemical phenomena that needs to be modelled. In addition to this the boundary conditions need to be defined as well. The construction of the domain geometry as well as the grid typically require up to 50% of the time spent on a typical CFD project.

After the initialisation has been completed within the pre-processing stage, the domain needs to be discretized such that a solver is able to compute the individual calculations.

There are four distinct discretization methods which are typically used to discretize the system, i.e.

1. The Finite Difference Method (FDM)
2. The Finite Volume Method (FVM)
3. The Finite Element Method (FEM)
4. Spectral Methods

These four discretisation schemes show some resemblance with one another, each having its own advantages and disadvantages. Therefore it will depend upon the application which of these is most suitable. The main characteristics will be discussed in more detail.

FDM
With the FDM discretization one can describe the unknown flow parameters of the flow problem by means of point samples at the node points of a grid of coordinate lines based upon the *differential* formulation of the governing equations. Here the truncated Taylor series expansions are often used to generate finite difference approximations of derivatives of the flow parameters in terms of point samples at each grid point and its neighbours. The next step in FDM is to replace the appearing derivatives in the governing equations by finite differences, which result in an algebraic equation for the values of the flow parameters at each cell location.

FVM
The FVM discretisation can be regarded as a special formulation of the FDM, which is typically used in modern CFD codes. In short, the FVM converts the governing equations based upon an *integral* formulation of the governing equations into a system of algebraic equations, which is solved using an iterative method. Similar to the FDM, the values are calculated at discrete points in space. The main difference however is that for FVM the values are computed for a small volume surrounding each node point on a mesh, rather than evaluating the value based upon the adjacent point.

FEM
The FEM scheme discretizes the domain of the system within elements with a finite area or volume, in terms of specified basis functions. The computational domain is divided up into finite elements, where the solution at each location is constructed using the basis functions. After this division the values of the unknown functions can be approximated inside each elements with either a linear or quadratic polynomial.

Spectral methods
Spectral discretisation methods approximate the unknown values of the flow field by means of either truncated Fourier series, or series of Chebyshev polynomials. These approximations are not local, instead they are valid throughout the entire computational domain. These truncated series replace the unknowns in the governing equations, after which the constraints complete the system. The spectral solvers is closely related to the FEM discretisation scheme. The main difference lies within the basis functions that are nonzero for spectral solvers over the entire domain, whereas the basis functions for FEM are nonzero in small subdomains.

In general it can be stated that a comparison of these four methods is difficult, due to amonst others the many variations of each method. Typically it can be stated that FVM and FDM provide discrete solutions, whereas FEM and Spectral solvers provide - up to a certain extent - continuous solutions.

Now that all typical discretization methods have been addressed the solving phase can commence. The different equation solving methods that are available will be discussed in the next subsection.

3.3 Solving the system

Assuming that the system has been discretized correctly for the right purpose the solver can start computing the simulation. There are different mathematical models which can be utilized, which will be discussed within this subsection. The main different variations are shown in figure 3.1, where the methods which are most accurate are listed on the top - and the most simplified methods are listed on the bottom.

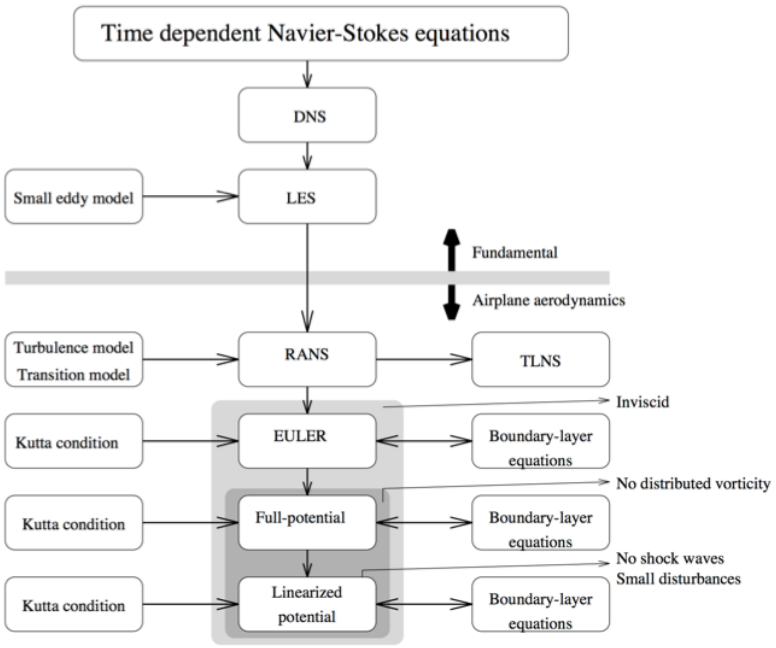

Figure 3.1: Overview of available mathematical flow models [20]

From figure 3.1 it follows that the time-dependent Navier Stokes equations are most accurate when a Direct Numerical Simulation (DNS) is employed. As was explained in chapter 4, this solver is computationally demanding up to an extent that with modern hardware resources only very simple geometries can be analyzed.

Smagorinsky [51] simplified the full Navier-Stokes equations using a low-pass filter which eliminates the small scale flow phenomena, which resulted in the Large Eddy Simulation (LES) scheme. The amount and scale of turbulence which is filtered can be selected by the user and typically depends upon the corresponding turbulence theory and computational resources. The turbulence consists out of different sizes of eddies, where fundamental principle is that the several orders of magnitude bigger eddies are more important to capture since these contain most of the turbulent kinetic energy.

This simplification results in a decrease of computational resources compared to DNS, although LES is typically still too computationally demanding for modern systems [37].

Todays most popular method for CFD software suites remains the Reynolds Averaged Navier Stokes (RANS) method, which uses a different mathematical schemes to model
turbulence compared to LES. More information about RANS can be found in section 3.5. The Euler method arises when the viscous action terms are neglected. When the equations are simplified even further by removing the vorticity equations the full potential equations can be used. After linearization of the full potential equations, one arrives at the linearized potential equations.

There are other methods available than the (derivatives of) traditional Navier-Stokes equations, such as the Lattice Boltzmann methods. This method uses the discrete Boltzmann equation in order to simulate a Newtonian fluid using collision models rather than solving the Navier-Stokes equations. [31] This promising solving method is left out of the consideration as there are very few CFD software suites who uses this novel technique.

Post processing the results

Once the solver has performed the analysis, the post processing phase can begin. Depending upon the user requirements, this phase consists of data interpretation and visualisation tools. This allows the user to draw conclusions on data (trends), and visualize results such as the pressure and skin friction, vector plots, particle tracking and dynamic animations.

3.4 Selecting CFD software

In order to select the appropriate CFD software suite, it is useful to state the requirements to obtain answers for the research objectives. These requirements can be found in the (sub-) research questions:

- Obtain a deeper understanding on how to reduce the drag of a simplified vehicle model which experiences a realistic cross-wind flow, and investigate its dynamic performance.
- Identify which design variables are (more) sensitive to drag increments in steady-state crosswind flows
- Ideally use RANS equations
- Ideally the CFD software would be open-source

Based upon a literature research and thorough discussions with experts in the CFD field, several potential CFD software suites were distilled and presented in table 3.1. In this table the most important characteristics are listed which will form the basis for a trade-off for the final selection of a CFD software suite.

CFD Package	CFD Method	Open Source
OpenFOAM	RANS / LES	✓
OpenFOAM Helyx	RANS / LES	✗
SU^2	RANS	✓
EXA PowerFLOW	Lattice Boltzmann	✗
Fluent	(U)RANS LES	✗
Numeca	RANS	✗

Table 3.1: Considered options for CFD software

Since an open-source software suite is preferred, both OpenFOAM and SU^2 are good options. Out of these two options the relatively new software suite SU^2 was chosen for its relative simplicity and robustness. SU^2 is easy to set up on a cluster environment within the TU Delft facilities, which is ideal for the large number of simulations which are to be performed. The Aerospace department within Delft University of Technology has a growing interest into utilizing SU^2 software as an important CFD tool within the curriculum, where it still needs to be explored how suitable the software is for this application. This is an additional motivation to test how capable this software suite really is.

3.5 Stanford University Unstructured

The Stanford University Unstructured suite is an open-source unstructured grid, finite element or finite volume CFD solver written in C++. *SU*^{2} is capable of producing numerical solutions of partial differential equations (PDE), together with performing PDE constrained shape optimisation. The software was first released in early 2012, after which an enthusiastic community has contributed to where it is today. *SU*^{2} can be set to run on a single processor for desktop use, or parallel where multiple cores in order to reduce the computation time. For now *SU*^{2} does not feature a Graphical User Interface (GUI) yet, instead it is initialised using a text configuration file together with a separate mesh file. This mesh file can be in either the SU2 format or within the standardised CFD General Notation System (CGNS).

SU^2 features 3 predominant CFD solvers, which are the Reynolds-Averaged Navier-Stokes equations (RANS), the Navier-Stokes equations for laminar flows and Euler equations. Here RANS are considered the best optimum between computational resources and accuracy of the results. The RANS equations consist of the complete Navier-Stokes equations, where certain contributions are neglected. The complete Navier-Stokes equations are presented in equations 3.1 - 3.4, where the individual contributions are indicated using the definition presented by Anderson [3]. The original Navier-Stokes equations consist of the momentum equations, whereas the mass, momentum and energy conservation laws nowadays together form the complete Navier-Stokes equations.

$$\underbrace{\frac{\partial \rho}{\partial t}}_{\substack{\text{time rate of change} \\ \text{of mass}}} + \underbrace{\nabla \cdot (\rho \mathbf{V})}_{\substack{\text{mass flow leaving} \\ \text{volume } \mathcal{V}}} = 0 \tag{3.1}$$

$$\underbrace{\frac{\partial \rho_i}{\partial t}}_{\substack{\text{time rate of change} \\ \text{of species mass}}} + \underbrace{\nabla \cdot (\rho_i \mathbf{V}_i)}_{\substack{\text{mass flow leaving} \\ \text{volume } \mathcal{V}}} = \underbrace{\dot{w}_i}_{\substack{\text{species mass rate of change} \\ \text{due to chemical reactions}}} \tag{3.2}$$

$$\underbrace{\frac{\partial (\rho \mathbf{V})}{\partial t}}_{\substack{\text{change of momentum} \\ \text{due to unsteady} \\ \text{fluctuations}}} + \underbrace{\rho \, (\mathbf{V} \cdot \nabla \mathbf{V})}_{\substack{\text{momentum flow out} \\ \text{of volume } \mathcal{V}}} + \underbrace{\nabla p}_{\substack{\text{pressure force} \\ \text{on S}}} \tag{3.3}$$

$$+ \underbrace{\rho \, \mathbf{f}}_{\substack{\text{body force}}} + \underbrace{\nabla \cdot \left[\mu \Big(\frac{\partial u_i}{\partial x_j} + \frac{\partial u_j}{\partial x_i} \Big) + \lambda \nabla \cdot \mathbf{V} \right]}_{\substack{\tau_{ij} \text{ surface force} \\ \text{due to viscosity}}} = 0$$

$$\underbrace{\frac{\partial (\rho E)}{\partial t}}_{\substack{\text{time rate of change} \\ \text{of energy}}} + \underbrace{\nabla \, (\rho \mathbf{V}) E}_{\substack{\text{energy flow out} \\ \text{of volume } \mathcal{V}}} = \tag{3.4}$$

$$\underbrace{\nabla \, (k \cdot \nabla T)}_{\substack{\text{transport of energy} \\ \text{due to thermal} \\ \text{conductivity}}} - \underbrace{\nabla \Big(\sum_i \rho_i \mathbf{V}_i h_i \Big)}_{\substack{\text{transport of energy} \\ \text{due to chemical} \\ \text{diffusion}}}$$

$$- \underbrace{\nabla \mathbf{q_R}}_{\substack{\text{transport of energy} \\ \text{due to radiation}}} - \underbrace{\nabla \cdot (p \mathbf{V})}_{\substack{\text{work done} \\ \text{due to pressure}}} + \underbrace{\nabla \cdot (\mathbf{V} \tau_{ij})}_{\substack{\text{work done} \\ \text{due to viscous stresses}}}$$

As can be seen from equations 3.1 - 3.4, the Navier-Stokes equations include viscous, radiative, chemical, species continuity, diffusion and conduction effects. Because not all these effects are necessary within this study it is possible to exclude certain effects in order to reduce the simulation complexity and thereby the computational resources. The following quantities are excluded within this study:

1. Species continuity as presented in equation 3.2
2. The body forces
3. Transport of energy due to chemical diffusion
4. Transport of energy due to radiation
5. Transport of energy due to thermal conductivity

The flow is also considered to behave as a perfect gas, which allows for rewriting the internal energy contribution in equation 3.4 using the temperature T. In addition the density and the viscosity now become a function of the temperature T. Furthermore the flow is considered to be isothermal and incompressible, which results in the energy equation presented in equation 3.5 to become unused. One can obtain the Reynolds Averaged Navier-Stokes equations from the remaining contributions using Reynolds decomposition, where the flow quantities are separated using a mean component and a fluctuating component. For the velocity u in i direction this results in equation 3.5:

$$u_i(x_i, t) = \bar{u}_i(x_i) + u'_i(x_i, t) \tag{3.5}$$

Here the mean of the latter fluctuating component is equal to zero:

$$\bar{u}'_i(x_i, t) = 0 \tag{3.6}$$

When all time dependent quantities in the Navier-Stokes equations 3.1 - 3.4 are Reynolds averaged, the remaining continuity equation 3.1 and the moment equation 3.3 can be rewritten as presented in equation 3.7 and 3.8 respectively using a tensor notation:

$$\frac{\delta \bar{u}_j}{\delta x_j} = 0 \tag{3.7}$$

$$\frac{\delta \bar{u}_i}{\delta t} + \bar{u}_j \frac{\delta \bar{p}}{\delta x_j} = -\frac{1}{\rho}\frac{\delta \bar{p}}{\delta x_i} + \frac{1}{\rho}\frac{\delta}{\delta x_j}\left(2\mu S_{ij} - \frac{2}{3}\mu \frac{\delta u_l}{\delta x_l}\delta_{ij}\right) + \frac{\delta}{\delta x_j}(-\rho \bar{u'_i u'_j}) + S_i \tag{3.8}$$

Within equation 3.5 - 3.8 it can be sen that for a three-dimensional flow with the aforementioned simplifications four equations with 10 corresponding unknowns are required. These 10 unknowns are the 3 velocity components, the pressure, and 6 unknowns within $\bar{u'_i u'_j}$. Within RANS equations the latter 6 unknowns are known as the Reynolds stress tensor, which are handled using turbulence modelling for closure of equations 3.5 - 3.8. The turbulence modelling can be performed within SU^2 using the Spalart Allmaras or the SST turbulence scheme. For more information on these turbulence models the reader is referred to Anderson [3].

In order to simulate numerous simulations using RANS equations it is essential to utilize the parallel functionality within SU^2. This can be done by compiling the code from source, where it is essential to install the open-source Message Passing Interface (MPI) first. Once this is done the mesh domain can be divided over separate segments which can be simulated by separate processors using METIS. This segmentation is done automatically within Python scripts which are included in the installation. This makes it possible to simulate simple geometries even on modern personal computers.

SU^2 is able to perform both direct and adjoint simulations. Direct simulations returns the flow field and delivers resulting aerodynamic force and moment coefficients, whereas the adjoint solver calculates gradients and sensitivities of the flow field towards a pre-defined objective such as lift, drag or any other moment or force coefficient. This information is particularly useful for optimization purposes.

Once the simulation settings are configured the simulation can commence. A typical testcase run is shown for reference in figure 3.2:

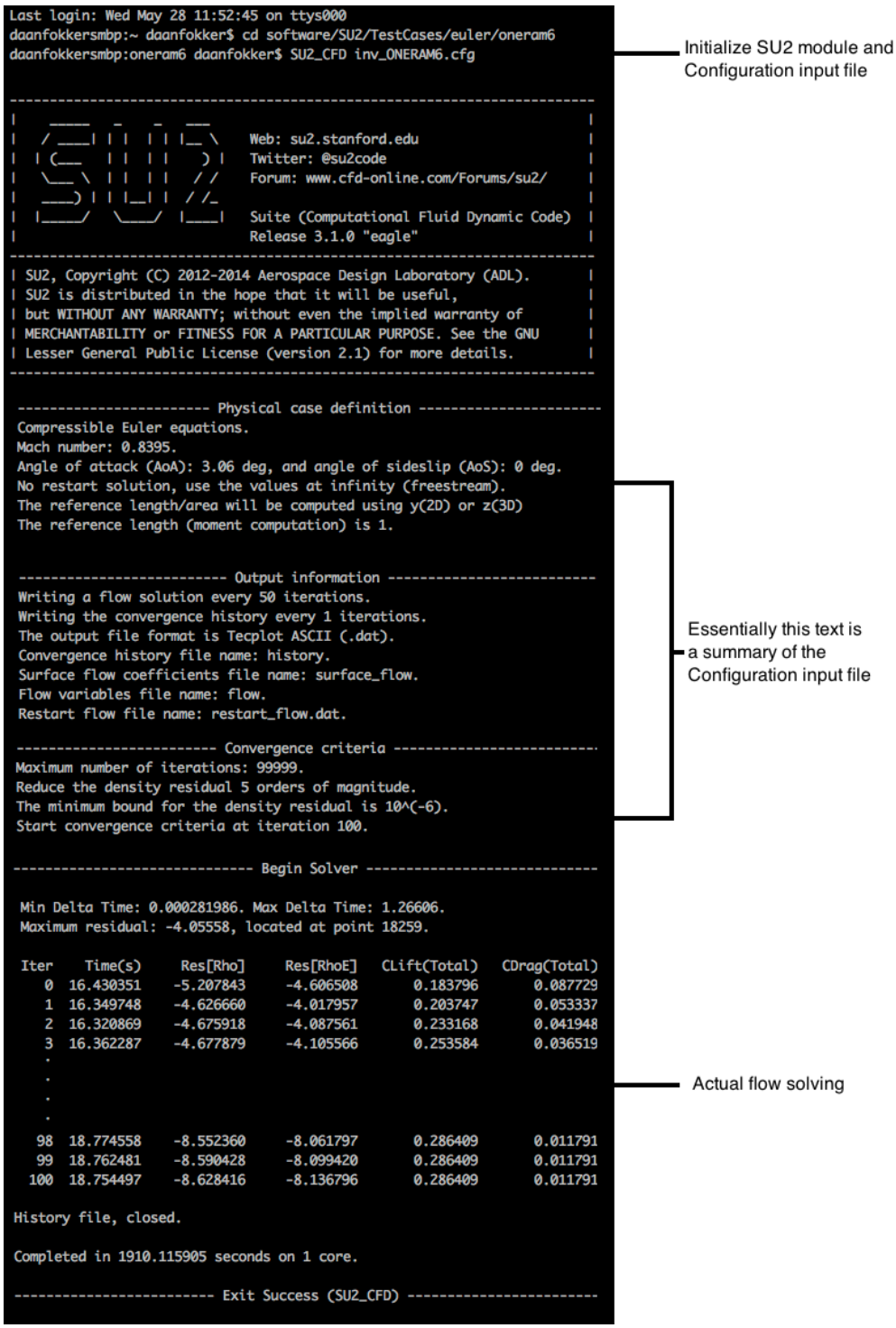

Figure 3.2: Onera M6 testcase within the SU^2 environment

3.6 Validating the CFD software

The SU^2 CFD software can be validated for use with bluff bodies using a reference vehicle geometry. From the different reference vehicles studied in literature, the SAE reference vehicle was chosen due to the close resemblance of the vehicle geometry within this study. The SAE reference vehicle geometry is shown in figure 3.5:

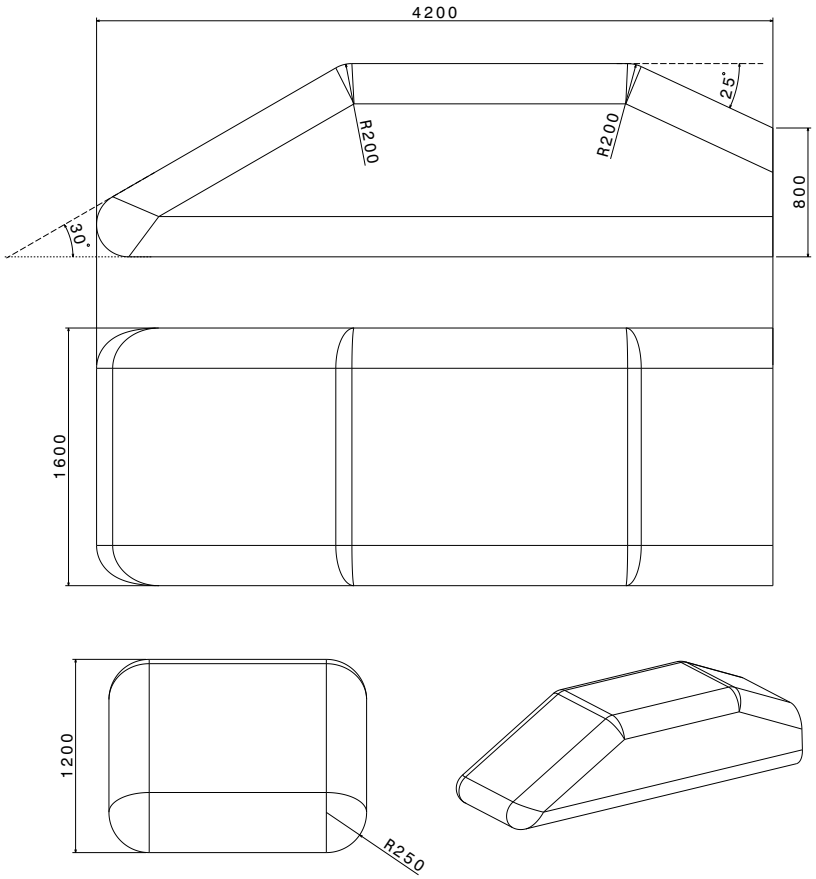

Figure 3.3: The SAE Reference vehicle is used for validation of the CFD software

As can be seen from figure 3.5, this vehicle is simplified to a great extent. There are no wheels present and also no realistic add-ons such as mirrors, cooling intake, and numerous other production vehicle details. Despite these simplifications it was shown that this vehicle is useful for validation purposes and even design studies on systematic design modifications [55]. This geometry is imported within ANSYS meshing software, after which a control volume is defined around the vehicle. The procedure for constructing this mesh is extensive, for this reason the details on the mesh construction are documented within Appendix V: Ansys Meshing. The result from this operation is shown within figure 3.5, which shows the control volume, the vehicle geometry and the markers are visible which are used to assign appropriate boundary conditions.

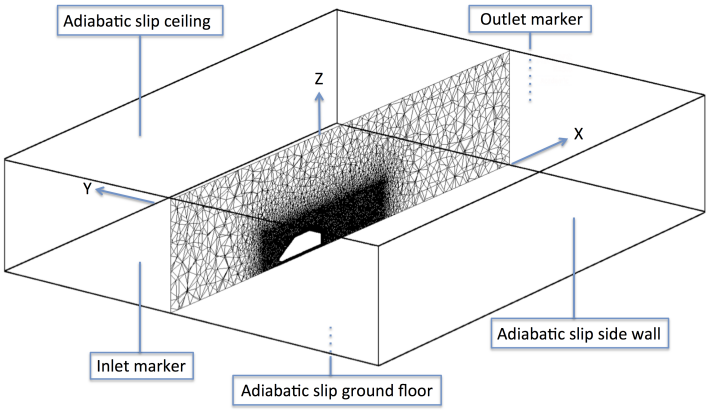

Figure 3.4: The SAE Reference vehicle within the digital domain

A detailed view of the reference vehicle mesh is shown in figure 3.5m which also indicates the no-slip adiabatic wall markers. In addition the 20 inflation layers which cover the vehicle surface are indicated which ensure additional accuracy in the viscous region close to the vehicle surface.

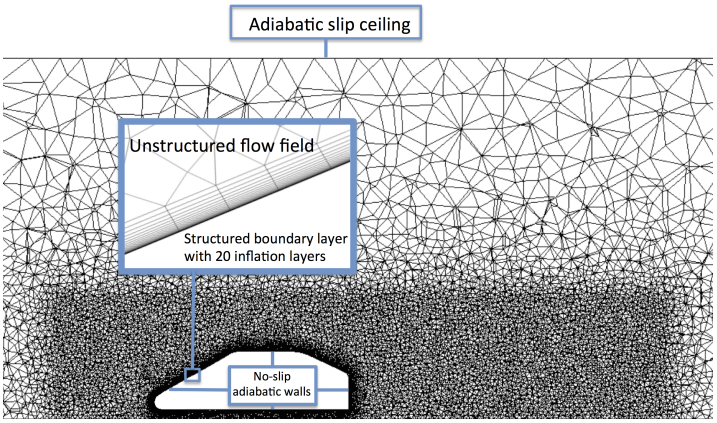

Figure 3.5: Close-up of the SAE Reference vehicle in the digital domain

The results in terms of the pressure field and the resultant force coefficients can be compared by the study conducted by Toppinga [55]. Here Toppinga used Daimler's Pro-STAR for his volume meshing, and STAR-CD for the actual CFD solving. Within STAR-CD the RANS equations are used in combination with a $k-\epsilon$ turbulence scheme [55]. The results from these simulations are compared by the results obtained from SU^2 within table 3.2:

Aerodynamic metric	SAE reference model *Toppinga*	SAE reference model SU^2 *Spalart - Allmaras*	SAE reference model SU^2 *SST*
C_D	0.210	0.200	0.200
C_L	0.200	0.210	0.210

Table 3.2: Validating SU^2 by comparing results with Toppinga's study

It can be seen in table 3.2 that the forces coefficients differ 5% between Toppinga's results and both simulations performed by SU^2, where two different turbulence modelling schemes have been tested. Unfortunately SU^2 does not include a k - ϵ turbulence modelling scheme to compare with. The corresponding pressure distribution of the SAE reference vehicle simulation using SU^2 is visualized within figure 3.6:

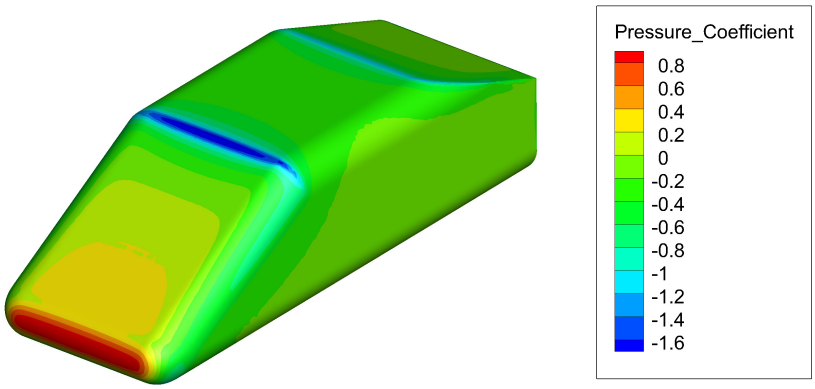

Figure 3.6: SAE Reference vehicle surface pressure distribution

The surface pressure distribution from figure 3.5 shows good resemblance with the surface pressure distribution found in Toppinga's study. Since both the surface pressure field and the force coefficients are similar, it can be concluded that SU^2 can produce reliable results which can be used for identifying trends.

Mesh dependance study

When performing CFD calculations there is typically a trade-off to be made between the fidelity of the aerodynamic results and the computational resources that are required. For this reason it is essential to perform a mesh dependance study in order to assess the stability of the results among different meshes, where an enhanced mesh typically results in increased computational resources. In order to assess the sensitivity of the forces coefficients towards the fidelity of the mesh two simulations are compared, where one simulation is conducted using an enhanced mesh. The results are presented within table 3.3:

Metric	Baseline mesh	Enhanced mesh
Number of cells	3 million volume cells	5 million volume cells
Inflation layers	20	20
Total inflation height	13 mm	13 mm
C_D	0.21	0.21
C_L	0.20	0.20

Table 3.3: Mesh dependance study results

Since the force coefficients do not change when the enhanced mesh is used, it can be concluded that the baseline mesh is sufficient for obtaining reliable force and moment coefficients.

Part II

Vehicle Dynamics

Chapter 4

Vehicle dynamics model

The second part of the thesis documents the performed Vehicle Dynamics study. Within this part there are four main sections, starting with an introduction to Vehicle Dynamics. This section is succeeded by the associated governing equations of motion for ground vehicles. Afterwards the mass distribution and associated mass moments of inertia are examined. These three sections are then combined within MATLAB within section 4.4.

4.1 Introduction to vehicle dynamics

Vehicle dynamics is an engineering discipline which studies the dynamical motion of ground vehicles. The dynamics of a vehicle are amongst others dependent on the vehicle's (suspension) geometry, its mass distribution, tire specifications, aerodynamic loading, road surface and specific modes of motion. The relations between these properties is dictated by classic mechanics theory. The vehicle handling is defined as the combination of the vehicle's lateral response (i.e. cornering, turning, directional response) and the vehicle's feedback towards the driver. It is generally difficult to obtain a satisfactory vehicle handling and driver comfort, given their different - usually contradictory - requirements.

Analogous to the aerodynamics part it is good practice to first define two important reference systems, which are shown in figure 4.1 and fig 4.2. Figure 4.1 shows the SAE Vehicle axis system, and fig 4.2 shows a typical vehicle within an Earth fixed coordinate system.

Vehicle fixed coordinate system

The right-hand orthogonal vehicle fixed coordinate system is typically used for describing vehicle motion using velocities and shown in figure 4.1. The origin of this reference frame is located at the vehicle center of gravity, and travels along with the vehicle.

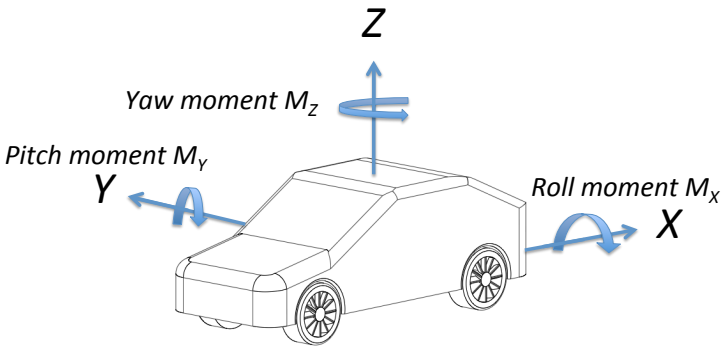

Figure 4.1: SAE Vehicle fixed reference frame

Earth fixed coordinate system

The Earth fixed coordinate system on the other hand is mostly used for vehicle maneuvers. The origin of this reference frame is typically located at the vehicle fixed coordinate system at the beginning of the respective maneuver.

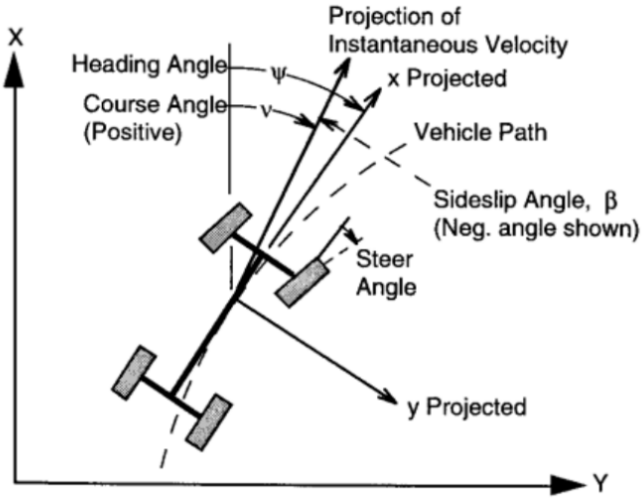

Figure 4.2: Trajectory of a vehicle within the Earth fixed reference frame

The coordinates of the vehicle during the maneuver within the $X-Y$ plane is governed by the quantities indicated within figure 4.2. The meaning of these quantities is listed on the next page.

- X - Forward travel
- Y - Lateral travel
- Z - Vertical travel
- Ψ - Heading angle, the angle between x and X
- ν - Course angle, the angle between the velocity vector and the X-axis
- β - Sideslip angle, the angle between the vehicle longitudinal x axis and the vehicle velocity vector
- Steer angle is defined as the angle between the vehicle longitudinal x axis and the center line of the front wheels

Typically the vehicle motion is described using the respective velocities (forward, lateral, vertical, roll, pitch and yaw) using the vehicle fixed coordinate system, whereas the velocities are referenced towards the earth fixed coordinate system.

Euler angles

The vehicle and earth fixed reference frame can be related to one another by making use of so called Euler angles. These Euler angles consist of a sequence of three angular rotations around the three principle axis of the earth fixed system. The vehicle yaw angle is measured by rotating the vehicle around the Z-axis, the vehicle pitch angle around the Y-axis, and the vehicle's roll angle follows from the rotation around the X-axis.

Newton's second law applied on vehicles

All forces and moments that apply to the vehicle are defined as if they act upon the vehicle. This implies that e.g. a resultant positive force in the x axis causes the vehicle to move forward. Typically the moments are calculated around the vehicle center of gravity.

The fundamental laws which form the foundation of most vehicle dynamics analysis is Newton's second law, which applies to both translational and rotational systems. For translational systems it holds that the sum of forces acting on a body in a given direction is equal to the product of its total mass and the acceleration:

$$\Sigma F_i = M \cdot a_i \tag{4.1}$$

Within equation 4.1 F_x represents the resultant force in the i-direction, M is the total mass of the considered body and a_i is the acceleration in the i-direction.

Newton's second law can also be applied on rotational systems, where it holds that in this case the sum of applied torques which act upon a body about a given

axis is equal to the product of its rotational moment of inertia and the rotational acceleration around this axis:

$$\Sigma T_i = I_{ii} \cdot \alpha_i \tag{4.2}$$

Analogous to translational systems it holds that T_i equals the resultant moment, I_{ii} is the mass moment of inertia and α_i is the angular acceleration, all measured around the i-axis.

Here the mass moment of inertia (MMoI) depends upon the mass distribution of a vehicle is measured in $[kg \cdot m^2]$. MMoI can be calculated around any arbitrary axis, but for convenience applies only to the three principal axes in this study, resulting in an Ixx, Iyy and Izz. It can generally be stated that the closer all components of the vehicle are towards the origin of the considered reference frame, the lower the respective MMoI are. Low MMoI are favorable for quick responses and high agility, whereas high MMoI are typically useful for additional stability and smoothing of motion, because of the reduced angular accelerations.

It can be concluded that the sum of forces and the sum of moments is of importance for the (angular) accelerations of the vehicle. The external forces and moments are typically a function of the aerodynamic loading and the road conditions. The internal forces and moments are dependent on the operator, the powertrain and the suspension geometry and settings.

The combination of these internal and external forces and moments makes vehicle dynamics an interesting but extensive area of research. Because of the extensive available theory, it is necessary to identify the vehicle dynamics objectives for this thesis study. These objectives determine the complexity of the vehicle dynamics model, which has implications on the required governing equations.

Vehicle Dynamics simulation objective

In order to determine which accuracy the vehicle dynamics model should possess, it is necessary to estimate which vehicle motions are likely to occur. This is because driving situations which include drifting of the vehicle is difficult to simulate due to the non-linear behavior of the tires, whereas steady maneuvers such as cruising is relatively straightforward.

For this study it is the objective to assess the performance of vehicles during its cruise phase, where steady cross-wind flows are acting upon the vehicle. Depending upon the selected cross-wind flow spectrum this will therefore exclude drifting. As a start it is assumed that the operator does not respond the incoming cross-wind flow, by means of actively keeping the steering wheel fixed. During this maneuver it is assumed that the velocity of the vehicle is kept constant.

With these boundary conditions it is aimed to assess the differences in the heading angle, roll angle and total lateral displacement of the vehicle over time. These angles and displacements are solely the result of the asymmetric aerodynamic loading.

The total lateral displacement is a direct measure for the operator safety as this displacement could interfere with lane boundaries or traffic.

The tool should include vehicle and suspension settings which are adjustable, in order to assess the influence of individual factors upon the lateral displacement. This will be especially useful in order to compare the hardware differences between typical combustion engine vehicles and electric vehicles. These options should therefore include the total mass, the mass inertia moment around all three principal axes and the center of gravity position. Additionally it should be possible to vary the aerodynamic loading expressed in terms of force and moment coefficients around all three principal axes. In order to simulate the motion of the vehicle it is essential that the suspension geometry and characteristics are included as well. The extent of which this is simulated depends upon the used *Equations of motion*, which are discussed in more detail within section 4.2. In order to examine the contributions of different vehicle dynamics parameters, it is essential that the vehicle wheelbase, the distances between the front and rear axle, the center of gravity location, and suspension stiffness and damping values can be modified.

Stability criterions, laws and regulations

The allowed combined total lateral displacement should be constructed carefully in order to discard unsafe vehicle designs. Unsafe vehicles are here defined as vehicles which show excessive values in lateral displacement, heading, yaw and roll angles and accelerations.

In order to comply with vehicle standards and best design practices, a literature study was performed on existing stability criterions and regulations. Using enquiries within the NHTSA (National Highway Traffic and Safety Administration) and the SAE International (Society of Automotive Engineers). The NHTSA is an organization which aims to achieve a higher safety on the (American) roads by attempting to minimize the amount of crashes through various means.

The SAE on the other hand is a knowledge base institute which aims at delivering technical design standards for both the automotive and aerospace industry.

Unfortunately neither of these organizations was able to deliver a design standard, or any tangible design metrics such as allowed yaw angle, or yaw acceleration for a given aerodynamic loading. Discussions with three staff members from different large automotive aerodynamic design departments (Tesla Motors, Chrysler and Volkswagen) it became apparent that there are indeed no such regulations available.

It is therefore up to the design department to establish their own set of requirements and objectives, which together will determine the vehicle characteristics up to a certain extent.

Discussions with the Tesla Motors aerodynamic design staff it was decided that the constraints upon the maximum allowed lateral displacement equals 2 meter when the vehicle travels with 30 m/s for 1.5 second. This corresponds to a lateral displacement of 2 meter over a course of 45 meter in longitudinal direction.

The 2 meter lateral displacement constraint is a maximum as this would yield exceeding the lane width after which a collision with either obstacles or other traffic to is likely to occur.

The 1.5 second threshold was taken as the average reaction time for humans in traffic situations. [47] Here it is noted that the reaction time interval is subject to many factors. In order to keep a safety margin it was decided to elongate the 1.5 seconds towards 2 seconds within the study.

For now there is no official constraint employed upon the maximum allowed roll and yaw angle, rate or acceleration. Instead it was chosen that the various angles, rates or accelerations from different geometries can simply be compared to one another. When all other factors such as suspension settings are kept similar it holds that the lower the respective values, the better it is in terms of safety and comfort.

4.2 Governing equations of motion

This section discusses all governing equations that play a role within the vehicle dynamics simulations. The vehicle consists of coupled springs, masses and dampers, which is excited within this study by external aerodynamic forces and moments. This in turn results into translation and rotation of the vehicle. The traditional bicycle model is a popular choice in order to simulate the dynamics of a vehicle. This model which is shown in figure 4.3 allows lateral and rotational dynamics simulations, without requiring detailed suspension settings. This bicycle model can afterwards be tailored in order to draw conclusions about the lateral dynamics performance due to an aerodynamic input.

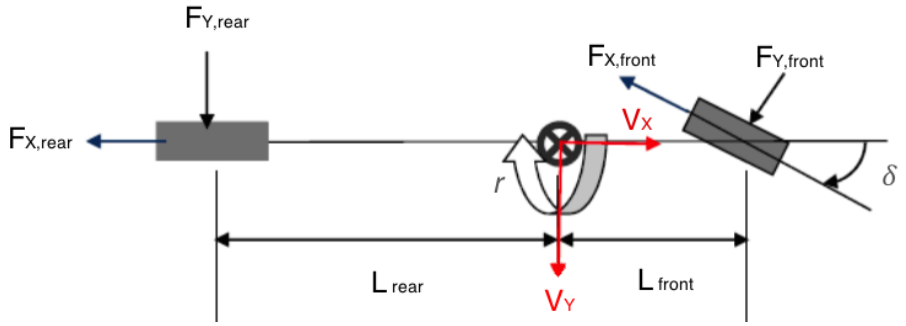

Figure 4.3: The traditional 2 DOF bicycle model is used as basis [5]

Within figure 4.3 the following assumptions and simplifications apply:

- No weight transfer is included
- There is no rolling or pitching of the vehicle
- The tire characteristics and responses are in the linear range
- Constant (slowly varying) forward velocity (steady-state behavior)
- No aerodynamic effects apply
- No suspension dynamics are included
- No steering dynamics nor suspension or steering compliance
- There are no aligning torque effects
- Only applies to a horizontal road surface without bumps
- Applies only to small angles of the tire-sideslip

The model can be used in order to study the following behavior:

- The effects of front and rear cornering stiffness values
- The effect of the center of gravity position
- The effects of lateral load transfer
- Consequences of steering input on yaw and body side-slip
- The effect of longitudinal velocity on stability

The main input to the system is a steering angle δ, which results in the assessment of the lateral dynamics of the vehicle including the yaw rate and acceleration. Since this study excludes steering input, the steering input angle δ is always zero. Instead of using the steering input angle the governing equations can be modified to also include an aerodynamic loading instead of the forces generated by controlling the steering wheel to assess the lateral dynamics of the vehicle. In addition it is also possible to study the rolling behavior of the vehicle provided that a roll stiffness and damping is set.

The free body diagram narrows down as presented in figure 4.4, where there are aerodynamic forces and moments, but without steering forces:

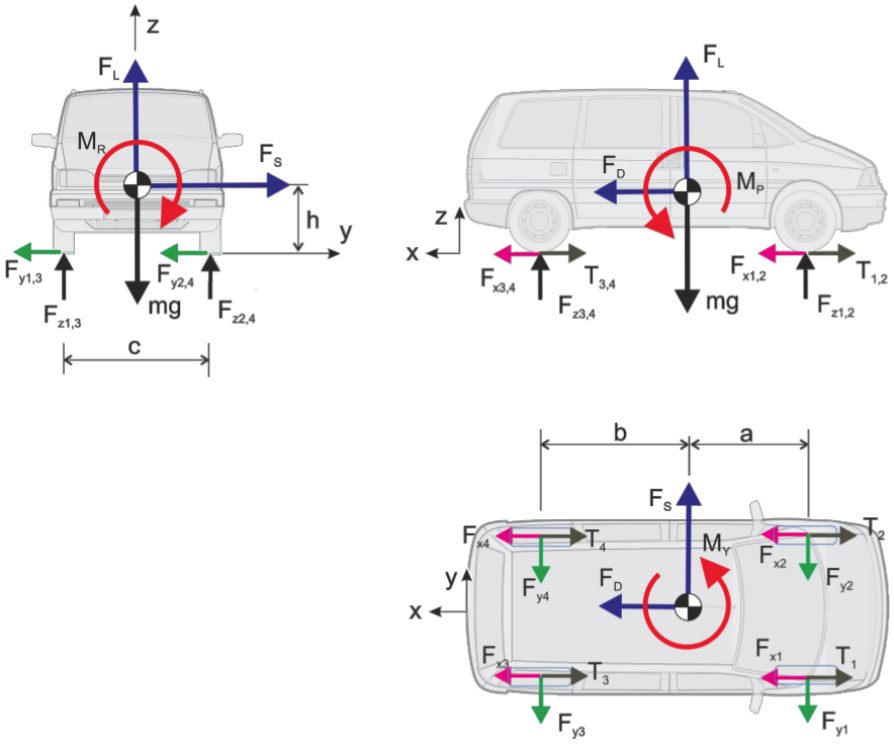

Figure 4.4: Free body diagram of the vehicle

.

Within figure 4.4 the indices indicate the respective wheel at which the forces occur. Here 1 is the right front wheel, 2 is the left front wheel, 3 is the rear right wheel, and 4 is the left rear wheel. The corresponding Newtonian equations that apply to this free body diagram are given in equations 4.3 - 4.5, where the forces are positive in the direction of the respective axis. All equations hold within the vehicle reference frame.

$$\Sigma F_x = T_1 + T_2 + T_3 + T_4 - F_{x1} - F_{x2} - F_{x3} - F_{x4} - F_D = m \cdot a_x \quad (4.3)$$

$$\Sigma F_y = -F_{y1} - F_{y2} - F_{y3} - F_{y4} + F_S = m \cdot a_y \quad (4.4)$$

$$\Sigma F_z = F_{z1} + F_{z2} + F_{z3} + F_{z4} - m \cdot g + F_L = m \cdot a_z \quad (4.5)$$

In addition to Newtons second law in the x, y, z direction, the moments equations around all three axes can be established as well.

In contrast with the force equations which were shown in equation 4.3 - 4.5, the moment equations also involve damping c and stiffness k contributions. The damping values which are used for this study is the roll and yaw damping, around the x and z axis respectively. Only the x axis features a roll stiffness as well. The damping contribution around the y axis is negligible because it is most effective at braking and take-off where wind-gust is least effective. Both damping contributions are by definition opposite to the rotation of motion, and a function of the angular rate.

Analogous to the equations shown in equations 4.3 - 4.5 a positive moment can be distinguished by applying the right-hand rule around the respective axes. The resulting moment equations are shown in equations 4.6 - 4.9:

$$\begin{aligned} \Sigma M_x = \quad & M_R + F_{z1} \cdot \frac{c}{2} + F_{z3} \cdot \frac{c}{2} - F_{z2} \cdot \frac{c}{2} - F_{z4} \cdot \frac{c}{2} \\ & - F_{y1} \cdot h - F_{y2} \cdot h - F_{y3} \cdot h - F_{y4} \cdot h \\ & - \mathrm{c}_{roll} \cdot \dot{\varphi} - \mathrm{k}_{roll} \cdot \varphi \quad = I_{xx} \cdot \ddot{\varphi} \end{aligned} \tag{4.6}$$

$$\begin{aligned} \Sigma M_y = \quad & M_P + F_{z1} \cdot a + F_{z2} \cdot a - F_{z3} \cdot b - F_{z4} \cdot b \\ & + T_1 \cdot h + T_2 \cdot h + T_3 \cdot h + T_4 \cdot h \\ & - F_{x1} \cdot h - F_{x2} \cdot h - F_{x3} \cdot h - F_{x4} \cdot h \quad = I_{yy} \cdot \ddot{\theta} \end{aligned} \tag{4.7}$$

$$\begin{aligned} \Sigma M_z = \quad & M_Y + T_1 \cdot \frac{c}{2} + T_3 \cdot \frac{c}{2} - T_3 \cdot \frac{c}{2} - T_4 \cdot \frac{c}{2} \\ & - F_{x1} \cdot \frac{c}{2} - F_{x3} \cdot \frac{c}{2} + F_{x2} \cdot \frac{c}{2} + F_{x4} \cdot \frac{c}{2} \\ & - F_{y1} \cdot \frac{c}{2} - F_{y2} \cdot \frac{c}{2} + F_{y3} \cdot \frac{c}{2} + F_{y4} \cdot \frac{c}{2} \\ & - \mathrm{c}_{yaw} \cdot \dot{\psi} \quad = I_{zz} \cdot \ddot{\psi} \end{aligned} \tag{4.8}$$

In equations 4.6 - 4.9 it is assumed that the aerodynamic forces and moments act upon and around the center of gravity. Typically within CFD software suites one can assign the location around which the pressure distribution is integrated into forces and moments manually, where the location of the center of gravity could be a logical choice.

Note that the origin of the reference frame is on the center aft of the vehicle, on the ground plane. The reason why the reference frame is not located within the center of gravity is this is impractical given the different employed yaw angles and mass distributions that are studied.

4.3 Vehicle mass moments of inertia

As was discussed in section 4.1, the mass moments of inertia is a measure for the extent to which an object resists rotational acceleration about a particular axis. The mass moment of inertia of assemblies which consist of multiple components such as a vehicle can be obtained using equation 4.9. Within equation 4.9 it is stated that the total inertia around a given axis can be found by discretizing all components and multiplying the infinitesimal mass contributions by the distance towards the center of gravity squared:

$$I_{x,y,z} = \Sigma m_i \cdot r_i^2 \tag{4.9}$$

This operation can be done manually, or using built-in CAD features. The latter is favorable due to the associated visual representation of the components. Since the geometry needs to be implemented in CAD anyways in order to prepare the vehicle body for aerodynamic analysis, it was chosen to use the built-in CAD feature. The most important components are drawn as well, such as a power train, wheels, drivers and seats in order to obtain a relatively accurate estimation of the mass moments of inertia around the three axes. The result is shown in figure 4.5, where the conventional and electrical architecture are depicted.

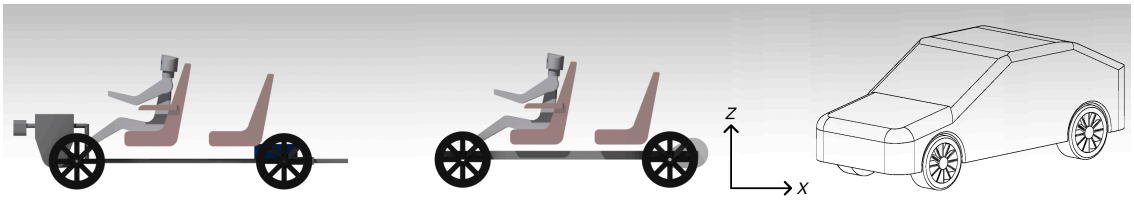

Figure 4.5: Vehicle inertia CAD model - Conventional (L), Electric (M), 3D view (R)

For both powertrains the most popular layout is used, i.e. an internal combustion engine in the front or an electric motor in the rear. The electric battery is shown in between the front and rear wheels, and on the left one can identify a blue fuel tank in between the rear wheels. The mass and respective mass location construct the mass moment of inertia. Therefore it is useful to create a mass and location breakdown of both vehicles, which is presented in table 4.1 and 4.2. All coordinates are measured with respect to the origin of the vehicle coordinate system which is shown in figure 4.5.

From table 4.1 it follows that the estimated mass of the electric vehicle is 410 kg or roughly 30% higher than its conventional combustion engine counterpart. The corresponding mass moments of inertia around all three principal axes are are also higher for the electric vehicle; I_{xx} is increased by roughly 30%, I_{yy} by around 3% and I_{zz} with approximately 8%. The relatively low increments in mass moments of inertia are a result of a centralized distribution of the mass components compared to the combustion vehicle.

Combustion vehicle	Mass	X coordinate	Y coordinate	Z coordinate
Body	400	-1.991	0.000	0.180
Engine	250	-3.318	-0.077	0.266
Driver	75	-2.327	-0.400	0.552
Co-driver	75	–2.327	0.400	0.552
Front seat	25	-2.085	-0.400	0.477
Front seat	25	-2.085	0.400	0.477
Rear seat	35	-1.123	0.000	0.431
Fuel tank	50	-0.800	0.250	0.100
4 wheels	140	-2.000	0.000	0.000
Miscalleneous	400	-1.870	0.000	0.050
Totals				
Center of gravity	1425	-2.150	-0.008	0.193
$Ixx = 356\ [kg \cdot m^2]$				
$Iyy = 1769\ [kg \cdot m^2]$				
$Izz = 1901\ [kg \cdot m^2]$				

Table 4.1: Combustion vehicle mass moment of inertia breakdown

Electric vehicle	Mass	X coordinate	Y coordinate	Z coordinate
Body	400	-1.991	0.000	0.180
Electric motor	60	-0.500	0.000	0.052
Driver	75	-2.327	-0.400	0.552
Co-driver	75	-2.327	0.400	0.552
Front seat	25	-2.085	-0.400	0.477
Front seat	25	-2.085	0.400	0.477
Rear seat	35	-1.123	0.000	0.431
Electric battery	600	-1.880	0.000	0.075
4 wheels	140	-2.000	0.000	0.000
Miscalleneous	400	-1.870	0.000	0.050
Totals				
Center of gravity	1835	-1.884	0.000	0.126
$Ixx = 466\ [kg \cdot m^2]$				
$Iyy = 1824\ [kg \cdot m^2]$				
$Izz = 2067\ [kg \cdot m^2]$				

Table 4.2: Electric vehicle mass moment of inertia breakdown

4.4 Implementation in MATLAB

This section presents the documentation of the lateral vehicle dynamics design tool and its implementation within MATLAB . The proposed MATLAB workflow structure is shown in figure 4.6. Within this figure one can distinguish four main stages within the vehicle dynamics model structure. The model commences using the main Run me file, which has a Graphical User Interface (GUI). The boundary conditions are assembled here and delivered to the simulation definition. The simulation information is then used within the vehicle motions domain which contains the governing equations of motion. The results are visualized in order to draw conclusions about the vehicle design in terms of lateral dynamic performance.

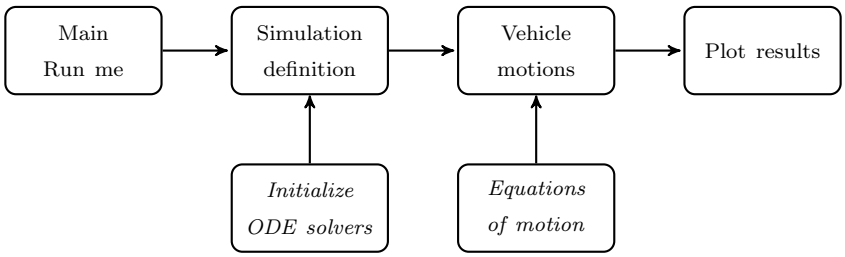

Figure 4.6: Vehicle dynamics MATLAB model structure

This model structure can be constructed efficiently using MATLAB functions.
The vehicle dynamics model has a main file called *Run me*, and two subunctions called *Simulations* and *Movements*. These three files are discussed within the next three subsections.

4.4.1 Main: Run me

This main routine is the backbone of the vehicle dynamics model. The function first collects and organizes all input data, which is performed within 12 identical sub functions, which represent 12 different vehicles. Within each of these 12 sub functions the aerodynamic input data, which consists of forces - and moment coefficients, are automatically read from solution files from the aerodynamic solver. The vehicle dynamic parameters are hard-coded numbers such as the position of the center of gravity. Within each of the 12 sub functions the user can easily switch between the "Electric vehicle vehicle dynamics parameter set" and the "Conventional ICE vehicle vehicle dynamics parameter set" in order to easily set the simulation vehicle type.

All aerodynamic forces and moments are assembled within 12 unique forces and moments vectors. Analogous to these vectors another 12 unique vectors are initialized which contain all vehicle dynamics related parameters.

After the input data collection the user is prompted to enter boundary conditions such as the duration of the simulation and the longitudinal velocity of the vehicle. The combined information comprises the complete set of input parameters.

The vectors containing the boundary conditions, the vehicle dynamics and the force and moment of the first vehicle are now sent to a new function called *Simulations*, which controls the solving procedure of the ODE's using another sub function *Movements*. These functions are explained in more detail in subsection 4.4.2, and ultimately yield the trajectory in planar $X-Y$ coordinates, and information about the (rate of) heading, yaw and roll angles.

This information is visualized using trajectory figures and figures which show the course of a certain variable over the duration of the simulation. Using this information conclusions can be drawn upon the sensitivity of the lateral dynamics of a vehicle to a certain geometry design variable.

4.4.2 Simulations

With the initialization phase completed the first function *Simulations* is created to control the simulations. These simulations need to solve the equations listed in equations 4.3 - 4.8, which can also be written in the format of equation 4.10:

$$\mathbf{M}\ddot{\mathbf{x}} + C\dot{\mathbf{x}} + K\mathbf{x} = \mathbf{F}_{external} \tag{4.10}$$

where

$$\mathbf{x} = [\, X\ Y\ Z\ \varphi\ \theta\ \psi \,]^T \tag{4.11}$$

resulting into a set of second order ordinary differential equations (ODE):

$$\begin{bmatrix} m & 0 & 0 & 0 & 0 & 0 \\ 0 & m & 0 & 0 & 0 & 0 \\ 0 & 0 & m & 0 & 0 & 0 \\ 0 & 0 & 0 & I_{XX} & 0 & 0 \\ 0 & 0 & 0 & 0 & I_{YY} & 0 \\ 0 & 0 & 0 & 0 & 0 & I_{ZZ} \end{bmatrix} \cdot \begin{bmatrix} \ddot{x} \\ \ddot{y} \\ \ddot{z} \\ \ddot{\varphi} \\ \ddot{\theta} \\ \ddot{\psi} \end{bmatrix} + \begin{bmatrix} 0 & 0 & 0 & 0 & 0 & 0 \\ 0 & 0 & 0 & 0 & 0 & 0 \\ 0 & 0 & 0 & 0 & 0 & 0 \\ 0 & 0 & 0 & c_r & 0 & 0 \\ 0 & 0 & 0 & 0 & 0 & 0 \\ 0 & 0 & 0 & 0 & 0 & 0 \end{bmatrix} \cdot \begin{bmatrix} \dot{x} \\ \dot{y} \\ \dot{z} \\ \dot{\varphi} \\ \dot{\theta} \\ \dot{\psi} \end{bmatrix} + \begin{bmatrix} 0 & 0 & 0 & 0 & 0 & 0 \\ 0 & 0 & 0 & 0 & 0 & 0 \\ 0 & 0 & 0 & 0 & 0 & 0 \\ 0 & 0 & 0 & k_r & 0 & 0 \\ 0 & 0 & 0 & 0 & 0 & 0 \\ 0 & 0 & 0 & 0 & 0 & 0 \end{bmatrix} \cdot \begin{bmatrix} x \\ y \\ z \\ \varphi \\ \theta \\ \psi \end{bmatrix} = \begin{bmatrix} F_X \\ F_Y \\ F_Z \\ M_X \\ M_Y \\ M_Z \end{bmatrix}$$

These ODE's can be solved using the ODE solving function within MATLAB .
When the system is solved all parameters including the vehicle's global position, velocity in x, y, z, angular velocity and angular accelerations.
The ODE solver within MATLAB requires the followings specifications:

- Explicit definition of the ODE
- Time interval for which the ODE needs to be solved
- Definition of the initial condition(s) or state(s)

The most common method of defining any ODE solver within MATLAB is by calling

$$Simulation = ode45\ (@\ Movements,\ [0\ \ t_f],\ \mathbf{x_0}); \tag{4.12}$$

The explicit definition of the second order ODE is in this case a coupled system with different states and therefore multiple second order ODE's.

These ODE's are handled within a dedicated sub-function called *Movements*. This sub-function is discussed in more detail in the next subsection 4.4.3.

The time interval of interest $[0\ t_f]$ for the vehicle trajectory is discretized within the ODE function in order to compute the state of the vehicle numerically.

The final term $\mathbf{x_0}$ is a vector which contains the initial values for each respective state or initial condition. In this specific study there are 7 states that describe the attitude of the vehicle, i.e. the lateral velocity v_y, yaw angle ψ, yaw rate r, roll angle ϕ, roll rate $\dot{\phi}$ and global coordinates X and Y. The pitch angle θ, angular rate $\dot{\theta}$ and acceleration $\ddot{\theta}$ are again not included due to the design of experiments - there is no braking or accelerating in longitudinal direction. Therefore the pitch performance was found to not be relevant for lateral displacement.

It is assumed that the vehicle enters the aerodynamic loading from an undisturbed, steady approach where v_x is constant and the above mentioned states are zero:

$$\mathbf{x_0} = [\,0\,0\,0\,0\,0\,0\,0\,]^T$$

There are different numerical solving schemes available within MATLAB which are able to solve the second order ODE. The different schemes all have their own distinct properties, robustness and name tag, which are listed in table 4.3:

ODE Solver	**Stiffness of ODE**	**Method**
ode45	Non-stiff	Runge-Kutta
ode23	Non-stiff	Runge-Kutta
ode113	Non-stiff	Adams
ode15s	Stiff	NDFs
ode23s	Stiff	Rosenbrock
ode23t	Moderately stiff	Trapezoidal rule
ode23tb	Stiff	TR-BDF2
ode15i	Fully implicit	BDFs

Table 4.3: Available ODE solvers within MATLAB

Here it is noted that the stiffness of the ODE solver is not a physical property of the system such as a spring. This ODE stiffness can be described as having time constants in a model that vary by several orders of magnitude. Different numerical schemes are used for stiff or non-stiff solvers, where each scheme has its own stability regions. That being said it holds that stiff ODE are best solved by a stiff solver, and vice-versa. Within this study the ODE's were found to be not stiff, based upon the observation that each ODE solver within MATLAB returned identical results with only seconds difference in computation time.

4.4.3 Movements

The function *Simulations* calls the function *Movements* in order to assess all the governing equations for all 7 vehicle states. These governing equations as they are discussed in chapter 4.2 need to be rewritten such that the (angular) acceleration is set explicitly instead of the sum of forces or moments. For the 7 required states it follows that there is little need for the sum of forces in the X and Z direction since the model assumes a constant longitudinal velocity and no movement in Z - direction. Furthermore the pitching moment equation around the Y - axis is also excluded from the analysis since the pitch angular dynamics are not included within the vehicle states. First the lateral acceleration is discussed, which after manipulations yields the first vehicle state; the lateral velocity:

$$\Sigma F_y = \quad -F_{y1} - F_{y2} - F_{y3} - F_{y4} + F_S \quad = m \cdot a_y \tag{4.13}$$

Rewriting equation 8.2 results into equation 8.3:

$$a_y = \frac{1}{m}\Big(- F_{y1} - F_{y2} - F_{y3} - F_{y4} + F_S\Big) \tag{4.14}$$

The lateral velocity is obtained by integrating the lateral acceleration and adding both the effect of the yaw angle times the forward velocity of the vehicle, and the roll induced lateral velocity:

$$v_y = \int_{t_0}^{t_f} \Big(a_y\Big)dt \quad + \quad v_x \cdot \int_{t_0}^{t_f} \Big(\dot{\boldsymbol{\psi}}\Big)dt \quad + \quad h_{cog} \cdot \int_{t_0}^{t_f} \Big(\ddot{\boldsymbol{\varphi}}\Big)dt \tag{4.15}$$

First the equation which describes the yaw acceleration needs to be integrated in order to obtain the actual yaw angle:

$$\begin{aligned} \Sigma M_z = \quad & M_Y + T_1 \cdot \frac{c}{2} + T_3 \cdot \frac{c}{2} - T_3 \cdot \frac{c}{2} - T_4 \cdot \frac{c}{2} \\ & -F_{x1} \cdot \frac{c}{2} - F_{x3} \cdot \frac{c}{2} + F_{x2} \cdot \frac{c}{2} + F_{x4} \cdot \frac{c}{2} \\ & -F_{y1} \cdot \frac{c}{2} - F_{y2} \cdot \frac{c}{2} + F_{y3} \cdot \frac{c}{2} + F_{y4} \cdot \frac{c}{2} \quad = I_{zz} \cdot \ddot{\psi} \end{aligned} \tag{4.16}$$

Rewriting moment equation 4.16 yields the yaw acceleration $\ddot{\boldsymbol{\psi}}$ explicitly:

$$\begin{aligned} \ddot{\boldsymbol{\psi}} = \quad & \frac{1}{I_{zz}}\Big(\; M_Y + T_1 \cdot \frac{c}{2} + T_3 \cdot \frac{c}{2} - T_3 \cdot \frac{c}{2} - T_4 \cdot \frac{c}{2} \\ & -F_{x1} \cdot \frac{c}{2} - F_{x3} \cdot \frac{c}{2} + F_{x2} \cdot \frac{c}{2} + F_{x4} \cdot \frac{c}{2} \\ & -F_{y1} \cdot \frac{c}{2} - F_{y2} \cdot \frac{c}{2} + F_{y3} \cdot \frac{c}{2} + F_{y4} \cdot \frac{c}{2} \; \Big) \end{aligned} \tag{4.17}$$

The contribution of the lateral displacement of the vehicle center of gravity due to the body roll compliance is small (around 2%) compared to the heading angle. Despite this observation its effect is still implemented as this will provide addition insight into the vehicle motions.
The equation for the roll angular acceleration is governed by equation 4.8, which is repeated here in equation 4.18:

$$\begin{aligned} \Sigma M_x = \quad & M_R + F_{z1} \cdot \frac{c}{2} + F_{z3} \cdot \frac{c}{2} - F_{z2} \cdot \frac{c}{2} - F_{z4} \cdot \frac{c}{2} \\ & -F_{y1} \cdot h - F_{y2} \cdot h - F_{y3} \cdot h - F_{y4} \cdot h \\ & -\mathrm{c}_{roll} \cdot \dot{\varphi} - \mathrm{k}_{roll} \cdot \varphi \quad = I_{xx} \cdot \ddot{\varphi} \end{aligned} \tag{4.18}$$

Rewriting equation 4.18 yields the roll acceleration $\ddot{\phi}$ explicitly:

$$\begin{aligned} \ddot{\boldsymbol{\phi}} = \quad & \frac{1}{I_{xx}} \Big(\; M_R + F_{z1} \cdot \frac{c}{2} + F_{z3} \cdot \frac{c}{2} - F_{z2} \cdot \frac{c}{2} - F_{z4} \cdot \frac{c}{2} \\ & -F_{y1} \cdot h - F_{y2} \cdot h - F_{y3} \cdot h - F_{y4} \cdot h \\ & -\mathrm{c}_{roll} \cdot \dot{\varphi} - \mathrm{k}_{roll} \cdot \varphi \; \Big) \end{aligned} \tag{4.19}$$

Using the initial conditions $\psi = 0$, $\dot{\psi} = 0$, $\ddot{\psi} = 0$, $\phi = 0$, $\dot{\phi} = 0$ and $\ddot{\phi} = 0$ equations 4.17 and 4.19 can be solved using the earlier described ODE solvers.

The final two vehicle states are the global X and Y position. These coordinates can be established by using equations 8.9 and 8.10, which describe the longitudinal and lateral velocity of the vehicle:

$$\dot{\boldsymbol{X}} = v_x \cdot cos(\boldsymbol{\psi}) - v_y \cdot sin(\boldsymbol{\psi}) \tag{4.20}$$

$$\dot{\boldsymbol{Y}} = v_x \cdot sin(\boldsymbol{\psi}) + v_y \cdot cos(\boldsymbol{\psi}) \tag{4.21}$$

Within equations 8.9 and 8.10 v_x is a constant value, and v_y can be obtained by solving the ODE presented in equation 8.4.

This concludes Chapter 8: Implementation in MATLAB .
Using this vehicle dynamics design tool it is possible to simulate a vehicle's dynamic response to an aerodynamic input loading.

The next part III documents the process of combining Aerodynamics and Vehicle Dynamics in order to draw conclusions on their interactions.

Part III

Results

Chapter 5

Results

The results that are obtained by the CFD simulations can now be implemented in the MATLAB script in order to assess the dynamic response of the vehicle. Two main design choices which directly arise are shape modifications to be applied to the reference vehicle, and the geometry definition of the reference vehicle. The research conducted by Toppinga provides a good starting point, as Toppinga researched which shape modifications are useful for drag reductions in symmetric flow conditions. [55] Although the dynamic response of the vehicle is not included in Toppinga's thesis, it is very useful to assess the aerodynamic results from this study first. Here it holds that the geometry of the reference vehicle is the result of many considerations. These different considerations and the final outcome are discussed in section 5.1.

The drag coefficient and the lateral displacement are the performance metrics used for evaluating the effect of the respective design variables. Although the drag coefficient and the vehicle trajectory are most important, other metrics are also of importance in order to identify the composition of these two metrics. For instance, from a comfort perspective it is useful to establish and compare both the roll and yaw angles, rates and accelerations. Considering such variations different states of the vehicle are presented as well as future references.

Within this study the vehicle responds only to the applied aerodynamic loading, without steering input. It is therefore important to know which metrics are important. For this reason first the reference vehicle is studied without any geometry modification. After this reference run the vehicle dynamics are studied in order to understand which vehicle dynamics parameters are most important. Using this information as a basis the vehicle geometry can systematically be modified and evaluated upon their performance.

5.1 Reference vehicle simulations

Within this section the results from the reference vehicle vehicle are discussed. The process of constructing a reference vehicle is first discussed, where assumptions and design choices are discussed. Afterwards the results of the aerodynamic and dynamic simulations are presented.

Constructing a reference vehicle

The geometry of the reference vehicle is the result of many considerations. On one hand the geometry should not be too complex in order to obtain generic trends instead of trends which are only valid for a specific vehicle. A more detailed vehicle typically also introduces complex flow structures which do not necessarily add value to the quality of the study. On the other hand the vehicle should also not be too simple, because the obtained results might not be applicable to modern vehicles.

It was chosen to use a fastback vehicle type as baseline reference vehicle, since this was a pronounced preference from Tesla Motors' aerodynamic staff. In addition to keeping the vehicle shape not too specific, it was chosen to apply additional simplifications in order to reduce the computational requirements per simulation.

Within literature it is a popular choice to exclude wheel housings and wheels of a vehicle; for example both the Ahmed reference vehicle and the SAE vehicle both do not have wheels. [1] [9] Toppinga reports that although removing the wheels is a big simplification compared to a realistic vehicle, the results of the remaining body are still useful. [55] The interaction of the flow around rotating wheels and their housings tend to substantially alter the underbody and lower body flow, which results in an increasing drag and lift coefficient. Toppinga compared reference vehicles with and without (rotating) wheels, and concluded that although the results are substantially different, the trends within the general vehicle flow effects remain similar.It was concluded that the offset in both the drag and lift coefficient is relatively constant throughout systematic geometry modifications. The many variables in the wheel (housing) design result in additional complexity within the aerodynamic simulations. This additional level of complexity does not contribute to the general understanding of the effects of systematic geometry modifications applied upon the vehicle body. Therefore it was chosen to not include wheels within this study.

This simplification does implicate that the vehicle dynamics model now receives has an unrealistic value for the drag coefficient due to the absence of the wheels. The effect upon the lateral displacement however is negligible given the assumed constant forward velocity. The resulting moments and side force coefficients are also affected by the absence of the wheels. This is a simplification of the simulation, therefore the simulation results are only useful for identifying trends and comparing the differences between the vehicle configurations rather than collecting absolute values.

It was decided to apply of edge radii around most edges of the vehicle. Without these edge radii the flow will tend to separate at the edges, which leads to a pressure

field around the vehicle with various separated flow zones resulting in an increased drag coefficient. Since modern vehicles are streamlined shapes, the results will be more representable when different edge radii are present and comparable to existing designs. A survey is performed among different types of Mercedes, Audi and Tesla vehicles in order to collect geometry information such as edge radii and surface angles of makes of automobiles, where the most relevant conclusions on the various edge radii are listed in the "Survey range" column within table 5.1. This geometry information is used for constructing the baseline geometry, and assists in determining the limits of geometry variables.

These considerations eventually resulted in the baseline reference vehicle geometry which is shown in figure 5.1:

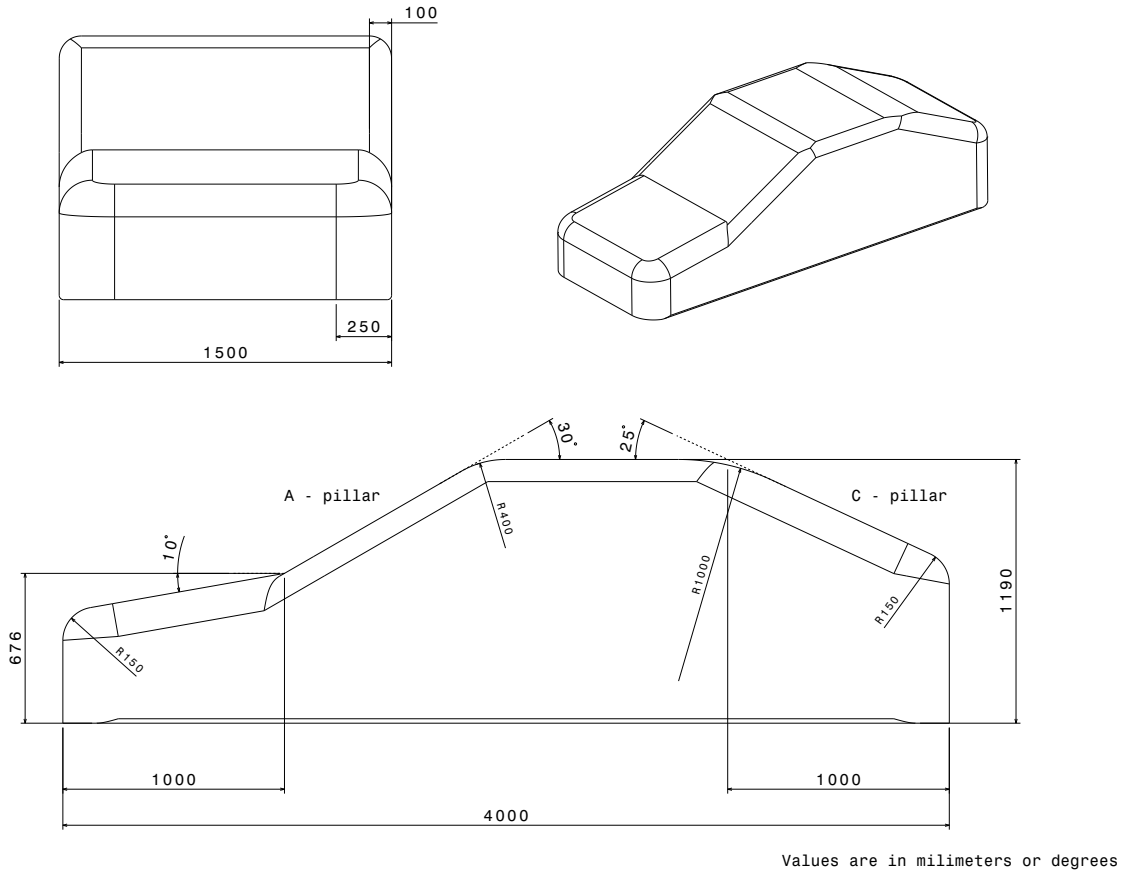

Figure 5.1: Reference vehicle geometry

This baseline geometry presented in figure 5.1 will systematically be modified using different angles and edge radii as is indicated in the "Range" column in table 5.1. By doing so one obtains an extensive dataset which contains information on the effect of shape modifications on the pressure field around the vehicle. In turn these changes in the pressure field can be used to draw conclusions on aerodynamic induced (lateral) vehicle dynamic effects.

Geometry metric	Value	Unit	Range	Survey range
Total length	4000	[mm]	-	-
Total width	1500	[mm]	-	-
Total height	1190	[mm]	-	-
Projected surface area	1.785	[m^2]	-	-
Length first compartment	1000	[mm]	-	-
Length center compartment	2000	[mm]	-	-
Length rear compartment	1000	[mm]	-	-
Length rear compartment	1000	[mm]	-	-
Front arrow angle	0	[degrees]	[0 - 5 - 10 - 15]	[0 - 10]
Rear taper angle	0	[degrees]	[0 - 5 - 10 - 15]	[0 - 10]
Hood angle	10	[degrees]	-	-
Front window angle	30	[degrees]	[25 - 30 - 35]	[25 - 40]
Rear window angle	25	[degrees]	[15 - 20 - 25]	[0 - 30]
Tumblehome angle	0	[degrees]	[0 - 5 - 10 - 15]	[0 - 30]
Nosecone radii (left/right)	250	[mm]	-	[150 - 300]
Bumper - hood radius	150	[mm]	-	[100 - 200]
Hood radii (left/right)	150	[mm]	-	[100 - 200]
Hood - front window radius	1000	[mm]	-	[0 - 100]
A - pillars (left/right)	100	[mm]	[50 - 100 - 150]	[50 - 100]
Front window - roof radius	400	[mm]	-	[200 - 600]
Roof radii (left/right)	100	[mm]	-	[30 - 100]
Roof - rear window radius	1000	[mm]	-	[100 - 1000]
C - pillars (left/right)	150	[mm]	[100 - 150 - 200]	[100- 200]
Rear window - bumper radius	150	[mm]	-	[100 - 200]
Rear bumper radii (left/right)	250	[mm]	-	[100 - 250]
Lower sides radii (left/right)	20	[mm]	-	[0 - 50]
Vehicle dynamics metric				
Front wheel - vehicle nose	0.75	[m]	-	-
Wheelbase	2.5	[m]	-	-
Rear wheel - vehicle aft	0.75	[m]	-	-
Roll stiffness	100000	[Nm / rad]	-	-
Roll damping	4540	[Nm / (rad/s)]	-	-
Friction coefficient μ (between tires and the ground)	0.8	[-]	-	-

Table 5.1: Baseline geometry metrics

Constructing the aerodynamic mesh

The vehicle geometry from figure 5.1 is drawn within ANSYS meshing software in order to construct the aerodynamic mesh. The vehicle geometry is built up such that the incident cross-wind flow angle can be adjusted by changing a single parameter. This is particularly useful for generating different meshes of the same geometry under a different incident cross-wind flow. A control volume is created around the vehicle geometry together with a so called "Body of Influence" - which is used for locally refining the amount of control points within the mesh where enhanced accuracy is desired. The resulting mesh is shown in figure 5.2, where the markers are visible which are used to assign appropriate boundary conditions.

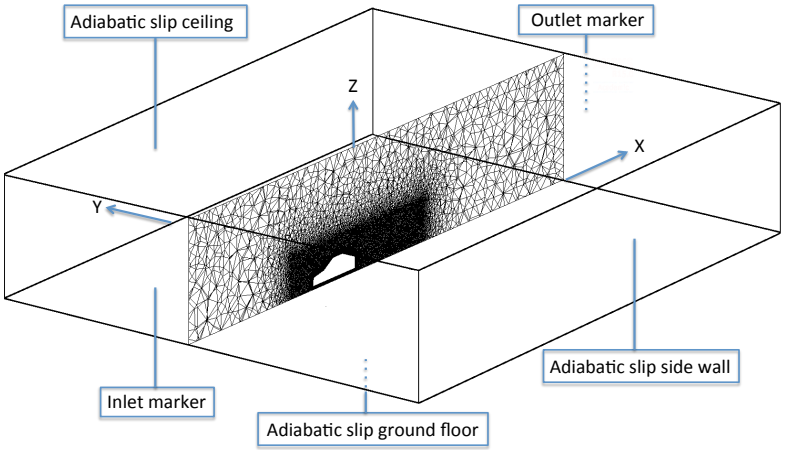

Figure 5.2: 3D view of the mesh

Within figure 5.3 a detailed view of the mesh on the XZ-plane is presented. Within this picture the Body of Influence is clearly visible, as well as the inflation layers which are applied at the complete surface of the vehicle geometry.

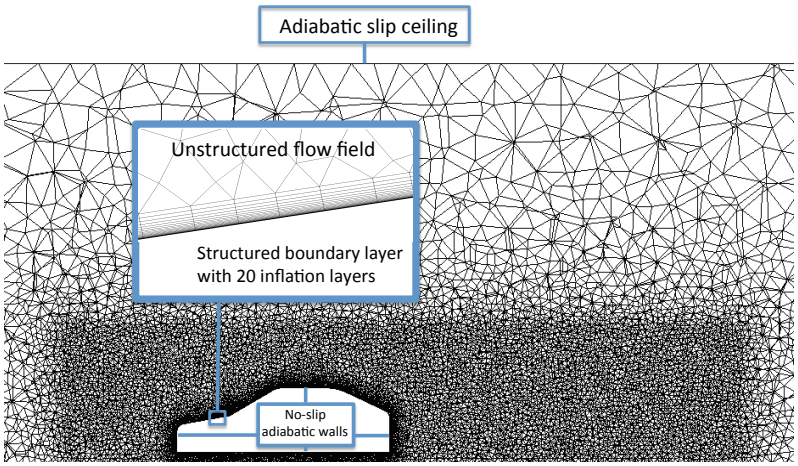

Figure 5.3: Detailed view of the mesh at the XZ-plane

The inflation layer is applied in order to capture the flow phenomena within the

boundary layer of the vehicle surface, and consists of 20 structured cell layers. The thickness of these cells grow orthogonally to the surface using a growth factor of 1.2, resulting in a total total thickness of 13$[mm]$. More information about the construction of the mesh can be seen in Appendix V.

Aerodynamic simulation setup

The simulation setup and boundary conditions which are used within this baseline reference simulation is identical for all performed simulations within this study. These general simulation assumption and boundary conditions which are used in all simulations are all listed below:

- RANS equations are used in combination with a Spalart - Allmaras turbulence scheme, which has by default a free-stream turbulent kinetic energy per unit mass of 3.375 m^2/s^2
- The pressure field is assumed to be converged once the residual (the difference between two subsequent results) of the density field becomes less than 10^{-7}.
- Throughout the entire flow field the Mach number (defined as $\frac{V}{a}$) remains below 0.3. This implies that the fluid is assumed to be incompressible and thus has no density variation.
- The fluid has a constant temperature throughout the domain, resulting in constant values for both the viscosity and specific heat.
- There is no heat transfer present between the air flow and the vehicle walls.
- The fluid is assumed to be isotropic, which implies that the quality of each material property is the same in every direction.
- Any external forces and moments such as gravity are neglected.
- There is no floor movement included in the analysis.
- All simulations are conducted with an inlet velocity of 30 m/s, resulting in a Reynolds number equal to $Re = 8.5 \cdot 10^6$ where $\rho = 1.225$ kg/m^3
- A no-slip boundary condition has been assigned to the vehicle body
- The digital boundaries such as the ceiling, side walls and road are treated with a slip boundary condition

The proposed model for the simulation studies have some inherent shortcomings, of which the most important ones are listed below:

- The flat underbody floor is not realistic, although electric vehicles have relatively smooth underbodies.
- The simulation of cooling flow is completely excluded within this study. From section 1.1 it was found that cooling flow typically adds 60 drag counts.
- The absence of (rotating) wheels, wheelhouses and realistic details is a major simplification.

Since all simulations use the same aerodynamic and settings, these considerations apply to all results.

Aerodynamic results

The results of the reference vehicle of the 0, 3 and 6 degrees cross-wind flow are presented in this subsection, starting with three surface pressure plots. In combination with among others longitudinal velocity plots one can distinguish the main flow effects upon the reference vehicle and the effect of the cross-wind flow angle. With this reference it is possible to compare the effect of shape modifications upon the main flow effects, allowing for a better understanding of the difference in force and moment coefficients and ultimately the lateral dynamic implications.

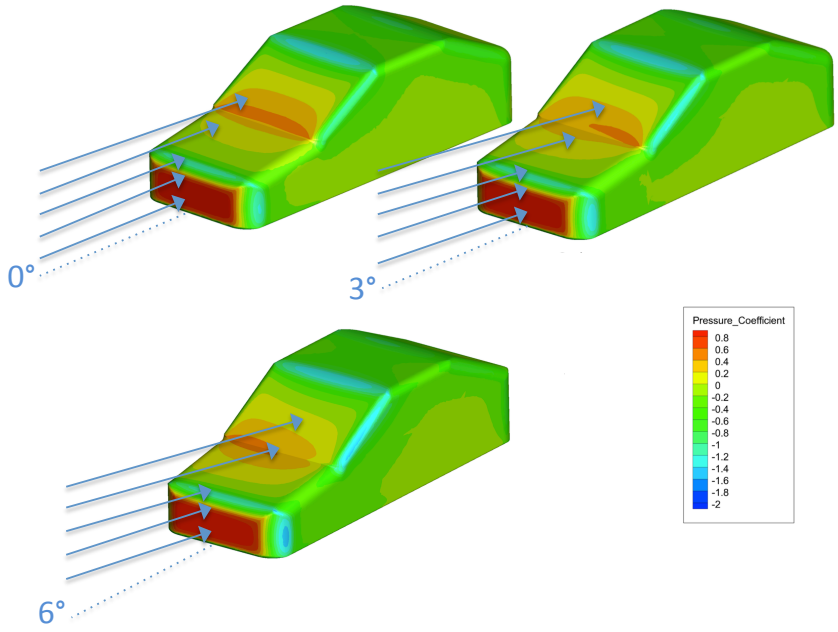

Figure 5.4: 0, 3 and 6 degrees pressure coefficient plots on the leeside front of the vehicle

Within figure 5.4 the three reference vehicles are shown with their respective surface pressure coefficient distribution plots as seen from the front leeside of the vehicle. Typical for vehicle shapes is the high pressure peak in front of the vehicle, indicated by the red pressure zone in front of the vehicle. [26] Beyond the vehicle nose the flow is accelerated over the side corners towards the sides, and towards the floor and engine compartment of the vehicle which can be seen by the (blue / green) low pressure zones which are located around the contour of the vehicle 'nose'.

Towards the vicinity of the front window the pressure starts to increase again where the surface pressure peak is reached on the lower side of the front window. This is indicated in figure 5.4 by the red pressure zone on the front window. The surface pressure contours of the 3 and 6 degrees cross-wind flow vehicles show different trends near the front window. The pressure peak of the vehicle which experiences a 3 degree cross-wind flow angle is shifted towards the leeside of the front window, whereas the pressure peak of the 6 degree cross wind flow is shifted towards the windward side of the vehicle.

The flow is afterwards accelerated over both the window - roof interface and the

so called A-pillars, which are the radiused pillars towards the side of the vehicle. During this stage the formation of the vehicle wake starts to form, where the flow around the vehicle starts to rotate and displace in lateral direction.

The vehicle wake shows typical flow structures where the flow is separated and the two typical predominant vortices originating from the rear C-pillars [26]. The wake aft of the three reference vehicles is visualized in figure 5.5:

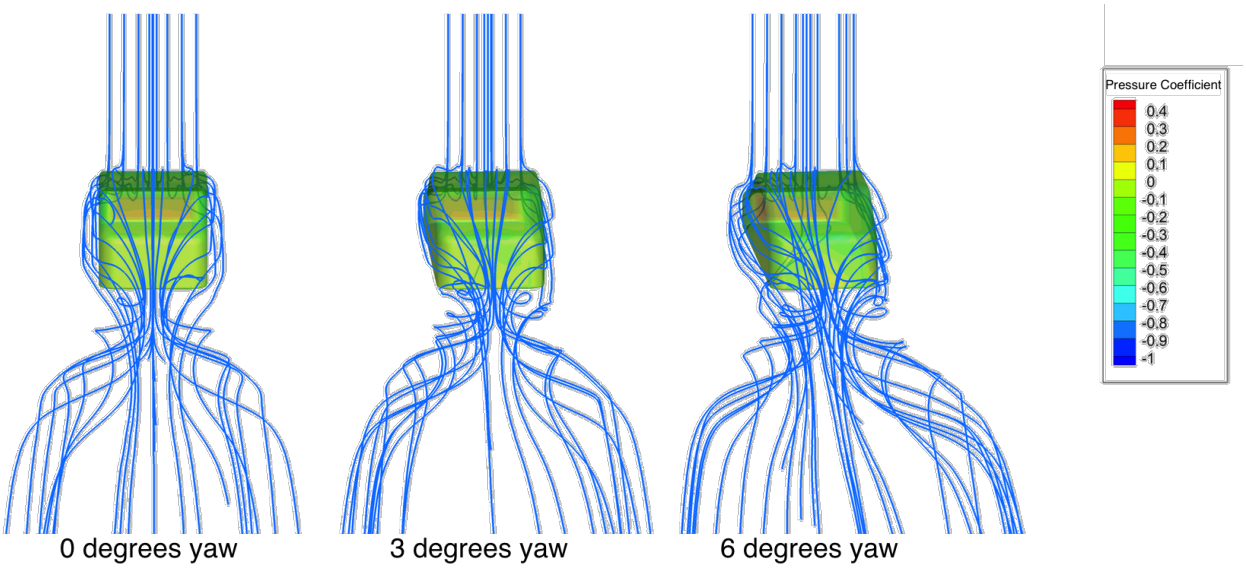

Figure 5.5: Stream traces aft of the vehicle inside the vehicle wake

It can be seen in figure 5.5 that the wake structure aft of the vehicle is affected by the different cross-wind flow angles. Not only does the wake appear to enhance, the vortices also appear to increase in strength with increasing cross-wind flow angle.

This trend can also be observed when the pressure contours along the ZX - plane is evaluated as is shown in figure 5.6. The low pressure region aft of the vehicle grows in magnitude when the cross-wind flow angle is increased, indicating that the turbulent wake becomes stronger in magnitude which results in an increase in vehicle drag. Another indication of the stronger wake is the formation of a high pressure zone above the low pressure zone within the wake of the simulation where a 6 degrees cross-wind flow is simulated. This high pressure zone was not present at the other simulations where the cross-wind flow was 0 or 3 degrees.

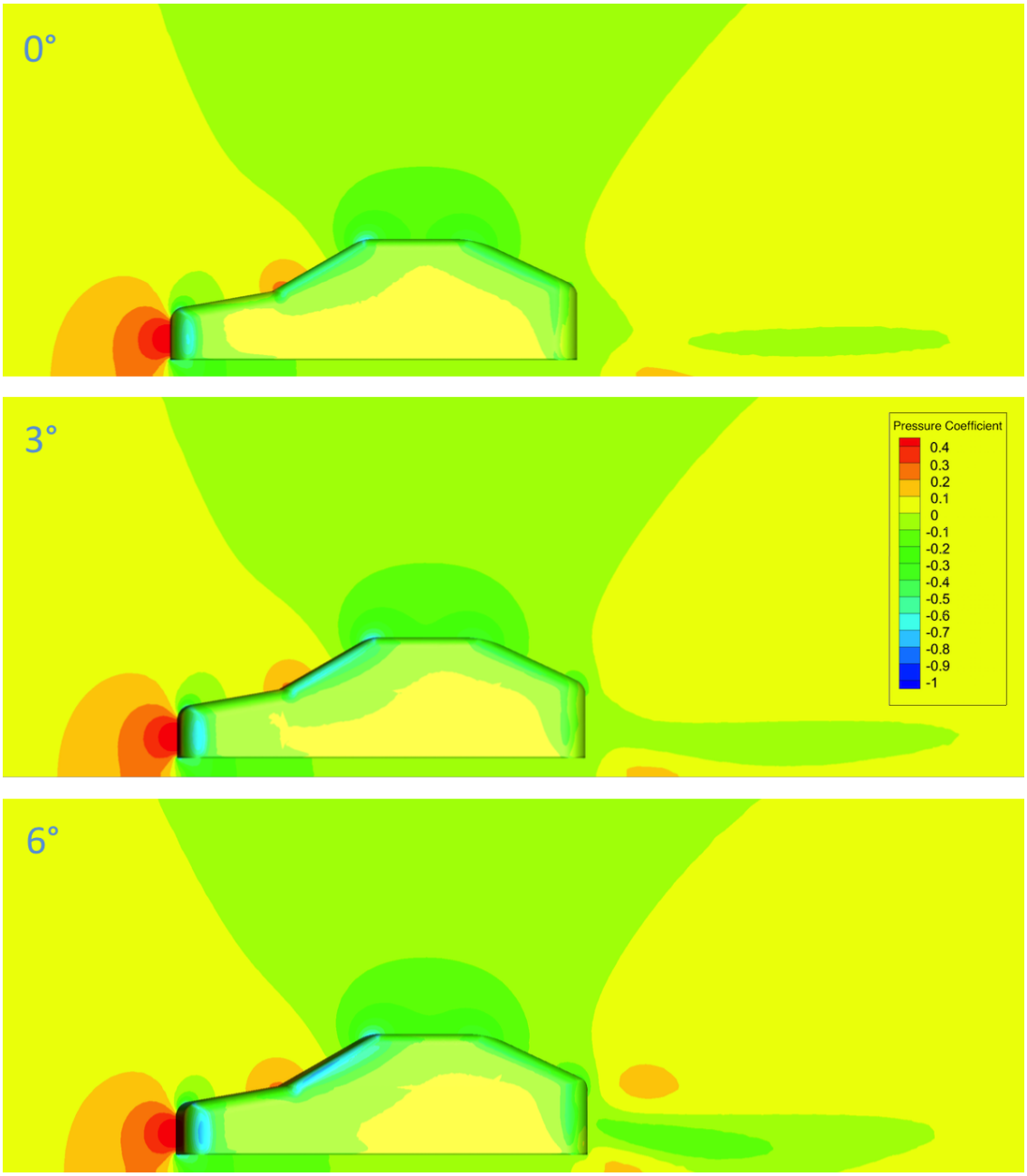

Figure 5.6: Pressure contours along the ZX - plane of the control volume

Skin friction coefficient

In addition to the difference of the pressure drag, the drag is also influenced by the vehicle's surface skin friction as was discussed in section 1.1. The surface skin friction coefficient distribution is shown in figure 5.7. In general one can state that the local shear stress component, and therefore the surface skin friction coefficient will be lower when the gradient of the local velocity near the surface wall within the boundary layer is reduced. This is typically the case when the local velocity is reduced due to the pressure distribution, or when the flow is separated from the surface due to locally high adverse pressure gradients.

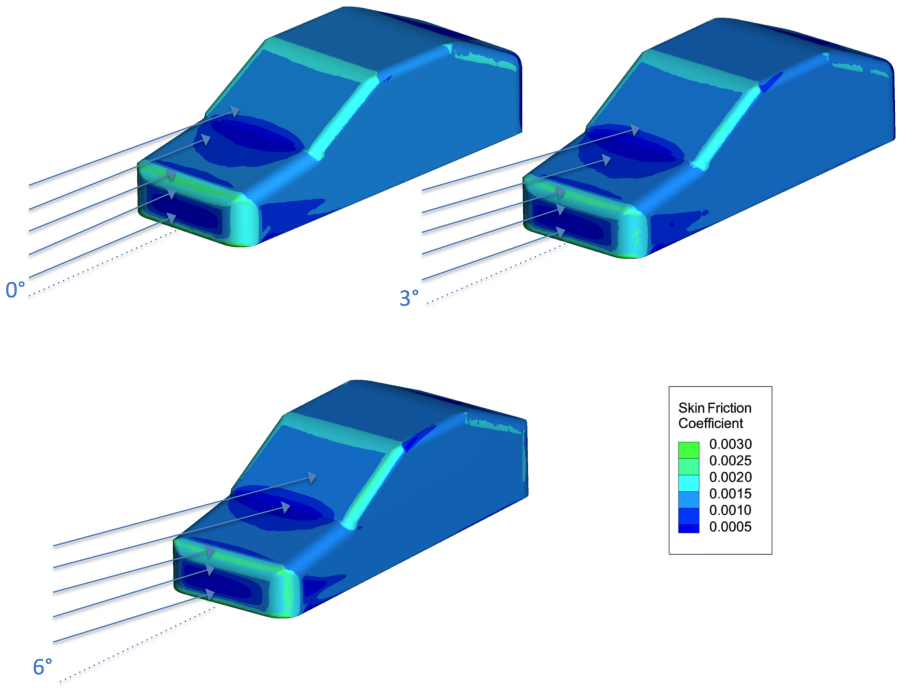

Figure 5.7: Skin friction distribution on the vehicle front during 3 different cross-wind flow angles

Within figure 5.7 it can be observed that around the contour of the nose the green zones indicate regions of high skin friction, which is due to the accelerated flow. As was expected the leeward radius towards the vehicle side experiences an increased skin friction due to the increased local flow velocity when the incident cross-wind flow angle is increased. Just after this area it appears that both on the motor compartment as well as the sides of the vehicle experience a zone of separated flow. This zone which is indicated by the dark blue areas is larger on the sides than is the case on the motor compartment. A possible explanation for this is that the angle between the frontal nose section and the motor compartment equals 100 degrees, whereas the angle between the frontal nose section and the vehicle sides is 90 degrees.

The flow is therefore likely to reattach faster on the motor compartment surface than on the vehicle sides since the curvature of the geometry is less. When the

cross-wind flow angle is increased to 6 degrees, the separated airflow on the front part of the vehicle sides change. On the windward side the skin friction increases as the separated flow zone is reduced due to the inclination towards the flow. On the leeward side however the skin friction decreases even further as the flow separates even further with the separation of flow as the vehicle side geometry is inclined further away from the incoming flow.

The pressure increase around the interface between the motor compartment and the front window results in a reduced flow velocity in this area, which results in a reduced skin friction coefficient. It can be seen in figure 5.7 that this area shifts slightly to the windward side of the vehicle when the cross-wind flow angle is increased. This can be attributed to the fact that the leeward A-pillar has a lower pressure coefficient than the windward A-pillar, with a corresponding higher velocity of the flow in this area. The higher velocity results in a higher skin friction compared to the windward side.

Additional flow effects can be observed when the flow encounters the interface between the front window and the roof. The flow is accelerated over this interface towards the roof with an accompanied skin friction increase, similar but to a less extent than the front nose section and the motor compartment. An interesting observation can be made on the leeward interface between the A-pillar and the side of the roof, where an area of reduced skin friction is found which increases with increasing cross-wind flow angle.

The skin friction aft of the vehicle where the vehicle wake is present is shown in figure 5.8. Here it can be seen that a symmetric flow condition results in a symmetrical skin friction distribution. In the center of the rear roof there is a triangular area on the surface which experiences a lower skin friction compared to the outer areas of the rear window surface. This triangular zone indicates the boundary of the vortices which originate from the C-pillars, as the rotational flow within these vortices yield a locally high skin friction coefficient due to the high local flow velocities within the vortices.

It appears that during cross-wind flow both vortices align with the incoming flow, and thereby shifting over the rear window. This is confirmed by the streamline plots shown in figure 5.5. The separated flow is unable to reattach to the adjacent surfaces, resulting in the formation of the vehicle wake which is enclosed by the C-pillar vortices.

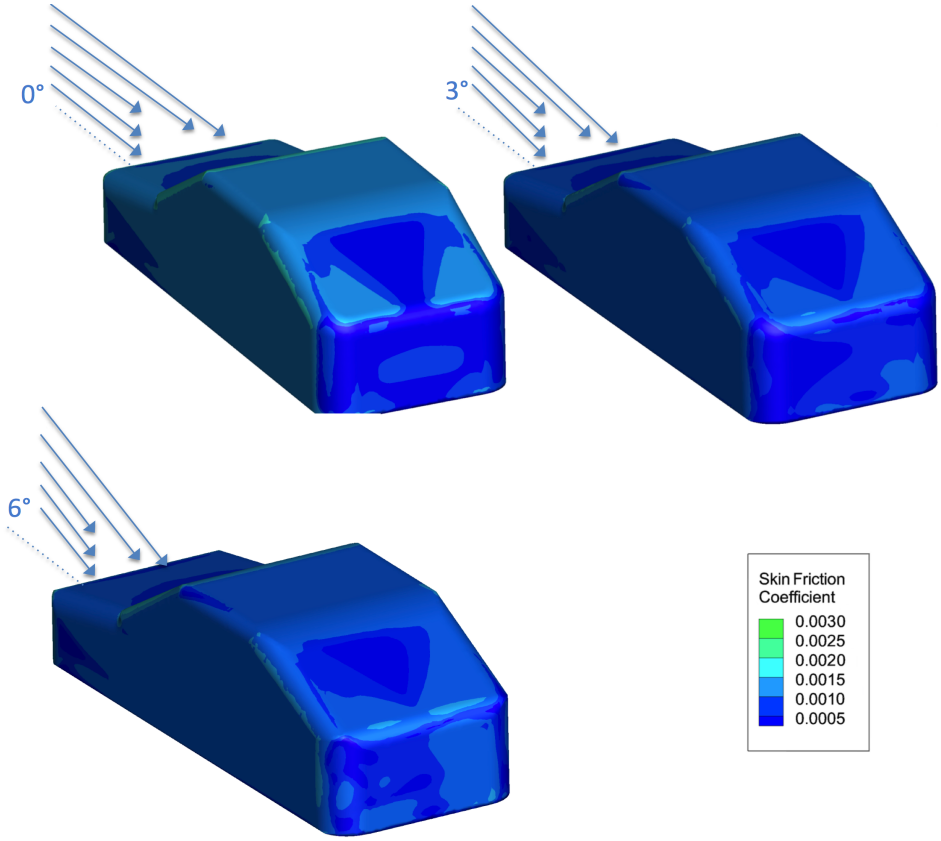

Figure 5.8: Skin friction distribution rear of the vehicle during 3 different cross-wind flow angles

The pressure distribution can be integrated over the complete vehicle in order to quantify the resulting force and moment coefficients as is shown in table 5.2:

Aerodynamic metric	0° cross-wind	3° cross-wind	6° cross-wind
C_D	0.250	0.303	0.368
C_L	0.223	0.246	0.305
C_S	0.000	-0.075	-0.164
C_{Mx}	0.000	0.005	0.010
C_{My}	0.054	0.055	0.059
C_{Mz}	0.000	0.006	0.010

Table 5.2: Aerodynamic force and moment coefficients for different cross-wind flows

Within table 5.2 it can be seen that the drag, lift and side force coefficient increases with increasing cross-wind flow. The moment coefficients also tend to increase with an increasing cross-wind flow angle. The pitching moment C_{My} does appear to be less affected by the cross-wind flow.

Vehicle dynamics results

The vehicle dynamics results for the reference vehicle use the previous aerodynamic results as input These forces and moments are incorporated within the vehicle dynamics model in order determine the system response, which in turn delivers a vehicle trajectory. The boundary conditions consists of the initial longitudinal velocity and vehicle suspension parameters have a substantial effect upon the simulation results. The effect of varying these parameters is discussed in section 5.2.

It was chosen to use two sets of reference vehicle dynamics parameters. The choice for two is because the first set contains vehicle dynamics parameters for a conventional combustion vehicle, while the latter contains vehicle dynamics parameters for a heavier electric vehicle. Here the force and moment coefficients from table 5.2 needs to be converted into a new forces and moments matrix when simulations are performed upon the conventional vehicle. This is done to compensate for the difference in center of gravity location around which these coefficients are computed.

In order to be able to compare the predominant differences equally, the only changes between these two sets involve the mass distribution, the position of the center of gravity and the corresponding mass moments of inertia around all three axes. The suspension (geometry) settings are kept fixed on both vehicle types. The results of the lateral response for the three reference vehicles is shown in figure 5.9 for a vehicle longitudinal velocity of 30 m/s. Here the results are two-fold; for every cross-wind flow angle both a conventional combustion engined vehicle (red) and an electric vehicle (green) are simulated.

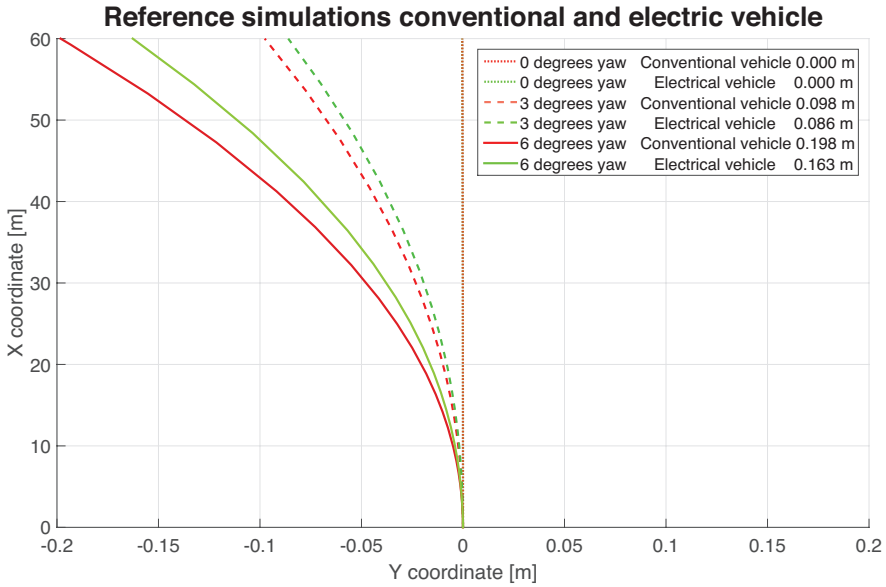

Figure 5.9: Lateral displacement of electric and conventional vehicles moving at 30m/s during 0, 3 and 6 degrees of cross-wind flow

Within figure 5.9 the effects of both vthe varying cross-wind flow (indicated by solid, dashed and dotted trajectories) and the difference between the lateral dynamics

between a conventional and electric vehicle are depicted. When the cross-wind angle is zero and the flow conditions are symmetrical, both the electric vehicle and the conventional internal combustion engined vehicle (ICE) do not translate in the lateral direction as expected. If the incident cross-wind flow is increased to 3 degrees the vehicles deviate approximately 0.086 to 0.098 m from their original course. When the cross-wind flow angle is increased towards 6 degrees both vehicles the lateral displacement becomes around 0.163 to 0.198 m in the lateral direction. It can be concluded that the difference between the two vehicles becomes more pronounced when the cross-wind flow angle is enhanced.

Since the aerodynamic loading is the same for the two vehicle types, the difference is due to the vehicle weight distribution and suspension parameters. More information about the difference between for both vehicles and the effects of the vehicle weight distribution and suspension parameters can be found in section 5.2. The lateral displacement is the main metric for cross-wind flow performance, which is composed out of (among others) the dynamic events as shown in figure 5.10.

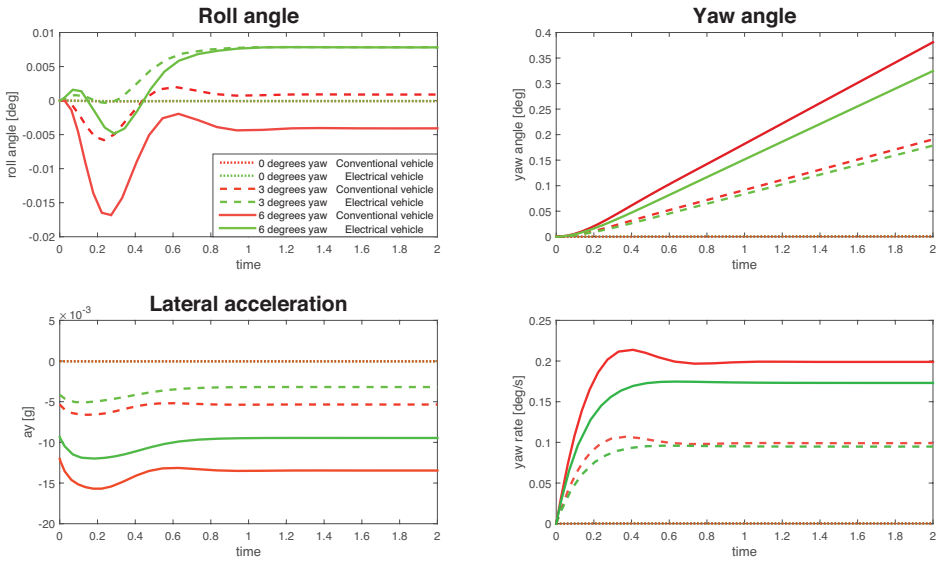

Figure 5.10: Vehicle dynamics log of three reference vehicles moving at 30m/s

The roll angle history file which is as depicted on the top left in figure 5.10 shows an interesting event. It appears that due to the yaw rate causes the vehicle nose to rotate in the positive yaw direction, which results in a centripetal force which depends upon the radius of rotation. Since the side force acts in the opposite direction, and the vehicle has a roll stiffness and roll damping, the vehicle shows an oscillatory behavior.

Because there is a substantial difference in different vehicle dynamics parameters it is hard to distinguish which effect is due to which property. All angles and accelerations are relatively small due to the small incident cross-wind flows and the relatively high longitudinal velocity. The lateral acceleration is nonzero at $t = 0s$

due to the abrupt on / off behaviour of the cross-wind flow at $t = 0s$. This is because the yaw acceleration is positive until approximately $t = 0.4s$, and equal to zero beyond $0.4s$.

It was found that the difference between the heading angle and the vehicle yaw angle is negligible, since the body slip is negligible. The yaw angle therefore also reflects the heading angle of the vehicle.

In order to check that the order of magnitude of the presented vehicle dynamics metrics are in place, the results have been compared to a similar simulation setup within the vehicle dynamics software package CarSim. This extensive vehicle dynamics software is capable of simulating detailed suspension and vehicle designs. This software uses a predefined (linear) lookup on how the different force and moment coefficients change due to an incident cross-wind flow. Since the software license for this product was not available for further analysis, only a comparison run to compare with the MATLAB model. During this comparison it was found that the input force and moment coefficients are similar for the reference vehicle database that this commercial software uses. It was also found that the lateral acceleration, the yaw angle, the roll angle and the lateral displacement are all in the same order of magnitude compared to CarSim's results.

With this additional check the confidence in the simulation results was secured, allowing the results presented in this subsection to serve as baseline results. These baseline results can be used in order to compare towards the subsequent lateral dynamic performance results of the vehicles which have a modified geometry.

These vehicles which have a modified geometry are discussed individually per type of shape modification, i.e. arrowing the front of the vehicle, or tapering the aft of the vehicle. The respective results are presented in the next subsections, and compared towards the baseline results from this section. This comparison is done by means of overlay plots and performance plots where the change in performance of the drag coefficient is compared with the change in performance of the lateral displacement.

Before the geometry is changed with systematic modifications, vehicle dynamics sensitivity study is performed first. This allows for insight on which forces, moments and vehicle dynamics parameters are of importance for the lateral dynamic response of the vehicle. This information can be used in order to focus on the most significant parameters without losing track of the cause-effect relations in analysing a vehicles lateral response.

◇

5.2 Vehicle dynamics sensitivity study

Within this section a vehicle dynamics sensitivity study is performed in order to identify important parameters for the lateral dynamic response of a vehicle which is subject to cross-wind flows. The following parameters are studied to reveal the effect on the lateral dynamics response upon an electric reference vehicle:

- Aerodynamic force and moment coefficients
- Operating weight of the vehicle
- Position of the center of gravity
- Mass moments of inertia
- Roll stiffness and damping
- Longitudinal velocity of the vehicle
- Comparison with a steering wheel input

In section 5.1 a combination of these effects (except the aerodynamic forces and moments as these are unchanged) was shown by comparing a conventional vehicle with an electric vehicle. Here it became apparent that the combined effect of the above mentioned parameters causes the lateral deviations of over 20% for cross-wind flows of 6 degrees. In order to study which vehicle dynamic effect has what effect, the vehicle dynamics parameters are studied systematically.

Aerodynamic force and moment coefficients effects

First the aerodynamic force and moment coefficients will be assessed. An effective way of doing this is by manually modifying individual force and moment coefficients to zero instead of their actual value. Although all force and moment coefficients are necessary to describe the attitude of the vehicle, not all values contribute to the lateral dynamic response during the aerodynamic loading within this study, i.e. there is a 0% difference in lateral position after 2 seconds. It was found that these examples include the C_D, C_L, C_{Mx} and C_{My}. The most important force and moment coefficient turn out to be C_S and C_{Mz} as shown in figure 5.11 and 5.12.

Within figure 5.11 the difference in the lateral dynamic response is shown between the reference and zero side force coefficient C_S simulations.
This can be seen when the red and the blue lines are compared to one another. Here the solid lines represent the 6 degrees cross-wind flow, dashed lines represent the 3 degrees and ultimately the dotted lines show the 0 degree cross-wind flow.
Analogous to figure 5.11 the moment coefficient around the Z axis C_{Mz} can be set to zero as well as is depicted in figure 5.12.

It appears that when the moment coefficient C_{Mz} is set to zero the effect is more substantial than the side force coefficient C_S. This conclusion is based upon the larger discrepancy found between both the two solid and dashed lines.
Nevertheless the C_{Mz} and C_S are both important and prove to be the most important metrics to study when systematic shape modifications are applied.

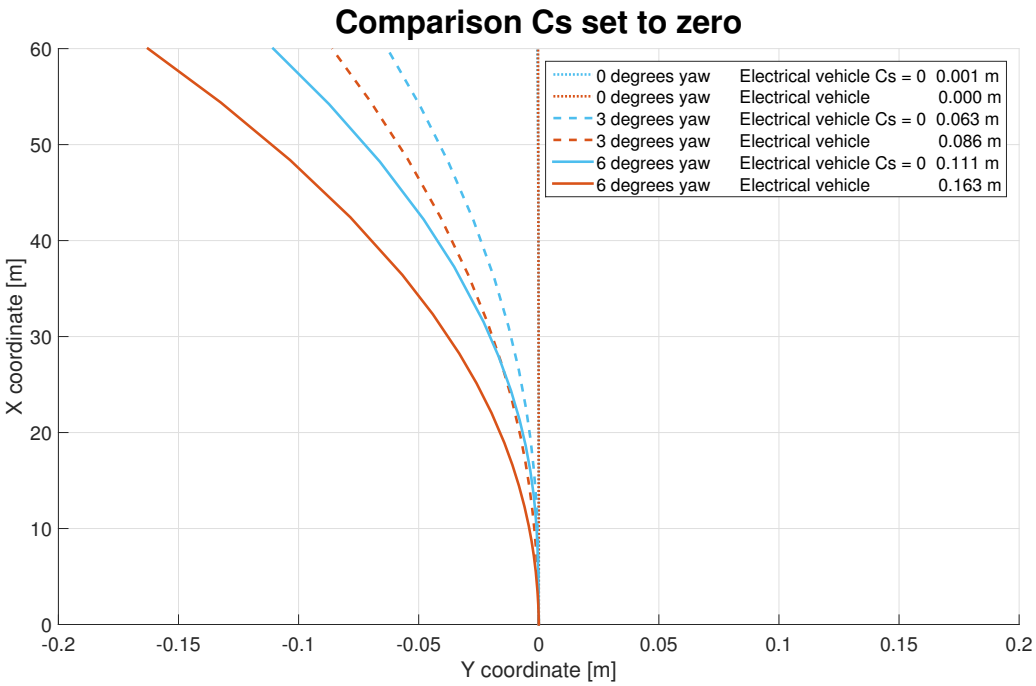

Figure 5.11: Discrepancy in trajectories between reference and C_S set to zero

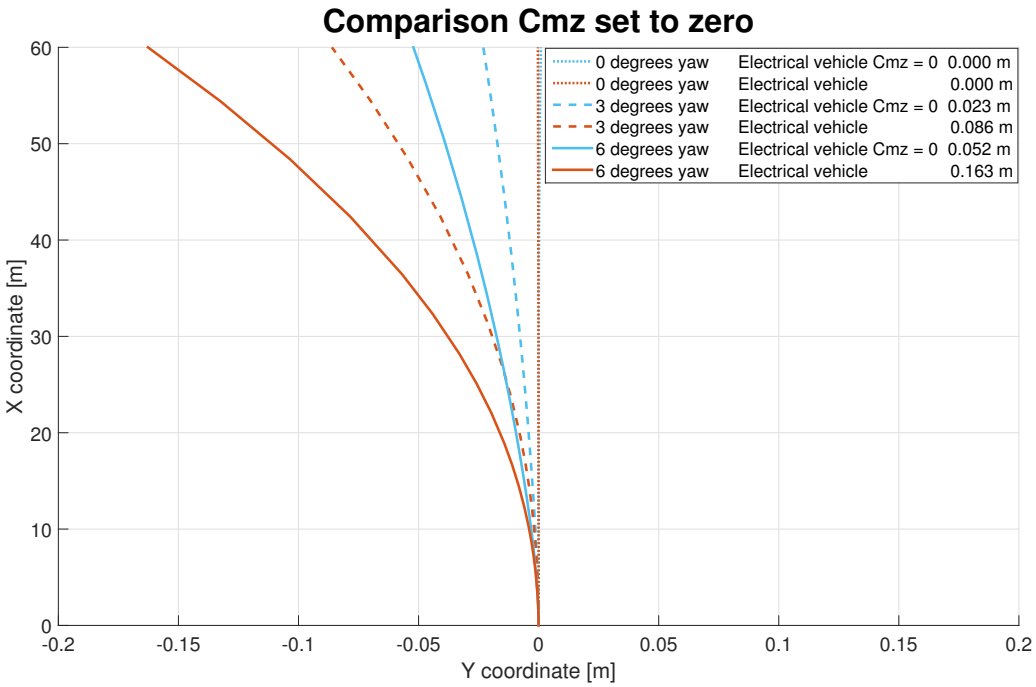

Figure 5.12: Discrepancy in trajectories between reference and C_{Mz} set to zero

Operating weight of the vehicle effects

The next vehicle dynamics metric to investigate is the vehicle operating weight. The difference in weight is applied at the vehicle center of gravity location, which has effects on both the mass moments of inertia and the friction forces. The friction force between the tires and the ground depends linearly on the friction coefficient μ and the normal force at each wheel F_{Zi}, where i = 1,2,3,4 as depicted in figure 4.4. Here it holds that a heavier vehicle both has an increased mass moment of inertia in combination with enhanced friction forces at the wheels, typically resulting in a reduced lateral dynamic response. Due to the fact that the lateral dynamic excitations are small within this study a slight change in weight does not change much. Therefore both the increments and decrements of the vehicle weight are set to 50%, which allows for insights in the trends of the vehicle operating weight. The results are shown in figure 5.13, where it can be seen that indeed lighter vehicles obtain a larger lateral deviation than heavier vehicles.

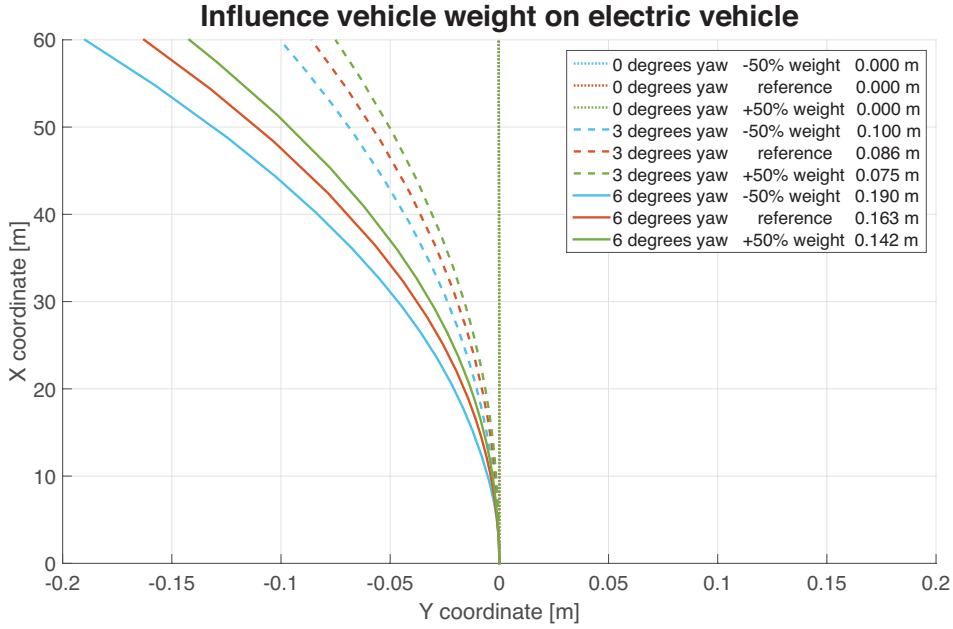

Figure 5.13: Electric vehicle trajectories where the vehicle weight is reduced and enhanced by 50%

It can be concluded that the vehicle operating weight is of importance for the lateral dynamic response of vehicles during cross-wind flows. It appears that the result is intuitive and predictable within this study. Here it certainly does matter where the additional weight is located. For this reason an additional subsection is devoted to documenting the effect of the position of the vehicle center of gravity.

Position of the center of gravity

The effect of the center of gravity position (COG) was studied by systematically changing the position of the vehicle COG. Here the vehicle COG is also used within the computation of the aerodynamic forces and moments which are thereby affected as well. It was found that the y and z position of the center of gravity do not have any effect on the lateral deviation of the vehicle because the secondary nature effects (e.g. roll, pitch, compliances and coupled dynamics) are neglected. The longitudinal position of the COG however causes a substantial difference in the lateral deviation of the vehicle. The longitudinal position of the COG is the distance between aft of the vehicle and the vehicle COG. This distance is $1.884m$ for the electric vehicle, and $2.150m$ for the conventional combustion vehicle. These values are first modified by adding and subtracting 10% of this value, where the results are shown in figure 5.14 for electric vehicles only as the results between the two vehicles is similar:

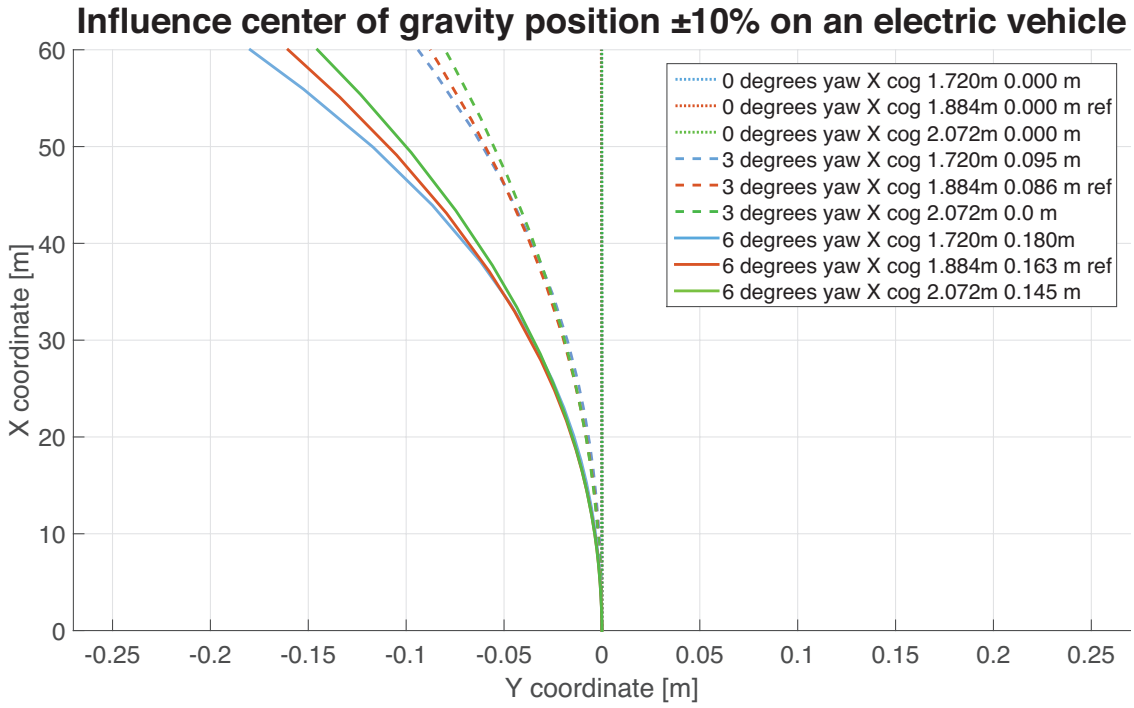

Figure 5.14: Electric vehicle trajectories where the longitudinal position of the center of gravity is reduced and enhanced by 10%

Within figure 5.14 it can be seen that during 3 degrees cross wind flows a decrement in the longitudinal position of the COG results in a 10% increment in deviation. During this cross wind condition an increase in COG results in a reduced lateral deviation, mainly due to the reduced moment arm on which the side force coefficient contributes to the yaw moment coefficient C_{Mz}. When the center of gravity position is enhanced and reduced even further to plus or minus 20% the effects are magnified as is shown in figure 5.15.

Within figure 5.15 it can be seen that in the scenario where the center of gravity location is translated by plus or minus 20 % the results are substantial, yielding up to 22% more lateral displacement when the center of gravity is located $0.4m$ more to the aft of the vehicle.

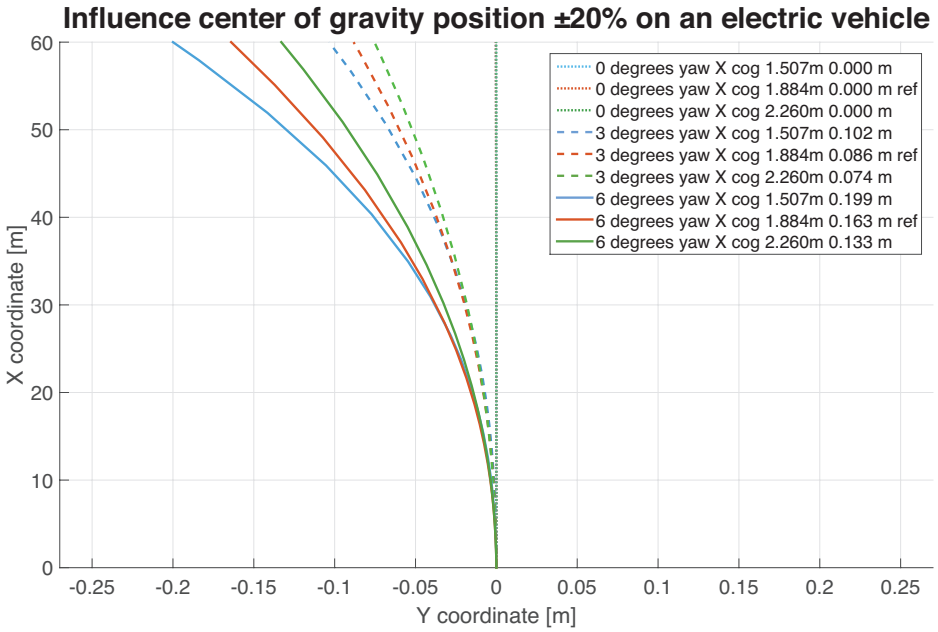

Figure 5.15: Electric vehicle trajectories where the longitudinal position of the center of gravity is reduced and enhanced by 20%

It can be concluded that the location of the center of gravity on the longitudinal axis has a profound effect upon the lateral displacement. The effects appear to be intuitive, i.e. a reduced distance from the vehicle aft to the center of gravity result in an enhanced lateral deviation, where an increased distance reduces the lateral deviation.

Longitudinal velocity of the vehicle

All simulations have so far been carried out at a fixed longitudinal velocity of $30m/s$, or roughly $108km/h$ as a baseline cruise velocity. In order to study the effect of this longitudinal velocity, 3 additional velocities have been simulated as well. These additional velocities include $20m/s$, $40m/s$ and $50m/s$. It was chosen to keep the cross-wind velocity of $3.15m/s$ (6 degrees cross-wind flow during $30m/s$) and 1.58 m/s (3 degrees cross-wind flow during $30m/s$)fixed rather than simulating 3 and 6 degrees of cross-wind. The traditional cross-wind flow angles are therefore linearly dependent upon of the longitudinal velocity as is depicted within table 5.3:

Longitudinal velocity [m/s] - (km/u)	**Cross-wind angle with 3.15 m/s cross wind**	**Cross-wind angle with 1.58 m/s cross wind**
20 - (72)	8.95°	4.48°
30 - (108)	6.00°	3.00°
40 - (144)	4.50°	2.25°
50 - (180)	3.60°	1.80°

Table 5.3: When the cross-wind velocity is kept fixed, the incident cross-wind flow angle changes with longitudinal velocity

Additional CFD simulations have been performed with these additional cross-wind flow angles, where the effect upon the reference vehicles is shown in figure 5.16 for electric vehicles and 5.17 for conventional vehicles.

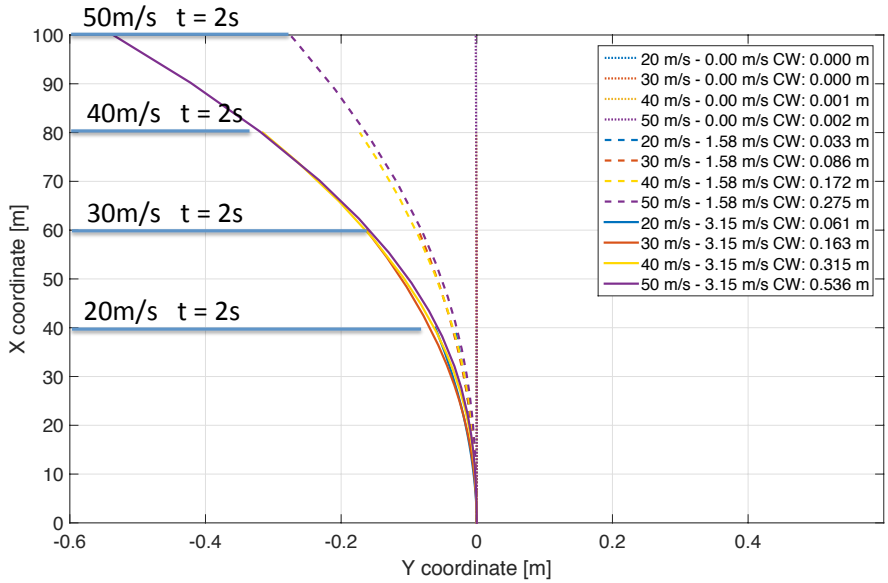

Figure 5.16: Electric vehicle trajectories with different longitudinal velocities - 1.58 and 3.15m/s cross-wind

It can be seen from figure 5.16 an increased longitudinal velocity does not have a substantial effect on the lateral deviation of the electric vehicle, other than that the vehicle covers more distance.

In contrast to the electric vehicle, the conventional vehicle obtains a smaller lateral deviation when the longitudinal velocity is increased as shown in figure 5.17:

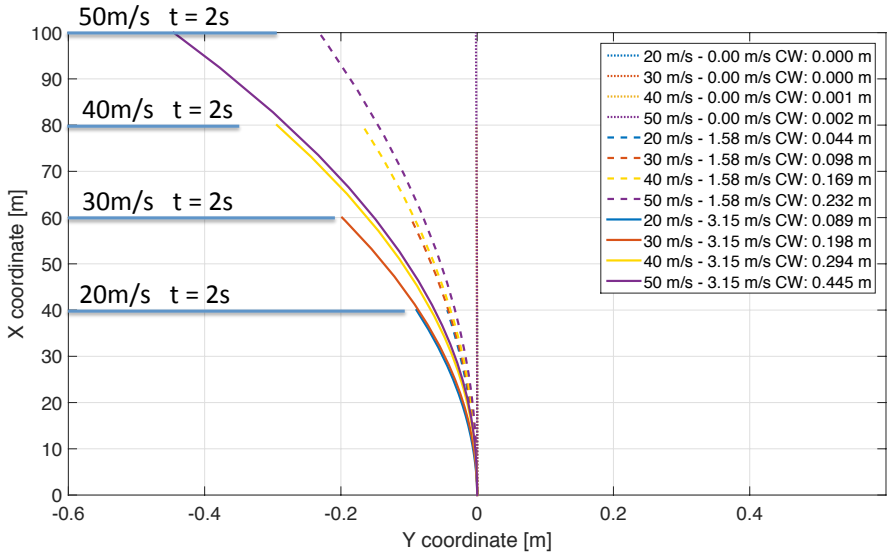

Figure 5.17: Conventional vehicle trajectories with different longitudinal velocities - 1.58 and 3.15m/s cross-wind

During both 40 and 50m/s simulations the conventional vehicle actually has a lower lateral deviation than the electric vehicle. When the velocity is set at 20 and 30 m/s the electric vehicle deviates less than the conventional vehicle. Since the aerodynamic loading is identical between the two vehicles, this difference is solely due to the combined differences in weight, weight distribution and the corresponding mass moments of inertia.

This is an important observation that in regards to the results found in the previous section, where where the electric vehicles were found to have a reduced lateral deviation compared to conventional vehicles.

Mass moments of inertia

In order to study the effect of the different mass moments of inertia I_{xx}, I_{yy} and I_{zz}, each respective metric has been multiplied with a factor of 0.5 and 1.5. It was found that both this increment and decrement effect again did not affect the lateral displacement during the I_{xx} and I_{yy} simulations because the secondary nature effects (e.g. roll, pitch, compliances and coupled dynamics) are neglected. The mass moment of inertia around the Z-axis I_{zz} however did show a difference as can be seen in figure 5.18. The reason for this is that the I_{xx} mostly influences the rolling behavior of the vehicle, where it was already shown that rolling has a negligible effect on the lateral deviation. Analogous to I_{xx}, the I_{yy} does not affect the lateral dynamics either due to the fact that pitch dynamics are not included within this study.

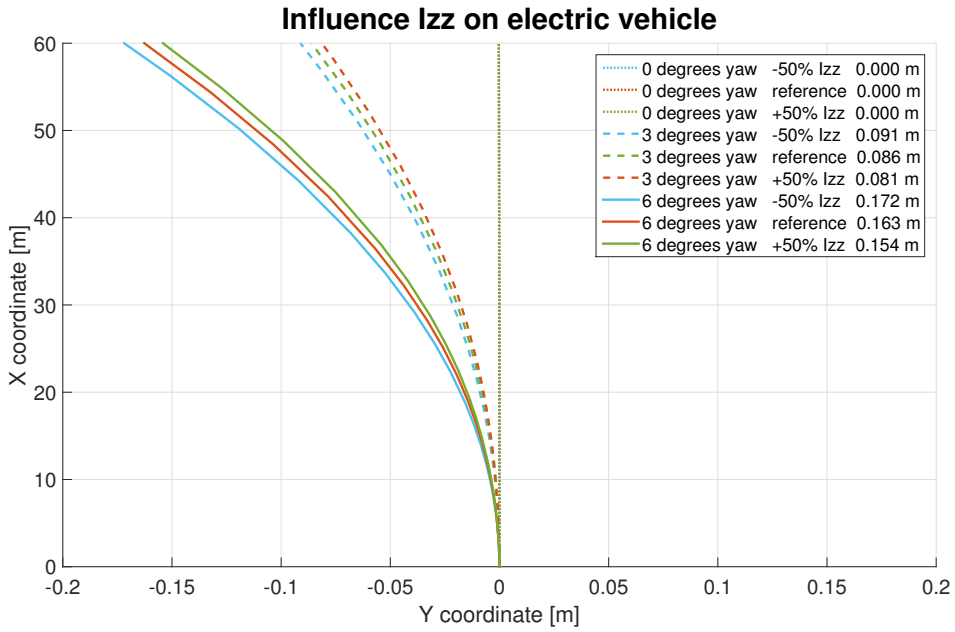

Figure 5.18: Izz trajectories

Since the yaw acceleration $\ddot{\psi}$ is linearly dependent on I_{zz}, the yaw acceleration is enhanced when the I_{zz} is reduced. This results in a larger lateral deviation which is also observed in figure 5.18. The opposite holds as well; an enhanced I_{zz} results in a lower yaw acceleration $\ddot{\psi}$ resulting in a reduced lateral deviation.

Roll stiffness and damping

The roll stiffness and damping effect were studied using the same method as as done during the mass moment of inertia study. Here it was found that both the roll stiffness and the damping do not influence the lateral deviation. This is mostly due to the fact that only the rolling behavior of the vehicle is influenced, which does not affect the lateral deviation.

Comparison with a steering wheel input

It follows that during the maximum lateral deviation due to a cross-wind angle of 6 degrees results within this study in a lateral deviation in the order of $0.20m$. When this value of this lateral deviation is compared with the effect of a steering input it one can put the aerodynamic loading in perspective. It was found that if the steering wheel (of a Mercedes car) is rotated towards at 1 degrees in either clockwise or counterclockwise direction for 2 seconds, a similar lateral deviation is obtained. A steering angle of 1 degree is easily achieved during normal driving situations. It can therefore be concluded that during normal cruise conditions where the vehicle is driving with around $30m/s$ while encountering cross-wind flows of up to 6 degrees, the lateral deviation is typically does not cause an issue. Although the lateral deviations are small it is chosen to include these within the study, since it is an inherent design implication which cannot be influenced by the operator.

Conclusions on vehicle dynamics variations

The main conclusions from the studied vehicle dynamics study are itemized below:

- From the aerodynamic quantities the side force coefficient C_S and C_{Mz} are by far the most dominant parameters for the lateral deviation.
- A 50% lighter vehicle deviates around 16% more, where 50% heavier vehicle deviates around 15% less than the reference vehicle.
- The longitudinal location of the center of gravity is important. For electric vehicles a $0.4m$ more aft positioned COG results in 22% more lateral deviation.
- When the vehicle velocity is modified it was concluded that electric vehicles are continue to travel the original trajectory, where the velocity determines the covered distance. Conventional vehicles however tend to deviate relatively less when the velocity is enhanced. Up until a longitudinal velocity of 30 m/s electric vehicles deviate less than conventional vehicles. When the velocity is enhanced the opposite is true, where conventional vehicles with a more forward placed COG deviate around 17% less.
- The mass moments of inertia I_{XX} and I_{YY} do not contribute to the lateral deviation when cross-wind flows of up to 6 degrees are considered. The I_{ZZ} does play a role since the yaw acceleration metric is linearly dependant upon the I_{ZZ}.
- A steering wheel input angle of 1 degree yields similar lateral deviations as a 6 degrees cross-wind flow.

These conclusions should be kept in mind when viewing the results of the different shape modifications sections. The results found in these subsequent sections are all subject to change when one of the above mentioned vehicle dynamics metrics are modified.

$\diamond$

5.3 Arrowing the vehicle front end

The first geometry modification that is applied is arrowing the front of the vehicle. This arrowing modification is systematically performed using 4 intermediate angles, where 0, 5, and 10 and 15 degrees of arrowing angle are applied. The arrowing modification is depicted within figure 5.19:

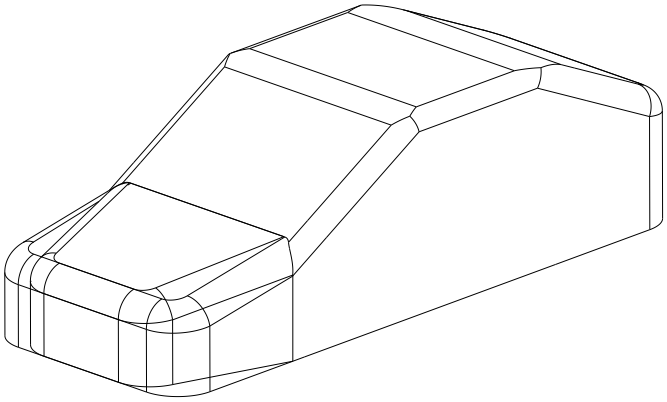

Figure 5.19: Arrowing modification performed on the vehicle front end

Aerodynamic implications of arrowing the vehicle's front end

The arrowing modification of the vehicle body especially affects the flow on the vehicle front. The vertical frontal nose section area is reduced which leads to a smaller high pressure zone at the front of the vehicle. The angle between the nose section area and both the front left and right side panel (near the left front "wheel" area) is reduced from 90 degrees to 85, 80 or 75 degrees. The results from the aerodynamic simulations for different arrowing angles during zero degrees cross-wind flow is shown in table 5.4:

Aerodynamic metric	0° arrow	5° arrow	10° arrow	15° arrow
C_D	0.251	0.239	0.235	0.224
C_L	0.224	0.224	0.235	0.236
C_S	0.000	0.000	0.000	0.004
C_{Mx}	0.000	0.000	0.000	0.000
C_{My}	0.054	0.053	0.051	0.049
C_{Mz}	0.000	0.000	0.000	0.000

Table 5.4: Aerodynamic metrics for different arrow angles - 0° cross-wind flow

It follows that during 0 degrees cross-wind flow the drag coefficient is reduced by up to 27 drag counts when a 15 degrees arrowing modification is employed. The lift coefficient on the other hand tends to increase by 12 counts. The arrowing modification performed by Toppinga on the SAE station wagon also showed a decrement in drag coefficient and an increase in the lift coefficient. [55] The differences Toppinga found are to a smaller extent than was found here - up to 5 drag counts.

This difference could be due to the difference in the applied arrowing; Toppinga arrowed the front 300 mm of the vehicle, whereas within this study the full 1000 mm front section was arrowed. Furthermore the difference between fastback vehicles and station wagons is not taken into account.

In the event of an incident cross-wind flow the leeward side experiences a slightly less severe separated flow zone due to the reduced curvature of the geometry resulting in an expected lower drag coefficient contribution compared to the reference vehicle. The windward side however is inclined more towards the incident cross-wind flow, resulting in an expected increase in the local pressure coefficient.

Aerodynamic metric	**0° arrow**	**5° arrow**	**10° arrow**	**15° arrow**
C_D	0.368	0.388	0.399	0.403
C_L	0.305	0.291	0.312	0.338
C_S	0.164	0.156	0.197	0.218
C_{Mx}	0.010	0.010	0.011	0.011
C_{My}	0.059	0.059	0.059	0.057
C_{Mz}	0.010	0.011	0.008	0.007

Table 5.5: Aerodynamic metrics for different arrow angles - 6° cross-wind flow

From table 5.5 it follows that the drag, lift and side force coefficient decreases for 5 degrees of arrowing, but increases when the arrowing angle is enhanced further. Furthermore C_{Mx} and C_{My} remain fairly constant, but C_{Mz} appears to be slightly decrease due to the arrowing modification. This is beneficial for reducing the lateral deviation as is shown in the next subsection.

Within figure 5.20 an example is shown of how the pressure distribution is affected by the arrowing angle when a cross-wind flow angle of 6 degrees is encountered. It can be seen that for this cross-wind flow angle the pressure distribution in front of the vehicle is affected more than aft of the vehicle. The low pressure zone on the leeward wind side of the vehicle nose section indeed appears to decrease in magnitude due to the reduced curvature. The typical pressure increase at the hood - front window interface appears to become smaller with increasing arrowing angle, where the 5 degree arrowing geometry shows an exception.

Vehicles with an arrowing angle of 10 and 15 degrees appear to have a relatively higher pressure zone formed on the leeward front side of the vehicle, indicated by the small light-green areas where the front left wheel would be. This surface pressure within this zone appears to become less negative when the arrowing angle is increased, and can be explained by the fact that this surface of the vehicle becomes more inclined to the flow hence achieve a higher local pressure.

This increment in surface pressure is most responsible for the decrement in the yaw moment coefficient C_{Mz}, mostly due to the effective moment arm towards the vehicle center of gravity.

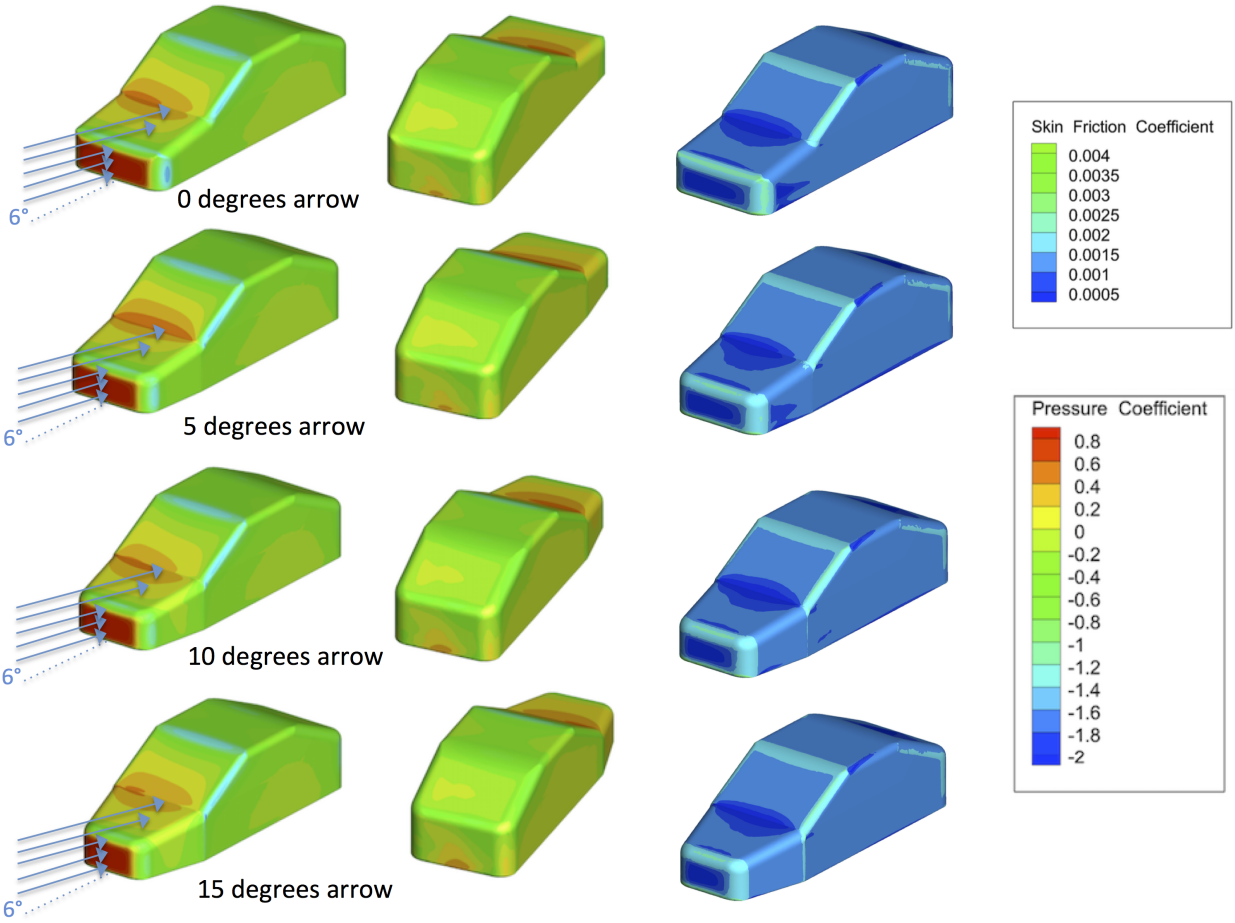

Figure 5.20: Surface pressure (left, center) and skin friction (right) distribution plots of 4 different arrowing configurations during 6° cross-wind flow

The skin friction coefficient distribution confirms the presence of a separated flow zone on the leeward front side of the vehicle, which decreases in size when the arrowing angle is enhanced as is shown in figure 5.20. Using these figures it follows that the skin friction distribution aft of the vehicle is similar between the different configurations, indicating that the difference in C_{Mz} is due to the difference in the pressure distribution on the leeward front of the vehicle.

An other interesting observation is the interface between the engine compartment surface, the front window, and the leeward vehicle side. On this location different surfaces meet, each with a distinct edge radius which inevitably don't blend particularly well. The arrowing modification tends to induce a complex flow structure at this junction.

In order to study the effects of the combined slightly reduced C_{Mz} and enhanced C_S the aerodynamic loading is employed on both the electric and the conventional vehicle within the next subsection. Here the consequences on the vehicle dynamics due to the arrowing modification results are presented.

Vehicle dynamics results

The dynamic lateral response of the reference vehicle with arrowing modifications is presented using vehicle trajectories within figure 5.21 and 5.22:

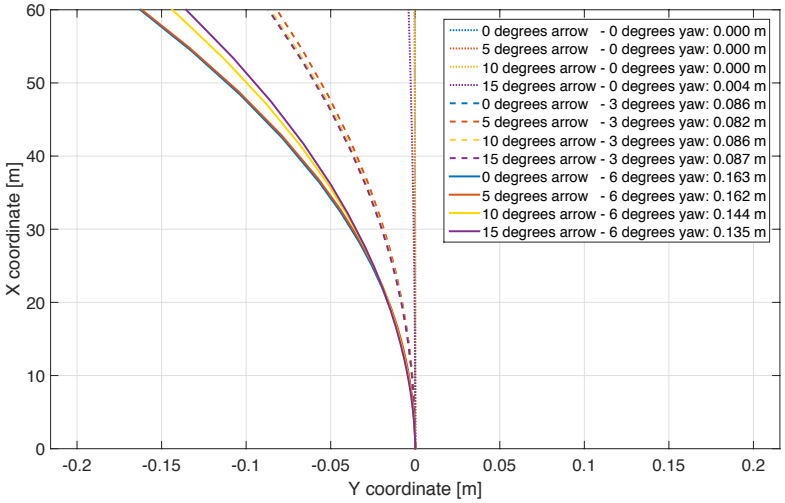

Figure 5.21: Electric vehicle trajectories with arrowing during 0°, 3° and 6° cross-wind

It can be seen in figure 5.21 that there is a difference between the effectiveness of arrowing between the trajectories of electric vehicle during 3 and 6 degrees cross wind flow. During 6 degrees cross-wind flow the arrowing modification is more effective than during 3 degrees cross-wind flow. Another observation is that arrowing can reduce the lateral deviation by around 20% during 6 degrees cross-wind flows.

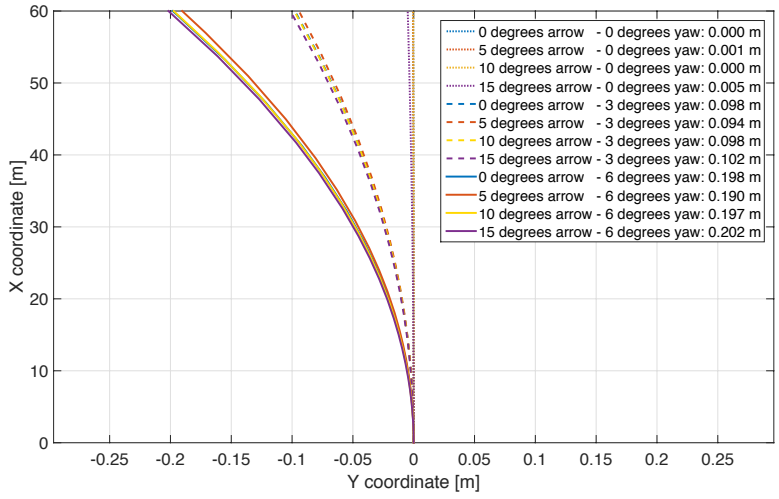

Figure 5.22: Conventional vehicle trajectories with arrowing during 0°, 3° and 6° cross-wind

Within figure 5.22 it is shown that the difference in lateral deviation is reduced between the 4 different conventional vehicle configurations. Arrowing appears to have a negligible effect on the lateral deviation for conventional cars.

The effect of arrowing the front of vehicle differs per incident cross-wind flow angle. When the different arrowing effects of the three different cross-wind flow angles are combined, information can be obtained about the averaged effect of arrowing.
The averaged data can provide insight in different performance metrics relations. An interesting way of presenting important relations is shown in figure 5.23. Within this figure it can be seen that arrowing the vehicle is on average beneficial for reducing the drag coefficient, regardless if the vehicle is conventional or electric.

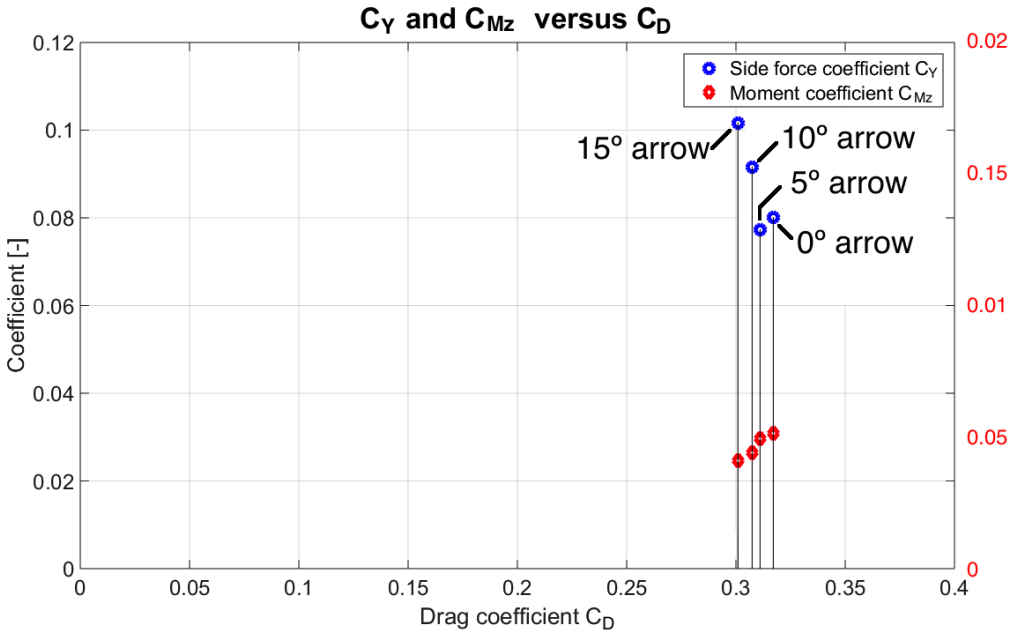

Figure 5.23: Averaged (0°, 3° and 6° cross-wind) yaw moment - and side force coefficient versus averaged drag coefficient

Furthermore it can be seen that arrowing electric vehicles tends to slightly decrease the yaw moment coefficient C_{Mz}, which reduces the lateral displacement.
In addition it can be seen that the side force C_S on average slightly decreases for 5 degrees of arrowing, but again increases for 10 and 15 degrees of arrowing. This implies that as far as the drag coefficient is concerned, from these options the 15 degrees arrowing angle is most beneficial.

Within figure 5.24 and 5.25 the gains and losses in percentages are shown for both the drag coefficient and the lateral displacement for both vehicle types. Here it holds that the top - left corner is the most ideal situation, where both a reduction in drag coefficient as well as lateral deviation is obtained.

It can be concluded that for electric vehicles any arrowing angle is beneficial for reducing both the vehicle drag and the lateral displacement. It follows that a 15 degrees arrowing angle however the optimal angle for electric vehicles, as this angle results in the highest reduction in lateral deviation and drag coefficient.

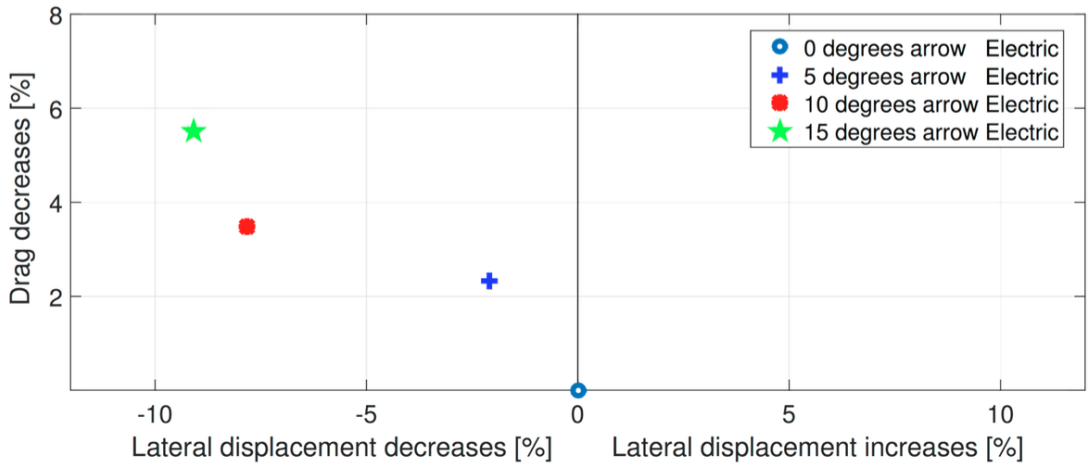

Figure 5.24: Arrowing has a positive effect on the drag coefficient and lateral displacement for electric cars

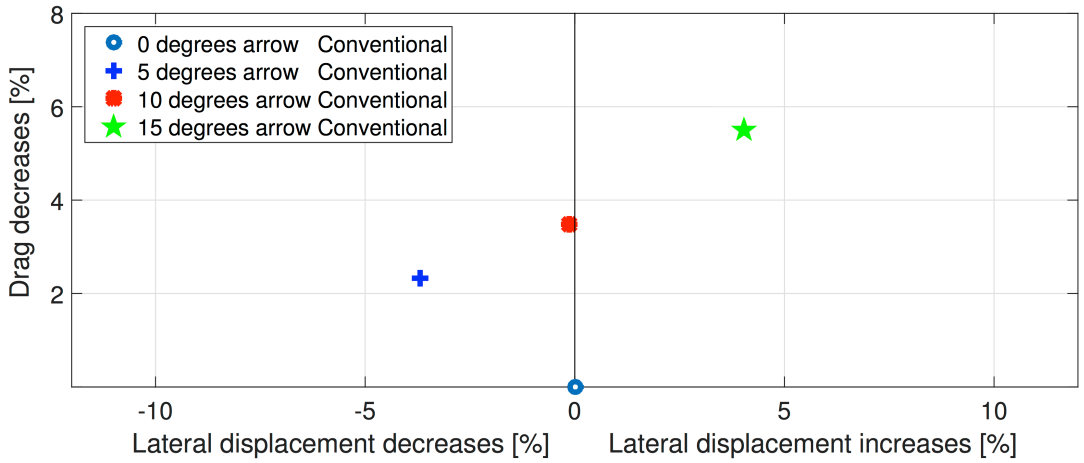

Figure 5.25: Arrowing has a positive effect on the drag coefficient, and combined effect on the lateral displacement for conventional cars

As was found earlier, conventional vehicles obtain less gains in terms of lateral deviation due to an arrowing angle. Especially a 15 degrees arrowing angle on average increases the lateral deviation by around 4%.

Ultimately the optimal value for the arrowing angle depends upon the vehicle type and the chosen weight factors for both the drag and the displacement metric.

◇

5.4 Tapering of the vehicle rear end

In this section the rear end of the vehicle is tapered as is shown in figure 5.26. This modification to the reference vehicle will affect both the wake and the flow around the sides and aft of the vehicle. The extend in which this happens and its effect upon the vehicle dynamics of the vehicle will be discussed.

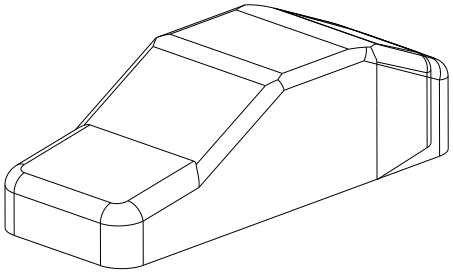

Figure 5.26: Tapering modification performed on the vehicle rear end

Aerodynamic implications of tapering the vehicle's rear end

As can be seen from figure 5.26 the vehicle body now has two inclined surfaces on each side, and a reduced aft surface area. From literature it was found that vehicles with a taper angle modification has the potential for effectively reducing the drag coefficient, typically depending upon the vehicle type. [55] The decrement in both the drag and lift coefficient would stem from the combination of the effects in the wake drag and the additional induced pressure drag at the tapered surfaces. Toppinga showed that the drag coefficient usually grows due to the drag contribution of the inclined tapered surfaces, but also decreases due to the reduced magnitude of the wake aft of the vehicle.

Depending upon the vehicle geometry either of these phenomena is predominant, resulting in either the increase or decrease in drag coefficient. The surface pressure distributions for a zero yaw cross-wind flow are first presented in order to investigate this conclusion upon the simplified vehicle geometry. The force and moment coefficients for different tapering angles is presented within table 5.6 for 0 degrees, and in table 5.7 for 6 degrees.

Aerodynamic metric	0° taper	5° taper	10° taper	15° taper
C_D	0.251	0.274	0.276	0.233
C_L	0.224	0.258	0.224	0.127
C_S	0.000	0.007	0.002	0.001
C_{Mx}	0.000	0.000	0.000	0.000
C_{My}	0.054	0.056	0.053	0.049
C_{Mz}	0.000	0.000	0.000	0.000

Table 5.6: Aerodynamic metrics for different taper angles - 0° cross-wind flow

It can be seen from table 5.6 that the drag coefficient for a symmetrical zero cross-wind flow simulation first increases for tapering angles of 5 and 10 degrees, and

then decreases for 15 degrees of tapering angle. When the corresponding pressure coefficient distribution is examined which is shown in figure 5.27 it exposes that the aforementioned effect recurs at the vehicle geometry of this study.

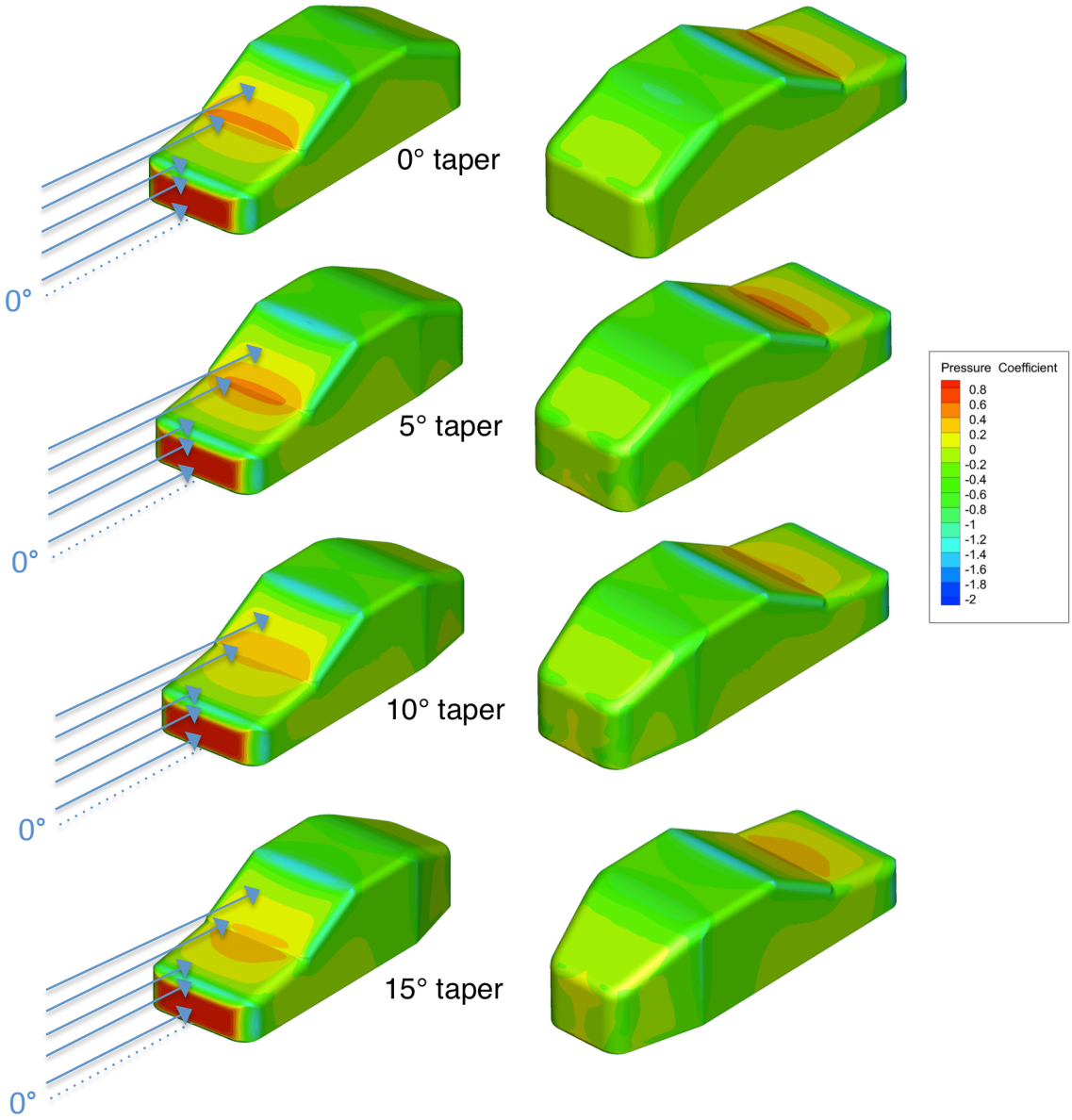

Figure 5.27: Pressure plots of 4 different tapering configurations during 0° cross-wind flow

When the taper angle increases it can be seen that the surface pressure coefficient aft of the vehicle increases, which is favorable for the drag coefficient. The higher local surface pressure coefficient results in less resistance to a forward motion of the vehicle compared to a lower local surface coefficient. From figure 5.27 it can also be seen that the surface pressure coefficient on the inclined tapered surface slightly increases, and thereby becomes less negative. Analogous to the aforementioned effect aft of the vehicle, this is also favorable for the drag coefficient.

Closer inspection on the front of the vehicle reveals that the geometry modification on the rear side also influences the flow upstream. This is indicated by the decreasing surface pressure coefficient peak at the hood - front window interface. Even though the maximum surface pressure coefficient tends to decrease for increasing taper angles, the area for which the pressure coefficient is above zero increases. The combined result of these effects are observed as the fluctuations shown in table 5.6.

Table 5.7 shows that it can be seen that during this 6 degrees cross-wind flow the drag coefficient drops substantially when an tapering modification is applied.

Aerodynamic metric	0° taper	5° taper	10° taper	15° taper
C_D	0.368	0.365	0.309	0.263
C_L	0.305	0.228	0.119	0.040
C_S	0.164	0.213	0.221	0.210
C_{Mx}	0.010	0.011	0.010	0.009
C_{My}	0.059	0.057	0.052	0.049
C_{Mz}	0.010	0.008	0.009	0.010

Table 5.7: Aerodynamic metrics for different taper angles - 6° cross-wind flow

It can be concluded that tapering the vehicle appears to be an effective measure to reduce the drag coefficient when the vehicle experiences a cross-wind flow. At the same time it does contribute to a steep increase in the side force coefficient C_S of approximately 30% for all three tapering angles. The yaw moment coefficient C_{Mz} is less affected by the tapering modification and tends to remain constant.

Similar to the symmetric 0 degrees cross-wind flow condition it can be observed that the tapering modification again influences the hood-front window interface. The frontal nose section however is not influenced by the tapering modification during any cross-wind flow. At the vehicle base a surface pressure coefficient increase can be observed within figure 5.28. This pressure recovery is an indication for a less severe vehicle wake, which results in the observed reduced drag coefficients from table 5.7.

Using the aerodynamic results in combination with the vehicle dynamics assessment conclusions can be drawn on applying a taper modification to a vehicle. The results are presented within figure 5.29 and 5.30, where it can be seen that taperering the vehicle during 3 and 6 degrees cross-wind flows reduces the cross-wind averaged drag coefficient substantially.
While the drag coefficient reduces down by 25%, the average increase in lateral displacement for electric vehicles increases by more than 8% when a taper angle of 15 degrees is used compared to the reference 0 degrees taper as shown in figure 5.29.

The conventional vehicle shows a similar performance, although an interesting difference is found between the two vehicles when 5 degrees tapering is applied.

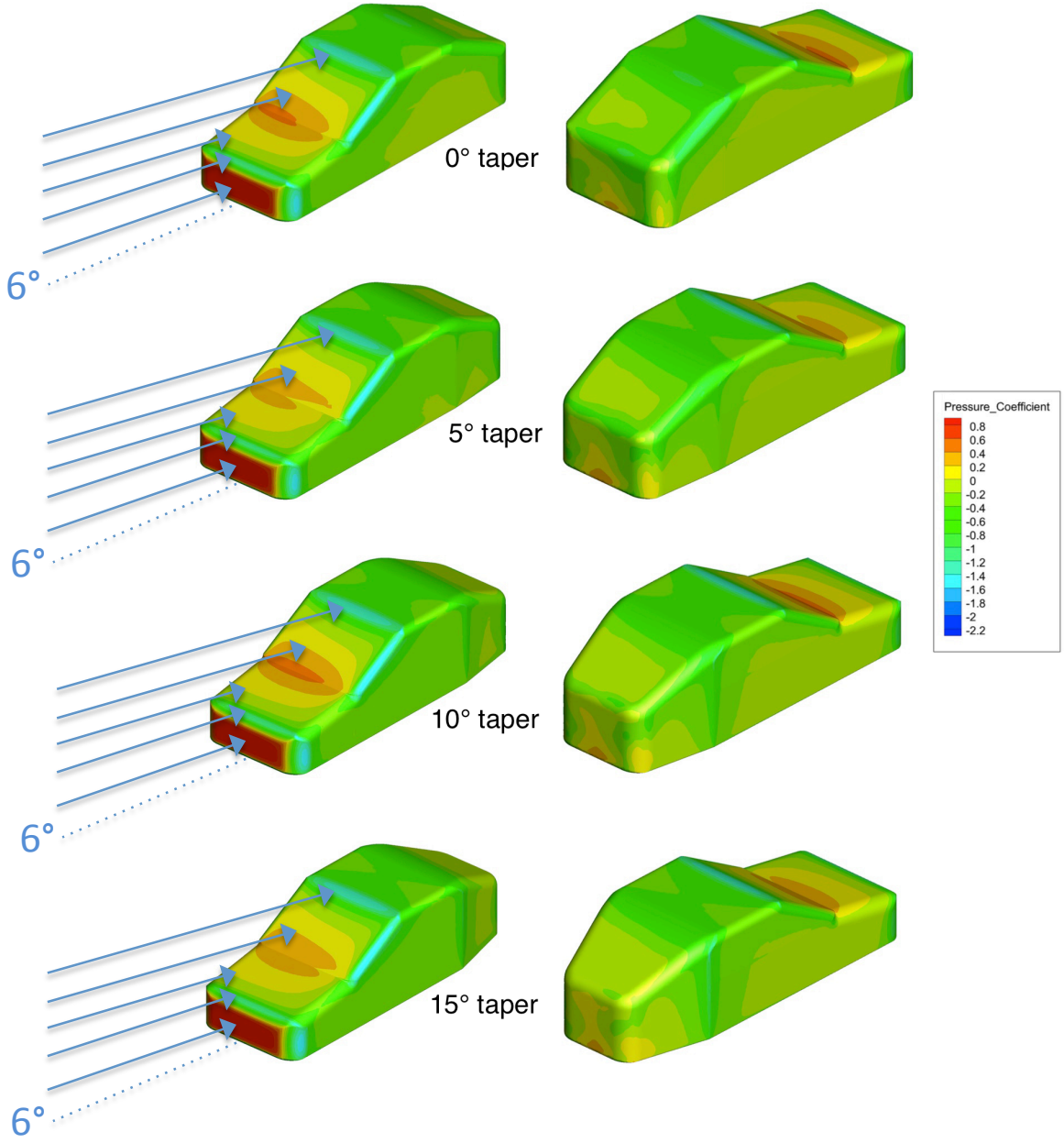

Figure 5.28: Pressure plots of 4 different tapering configurations during 6° cross-wind flow

The electric vehicle achieves a marginal improvement in lateral deviation of around 2%, whereas the conventional vehicle experiences an increase in lateral deviation of around 5%. This difference is due to the weight and weight distribution, and as was found in section 5.2 only holds for a longitudinal velocity of 30 m/s. It can be concluded that tapering has a large effect on the drag coefficient of the vehicle at the expense of a substantial increase in lateral deviation. When only these two metrics are equally important it is recommended to apply a tapering angle of 15 degrees.

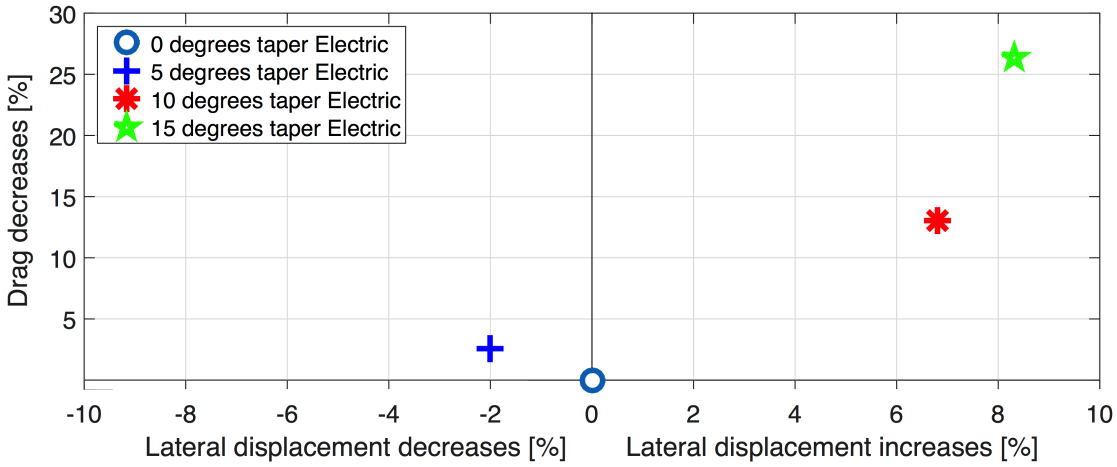

Figure 5.29: Drag coefficient and lateral displacement improvement due to tapering electro

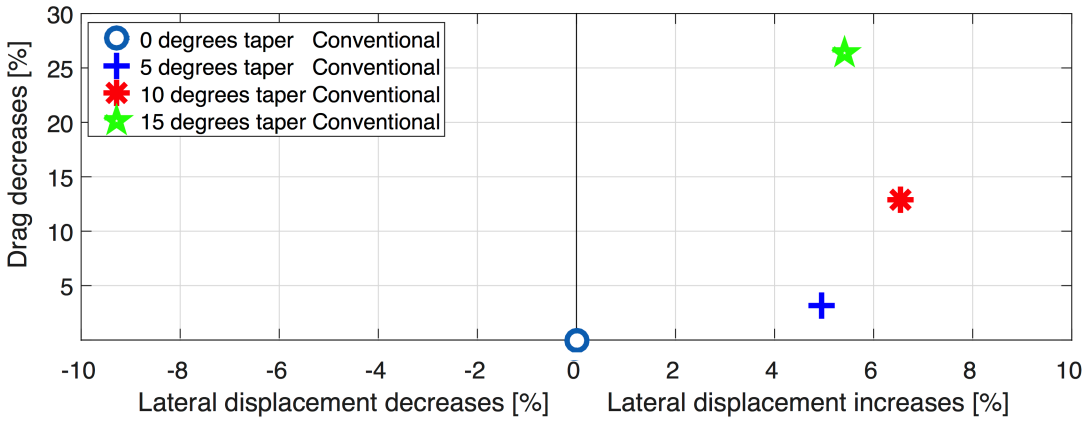

Figure 5.30: Drag coefficient and lateral displacement improvement due to tapering ICE

◇

5.5 Variations of the tumblehome angle

In this section the rear end of the vehicle is tapered as is shown in figure 5.31. This modification causes the side windows to be inclined inwards towards the center of the roof by 0, 5, 10 and 15 degrees.

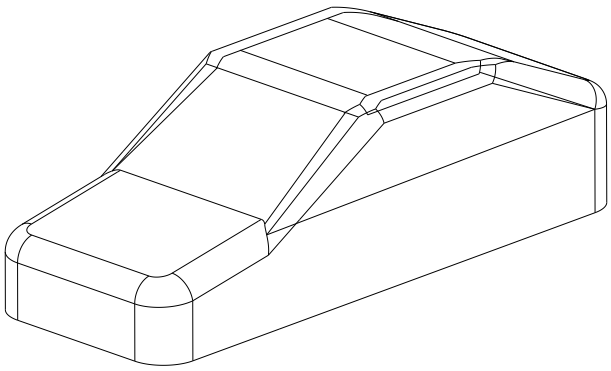

Figure 5.31: Tumblehome angle applied on the simplified vehicle geometry

As can be seen within figure 5.31, the projected surface area decreases with increasing tumblehome.Since the force and moment coefficients are linearly dependent upon the projected surface area S, it is important to use a correct frontal surface. This applies to both the aerodynamic solver, and within the MATLAB script which converts the force and moment coefficients into actual forces and moments. Analogous to the previous sections first the aerodynamic implications of the tumblehome modification are presented, followed by a lateral dynamics assessment.

A tumblehome modification affects the flow field around the roof and sidewalls and thereby the vehicle wake. From literature it became apparent that tumblehome modifications are not particularly useful for reducing the drag coefficient [55]. This conclusion is confirmed by the aerodynamic metrics presented in table 5.8 and 5.9.

Aerodynamic metric	0° TH	5° TH	10° TH	15° TH
C_D	0.251	0.249	0.252	0.253
C_L	0.224	0.213	0.213	0.208
C_S	0.000	0.000	0.000	0.000
C_{Mx}	0.000	0.000	0.000	0.000
C_{My}	0.054	0.054	0.054	0.054
C_{Mz}	0.000	0.000	0.000	0.000

Table 5.8: Aerodynamic metrics for different tumblehome angles - 0° cross-wind flow

Within table 5.8 it can be seen that almost all coefficients are close to constant for the different tumblehome angles during a 0 degree cross-wind flow. The total drag force does decrease due to the decrease in projected surface area.

Aerodynamic metric	0° TH	5° TH	10° TH	15° TH
C_D	0.368	0.399	0.389	0.364
C_L	0.305	0.304	0.281	0.237
C_S	0.164	0.168	0.171	0.181
C_{Mx}	0.010	0.010	0.010	0.009
C_{My}	0.059	0.059	0.058	0.056
C_{Mz}	0.011	0.011	0.011	0.011

Table 5.9: Aerodynamic metrics for different tumblehome angles - 6° cross-wind flow

It can be concluded that applying tumblehome is not a very useful modification in terms of reducing the drag. This is confirmed by figure 5.32, which shows the gains and losses from applying a tumblehome angle to an electric vehicle.

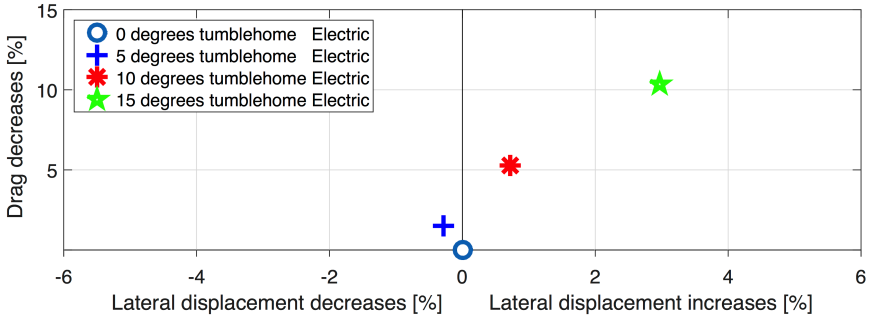

Figure 5.32: Drag coefficient and lateral displacement improvement due to tumblehome modifications applied to an electric vehicle

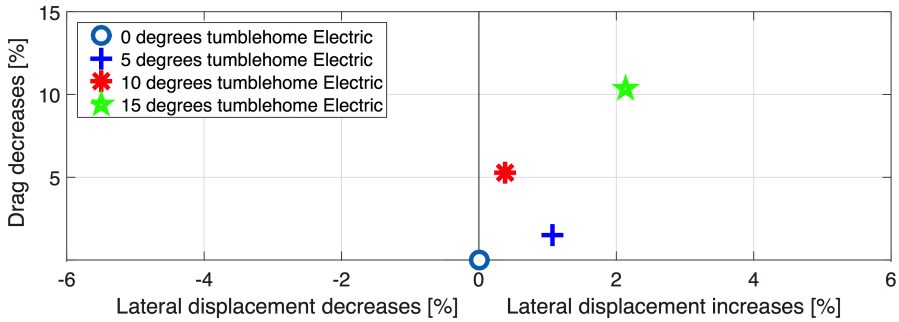

Figure 5.33: Drag coefficient and lateral displacement improvement due to tumblehome modifications applied to a conventional vehicle

It can be seen that if a reduction in lateral displacement is paramount, a tumblehome modification should generally be avoided. The averaged cross-wind flow drag coefficient however does reduce substantially when a tumblehome angle is applied, especially during asymmetric flow conditions. If reducing the drag is equally or more important than reducing the lateral deviation a tumblehome modification is therefore recommended.

◇

5.6 Variations of the front window angle

In this section the incidence angle of the front window is modified as is depicted within figure 5.34. It was chosen to study the effect of a front window angle of 25 degrees, the reference 30 and 35 degrees from the horizontal X-axis.

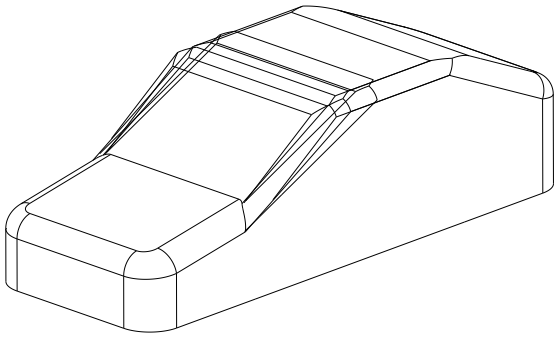

Figure 5.34: Front window angle variations on the simplified vehicle geometry

Toppinga showed that enhancing the front window angle is typically unfavorable for reducing the drag coefficient. Within the next subsection this conclusion is tested, after which the implications on the lateral dynamics are assessed. The resulting force and moment coefficients which were found from the front window variations during 0 degrees cross-wind flow are presented within table 5.10 and 5.11.

Aerodynamic metric	**Front window 25°**	**Front window 30°**	**Front window 35°**
C_D	0.241	0.251	0.299
C_L	0.230	0.224	0.292
C_S	0.001	0.000	0.002
C_{Mx}	0.000	0.000	0.000
C_{My}	0.053	0.054	0.057
C_{Mz}	0.000	0.000	0.000

Table 5.10: Aerodynamic metrics for different front window angles - 0° cross-wind flow

Aerodynamic metric	**Front window 25°**	**Front window 30°**	**Front window 35°**
C_D	0.388	0.368	0.375
C_L	0.357	0.305	0.272
C_S	0.217	0.164	0.161
C_{Mx}	0.012	0.010	0.010
C_{My}	0.063	0.059	0.058
C_{Mz}	0.007	0.011	0.011

Table 5.11: Aerodynamic metrics for different front window angles - 6° cross-wind flow

Here it can be seen that during symmetric flow conditions indeed the drag coefficient tends to decrease by 5% when a front window angle of 25 degrees is used. When

the front window angle is enhanced to 35 degrees the drag coefficient increases by around 20%. In addition it can be seen that the lift coefficient increases with increasing front window angle, which is also confirmed in Toppinga's study. [55]

Figure 5.35: Drag coefficient and lateral displacement improvement on electric vehicles due to front window angle variation

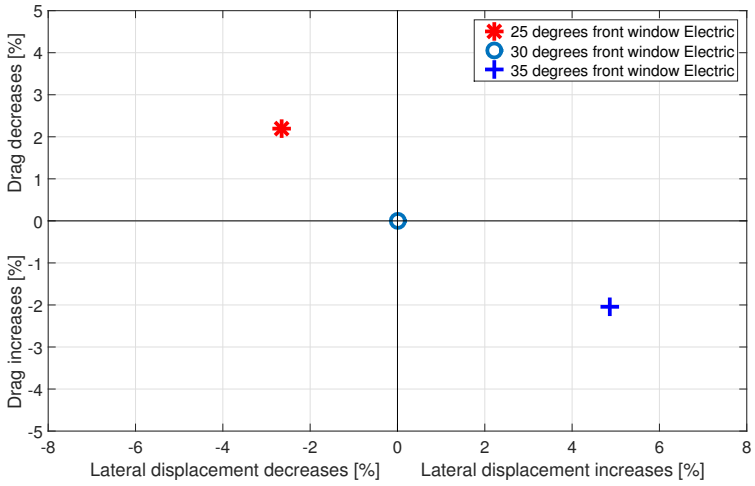

Figure 5.36: Drag coefficient and lateral displacement improvement on conventional vehicles due to front window angle variation

As can be seen from these pictures it follows that that applying a front window angle of 25 degrees is most favorable for both vehicles, where in both cases a front window angle of 35 degrees yields the an increase in both the drag coefficient and the lateral displacement.

◇

5.7 Variations of the rear window angle

In this section the rear window slant angle of the vehicle is modified as depicted within figure 5.37. It was chosen to study the effect of a front window angle of 15, the reference 20 and 25 degrees from the horizontal X-axis.

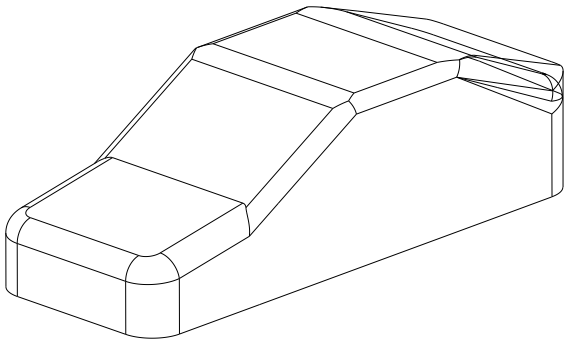

Figure 5.37: Rear window slant angle variations on the simplified vehicle geometry

The rear window slant angle is generally an important and sensitive parameter as it highly influencing the flow structures within the vehicle wake. [18] The literature also shows that this is due to the the strength of vortices originating at the C-pillars. Toppinga showed that enhancing the rear window slant angle for the SAE reference vehicle is favorable until 15 degrees, where further increases result in an increased drag coefficient. Within the next subsection this conclusion is tested from 15 degrees onwards, after which the lateral dynamics are assessed.

The aerodynamic metrics results for the symmetric flow conditions are presented in table 5.19 and 5.20.

Aerodynamic metric	Rear window 15°	Rear window 20°	Rear window 25°
C_D	0.242	0.251	0.270
C_L	0.230	0.224	0.300
C_S	0.000	0.000	0.002
C_{Mx}	0.000	0.000	0.000
C_{My}	0.053	0.054	0.057
C_{Mz}	0.000	0.000	0.000

Table 5.12: Aerodynamic metrics for different rear window angles - 0° cross-wind flow

During symmetric flow conditions the drag and lift coefficient decreases when the rear window angle is increased from 25 degrees until 20 degrees by 19 and 76 drag counts respectively. This trend is similar to the results found by Toppinga, who found a 20 and 50 counts decrease in this specific scenario. [55] A possible explanation for the discrepancy between the two lift coefficients this is that Toppinga employed a rear diffuser within his rear window angle variation simulations, which reduces the lift coefficient.

The surface pressure distribution plots together with the skin friction distributions shown in figure 5.38 provide insight in the substantial differences in drag coefficient

between the different configurations. Within the skin friction distribution on the top right of figure 5.38 it can be seen that the 15 degree rear window configuration possesses a vehicle base where the flow completely separated as indicated by the low local skin friction coefficient. Although this not desired for a low drag coefficient, it does allow for relatively weak C-pillar vortices. This is indicated by the slightly higher skin friction coefficient in the middle of the rear window compared to the other configurations.

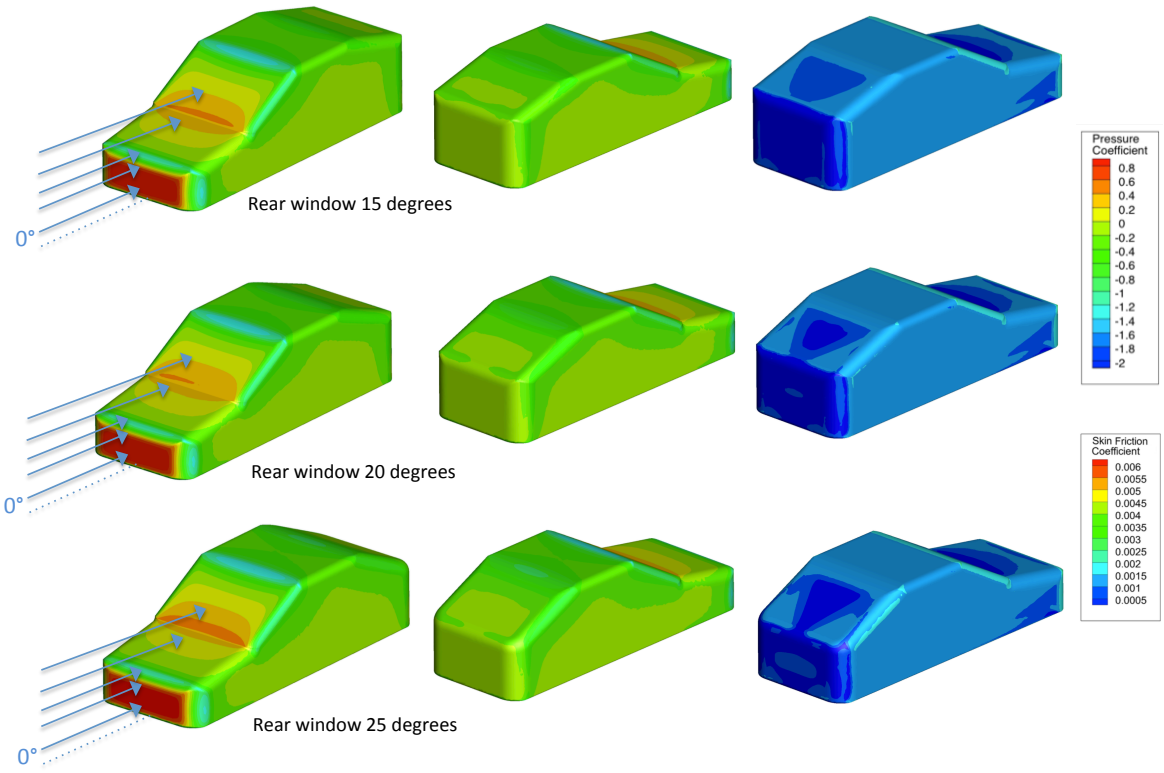

Figure 5.38: Pressure plots of 3 rear window configurations during 0° cross-wind flow

The results of the 6 degrees cross-wind flow simulations are presented in table 5.20:

Aerodynamic metric	Rear window 15°	Rear window 20°	Rear window 25°
C_D	0.299	0.368	0.375
C_L	0.067	0.305	0.263
C_S	0.217	0.164	0.161
C_{Mx}	0.011	0.010	0.009
C_{My}	0.063	0.059	0.058
C_{Mz}	0.007	0.011	0.011

Table 5.13: Aerodynamic metrics for different rear window angles - 6° cross-wind flow

Again the 15 degrees rear window configuration shows the lowest drag coefficient. Due to the enhanced side area surface of the vehicle it is more sensitive for cross-winds, which is confirmed by the high side force coefficient.

This is confirmed by inspecting the surface pressure coefficient distribution within figure 5.39, where the windward vehicle side (visible in the center vehicle in figure 5.39) indeed shows a higher pressure. Although the yawing moment coefficient C_{Mz} is reduced, the vehicle still experiences a substantial higher lateral deviation compared to the the other two configurations.

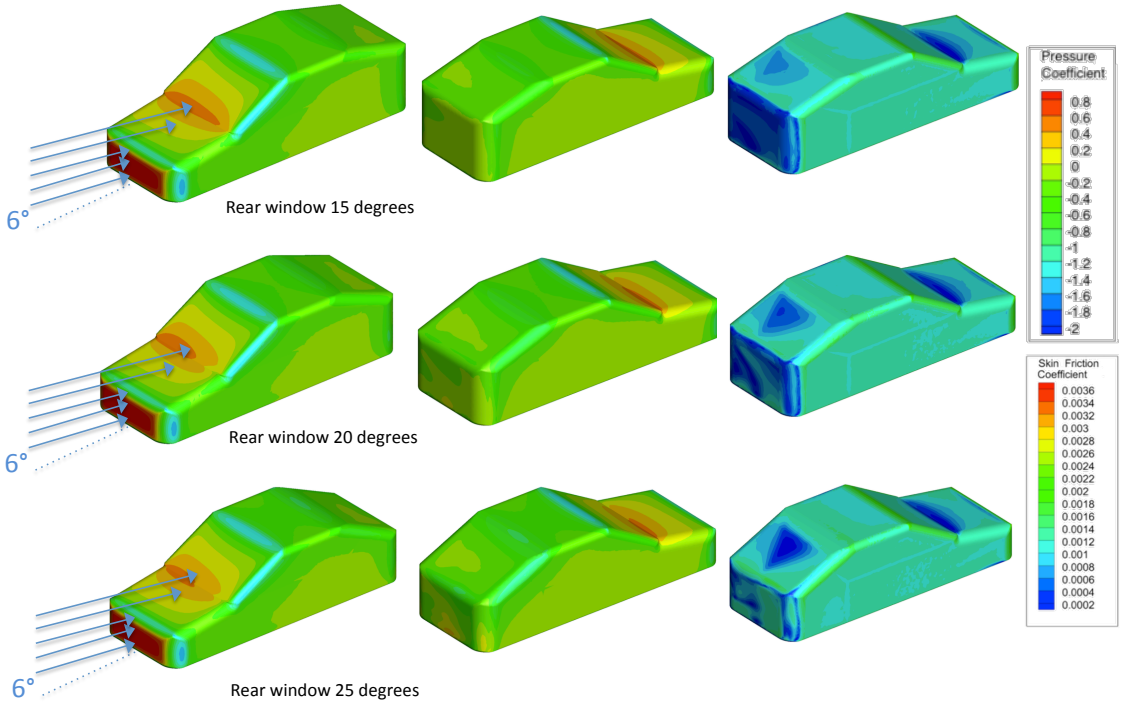

Figure 5.39: Pressure plots of 3 rear window configurations during 6° cross-wind flow

It is evident that a trade-off is well in place, given the substantial drag reduction possibilities within the rear window angle variation which come with an enhanced lateral deviation penalty. This two metrics are presented within a performance plot which is shown in figure 5.41 and 5.41. Within these two figures it can be seen that the electric vehicle has a reduced effect upon the procentual improvement in lateral deviation compared to the conventional vehicle. When lateral deviation is paramount it can be concluded that a rear window angle of 25 degrees should be maintained. In the case that reducing the drag coefficient is more desired, a 15 degrees rear window angle is recommended.

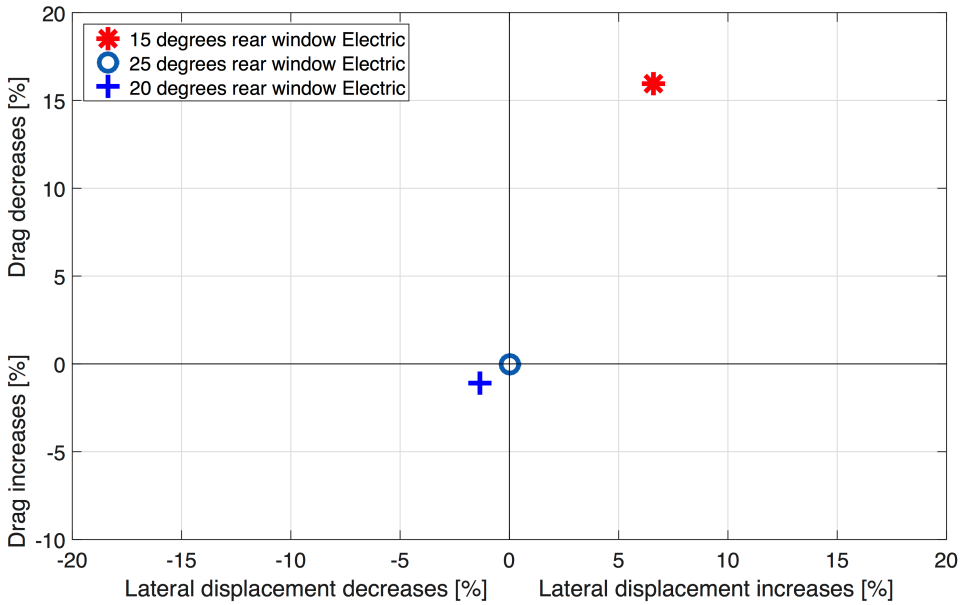

Figure 5.40: Drag coefficient and lateral displacement improvement due to rear window angle variation electric

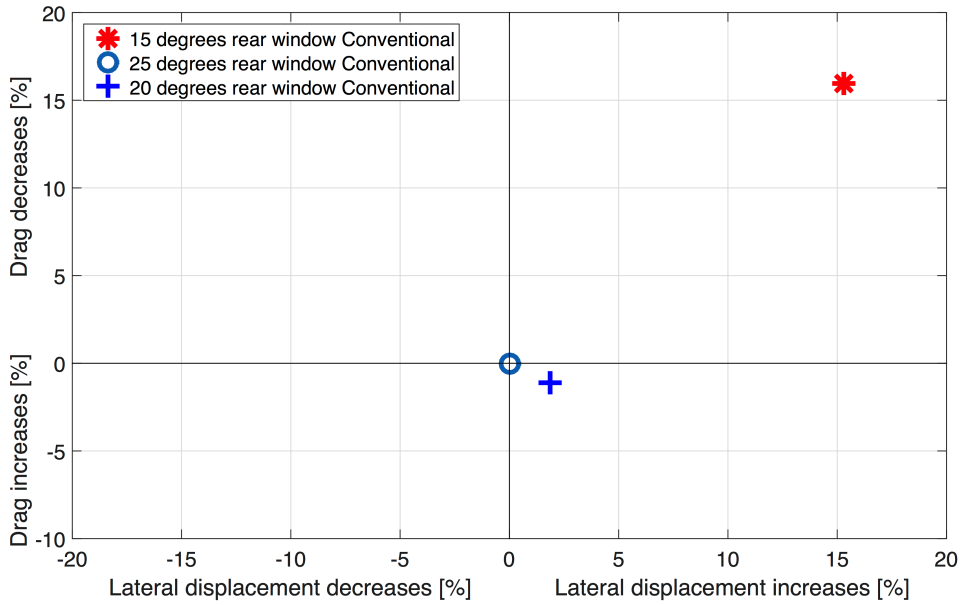

Figure 5.41: Drag coefficient and lateral displacement improvement due to rear window angle variation conventional

◇

5.8 Variations of the A-pillar radius

The effect variation of the A-pillars is studied as it is assumed that these have a substantial influence on the flow field around the upper part of the vehicle body, especially during cross-wind flows. The reference A-pillar radius is $0.10m$, the radius is decreased to $0.05m$ followed by an increase towards $0.15m$ as shown in figure 5.42:

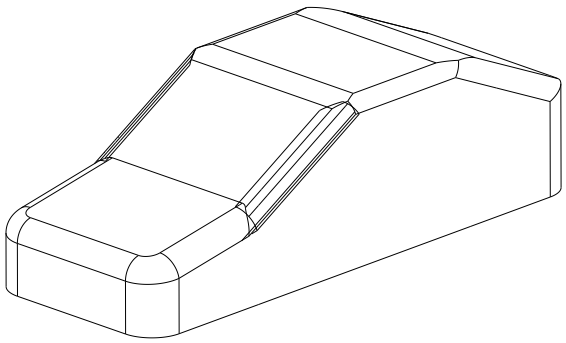

Figure 5.42: A-pillar radius applied the simplified vehicle geometry

The results from the symmetric flow condition are presented in table 5.14 and 5.20.

Aerodynamic metric	A-pillar 50 mm	A-pillar 100 mm	A-pillar 150 mm
C_D	0.255	0.251	0.251
C_L	0.145	0.224	0.243
C_S	0.000	0.000	0.002
C_{Mx}	0.000	0.000	0.000
C_{My}	0.053	0.054	0.056
C_{Mz}	0.000	0.000	0.000

Table 5.14: Aerodynamic metrics for different A-pillar radii - 0° cross-wind flow

Aerodynamic metric	A-pillar 50 mm	A-pillar 100 mm	A-pillar 150 mm
C_D	0.412	0.368	0.375
C_L	0.197	0.305	0.262
C_S	0.221	0.164	0.161
C_{Mx}	0.012	0.010	0.010
C_{My}	0.063	0.059	0.058
C_{Mz}	0.011	0.011	0.011

Table 5.15: Aerodynamic metrics for different A-pillar radii - 6° cross-wind flow

It can be concluded that the drag coefficient tends to stabilize at an A-pillar of around $0.1m$, where the A-pillar with a radius of $0.05m$ performs worse in both flow environments compared to the other two configurations. An A-pillar configuration with r = $0.05m$ also results in an enhanced side force coefficient, which is undesired for the lateral deviation. When the A-pillar radius is enhanced towards r = $0.15m$ it follows that the drag coefficient is not affected during symmetric flow conditions, whereas during cross-wind flows the drag coefficient is reduced.

In addition to the cross-wind averaged reduction of the drag coefficient, the vehicle dynamics assessment on the A-pillars revealed that the A-pillar configuration r = $0.15m$ also yielded a subtle reduction in lateral deviation. The combined results are shown per vehicle type in figure 5.43 and 5.44.

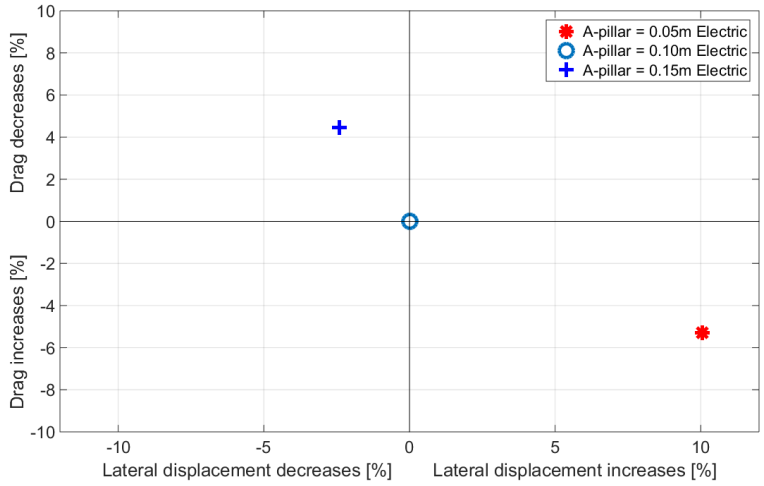

Figure 5.43: Drag coefficient and lateral displacement improvement due to A-pillar radius variation for electric vehicles

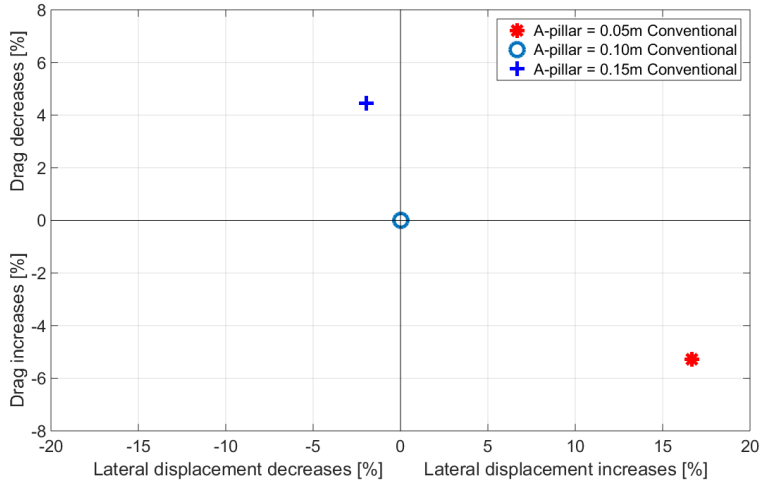

Figure 5.44: Drag coefficient and lateral displacement improvement due to A-pillar radius variation for conventional vehicles

It can be concluded that an A-pillar with a radius of r = $0.15m$ is optimal within this study.

◇

5.9 Variations of the C-pillar radius

The final shape modification which is studied is the C-pillar radii. From a reference radius of $0.15m$ the radius is changed to $0.10m$ and $0.20m$ in order to assess the impact on both the aerodynamic metrics and the resulting effect on the lateral vehicle dynamics. The C-pillar modifications are visualized within figure 5.45:

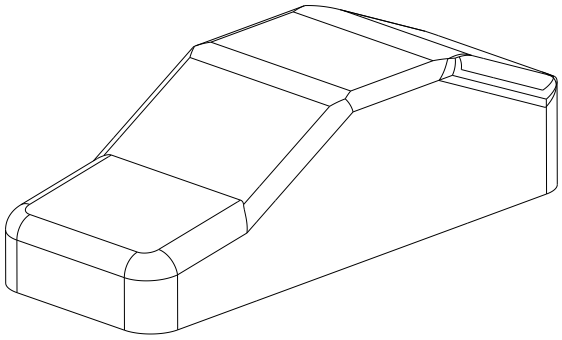

Figure 5.45: C-pillar radius applied the simplified vehicle geometry

The C-pillar radius is included since it this design feature are likely to have a substantial effect upon the formation and strength of vortices originating from the C-pillars, which in turn are important for the vehicle wake and thereby the drag coefficient. Similar to the previous sections first the aerodynamic implications are presented, followed by a lateral vehicle dynamics study.

The aerodynamic metrics results are presented within table 5.19 and 5.20.

Aerodynamic metric	C-pillar 100 mm	C-pillar 150 mm	C-pillar 200 mm
C_D	0.241	0.251	0.299
C_L	0.230	0.224	0.292
C_S	0.001	0.000	0.002
C_{Mx}	0.000	0.000	0.000
C_{My}	0.053	0.054	0.057
C_{Mz}	0.000	0.000	0.000

Table 5.16: Aerodynamic metrics for different C-pillar radii - 0° cross-wind flow

Here it can be seen that during symmetrical flow conditions the C-pillar configuration with radius r = $0.1m$ is preferred in order to reduce both the drag and the lift coefficient. The steep drag increase for a C-pillar with a radius of $0.2m$ during symmetric conditions came unexpected. The surface pressure distribution plots are shown together with a skin friction distribution in figure 5.46 in order to determine the root cause for this conclusion.

Within figure 5.46 it can be seen that in the C-pillar configuration where r = $0.1m$ the complete flow field appears to get affected. From the skin friction distribution it can be deduced that the vortices originating at the C-pillars tend to decrease in strength and become more compact, which can be seen by the widening of the low skin friction zone on the rear window. In addition to this difference in the C-pillar vortices it appears that the surface pressure on the vehicle sides slightly increases which also results in a subtle increment of the skin friction coefficient over the complete vehicle side. Contrary to these observations it appears that the pressure peak at the interface between the motor compartment and the front window decreases in magnitude which is benificial for the drag coefficient. The substantial decrement in this pressure peak is responsible for the lower drag coefficient found for the r = $0.1m$ configuration.

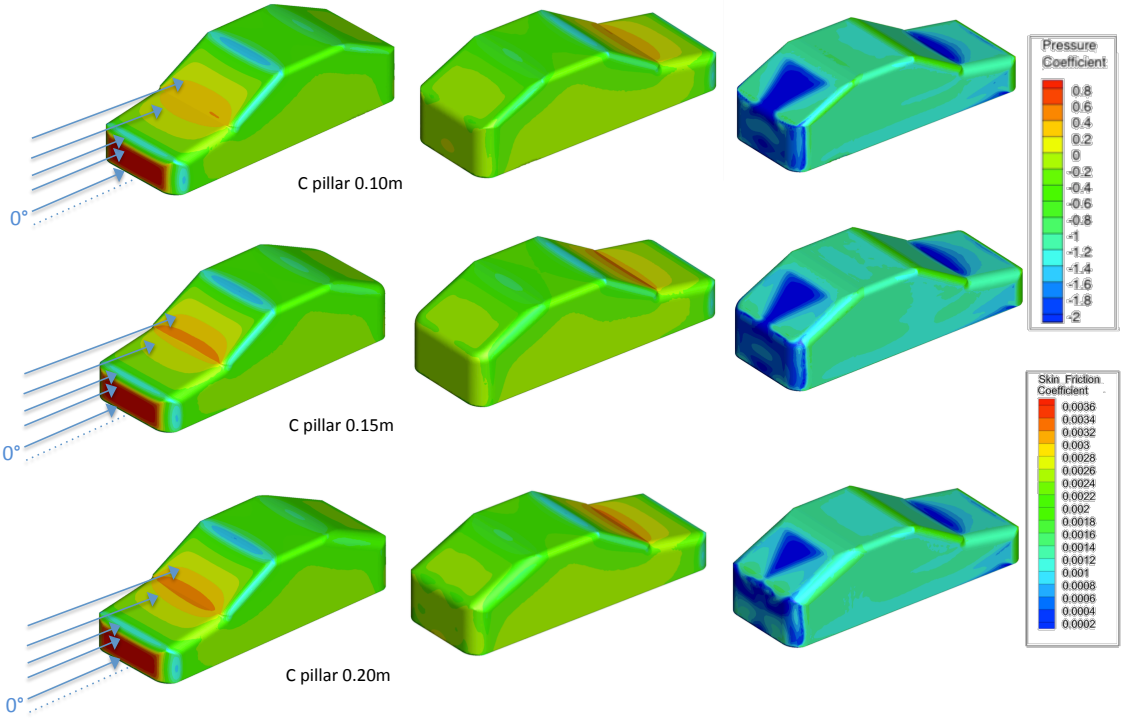

Figure 5.46: Surface pressure and skin friction distribution plots of 3 different C-pillar radii - 0° cross-wind flow

When the C-pillar configuration with r = $0.2m$ is examined it is concluded that in this case the vortices gain strength which is indicated by the relatively small area of low skin friction triangle on the rear window. The relatively high skin friction in combination with a streamline assessment reveals the presence of enhanced vortices originating from the C-pillar, which together with the enhanced pressure peak at the front window is responsible for a steep increase in the drag coefficient.

When the incident cross-wind flow angle is increased towards 6 degrees it can be seen in table 5.20 that in this case a larger C-pillar radius is actually useful for reducing the drag coefficient.

Here the configuration with r = $0.1m$ now has the highest drag coefficient.
It can be concluded that the effectiveness of the C-pillar radius for reducing the drag depends upon the cross-wind flow angle.

Aerodynamic metric	C-pillar 100 mm	C-pillar 150 mm	C-pillar 200 mm
C_D	0.434	0.368	0.375
C_L	0.357	0.305	0.263
C_S	0.217	0.164	0.161
C_{Mx}	0.013	0.010	0.012
C_{My}	0.056	0.059	0.054
C_{Mz}	0.007	0.011	0.011

Table 5.17: Aerodynamic metrics for different C-pillar radii - 6° cross-wind flow

The corresponding surface pressure distribution plots together with the skin friction distribution during 6 degrees of cross-wind flow are shown in figure 5.47:

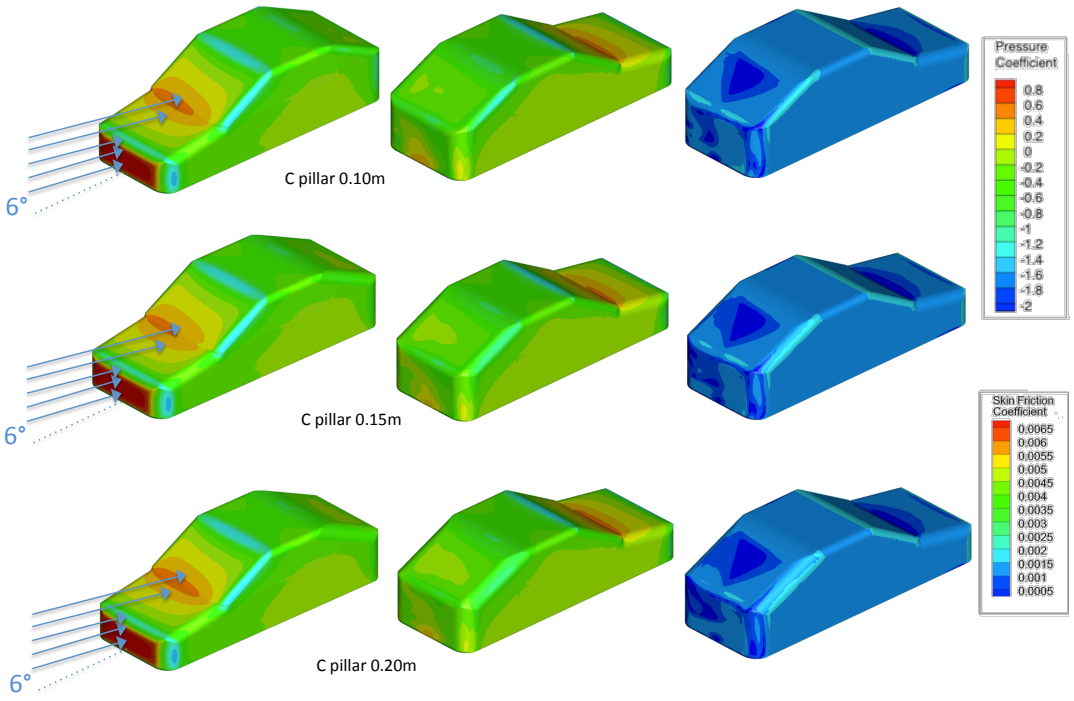

Figure 5.47: Surface pressure and skin friction distribution plots of 3 different C-pillar radii during 6° cross-wind flow

Since in this case the surface pressure distributions plots only differ aft of the vehicle, it can be concluded that during 6 degrees cross-wind flow the interaction effects with the vehicle front are less pronounced. The main differences are now only found within the wake of the vehicle caused by the difference in magnitude of the vortices originating from the C-pillars. This is concluded by examining the streamlines and the growing less negative pressure zone on the rear window of the vehicle indicated by the light green zone.

The performance plots can be created by combining ther aerodynamic results with the vehicle dynamics assessment. The performance plots are shown in figure 5.48 and 5.49 for electric and conventional vehicles respectively:

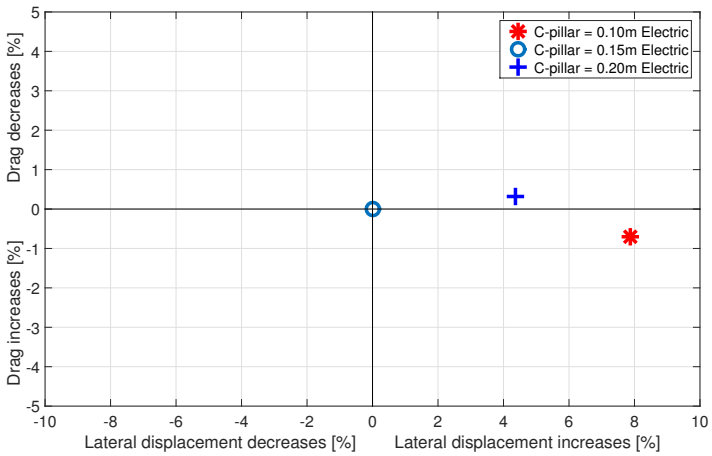

Figure 5.48: Drag coefficient and lateral displacement improvement due to C-pillar radius variation for electric vehicles

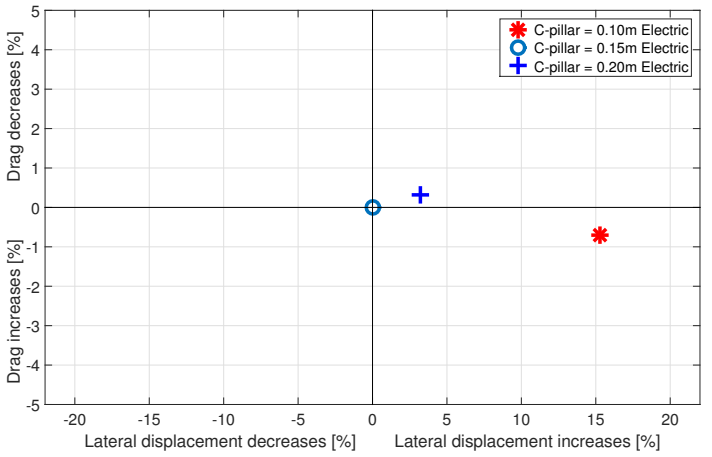

Figure 5.49: Drag coefficient and lateral displacement improvement due to C-pillar radius variation for conventional vehicles

As can be seen from figure 5.48 and 5.49 the drag coefficient reductions which are possible using a C-pillar radius of r = $0.2m$ cause the lateral deviation to increase by 8% and 16% for electric and conventional vehicles respectively. For this reason it is not recommend to modify the C-pillar radius at this point. It can be concluded that the C-pillar is an interesting design parameter which is sensitive to cross-wind.

◇

5.10 Towards an optimized vehicle geometry

The effect of individual design modifications has now been explored in terms of aerodynamic and vehicle dynamic performance. The study will be completed when the different design modifications are combined. By doing so conclusions can be drawn on their interactions, and to study the performance of the optimized vehicle geometry. In order to investigate this, the results gained in the previous sections can be used in order to work towards an optimized vehicle geometry. The optimal angles and parameters can be selected when a weight factor for the drag coefficient of 0.5 out of 1 is used. This implies that the performance of the vehicle drag is as important as the reduction in lateral displacement, resulting in a vehicle which has the properties shown in table 5.18:

Design modification	Proposed value	Unit
Arrowing angle	15	[degrees]
Tapering angle	15	[degrees]
Tumblehome angle	15	[degrees]
Front window angle	25	[degrees]
Rear window angle	15	[degrees]
A-pillar radius	0.15	[m]
C-pillar radius	0.15	[m]

Table 5.18: Optimized geometry optimal values with a drag weight factor of 0.5

The optimized vehicle geometry is presented within figure 5.50:

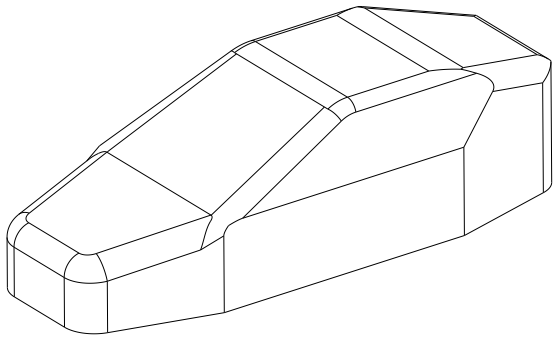

Figure 5.50: Proposed iteration of the vehicle geometry with various shape modifications

This optimized vehicle shape is simulated within SU^2, where it found that this vehicle indeed reduces the drag coefficient as can be seen in table 5.19. Using the results within this table it can be concluded that all the proposed design modifications combined together yield a drag reduction of 17%. This difference in drag coefficient indicates that the individual design modifications work well together. When the cross-wind flow angle is set to 6 degrees the difference in drag coefficient is even more pronounced as can be seen from table 5.20. A drag coefficient reduction of 43% is achieved when the design is modified using the values from table 5.18. The resulting reduction of the cross-wind flow averaged drag coefficient is 30%.

Aerodynamic metric	Baseline geometry	Optimized vehicle geometry
C_D	0.251	0.206
C_L	0.224	0.103
C_S	0.000	0.000
C_{Mx}	0.000	0.000
C_{My}	0.054	0.052
C_{Mz}	0.000	0.000

Table 5.19: Aerodynamic metrics for the reference vehicle and the optimized vehicle during 0° cross-wind flow

Aerodynamic metric	Baseline geometry	Optimized vehicle geometry
C_D	0.368	0.215
C_L	0.305	0.102
C_S	0.164	0.235
C_{Mx}	0.010	0.034
C_{My}	0.059	0.052
C_{Mz}	0.011	0.011

Table 5.20: Aerodynamic metrics for the reference vehicle and the optimized vehicle during 6° cross-wind flow

It follows that the drag coefficient between the 0 and 6 degrees cross-wind flow is substantially less sensitive to cross-wind flows, as the force and moment coefficients differ less from one another than the reference vehicles do between 0 and 6 degrees cross-wind flow. The optimized vehicle does however experience a higher side force coefficient due to the larger side surface area compared to the reference vehicle. The corresponding surface pressure distribution plots are shown in figure 5.51.

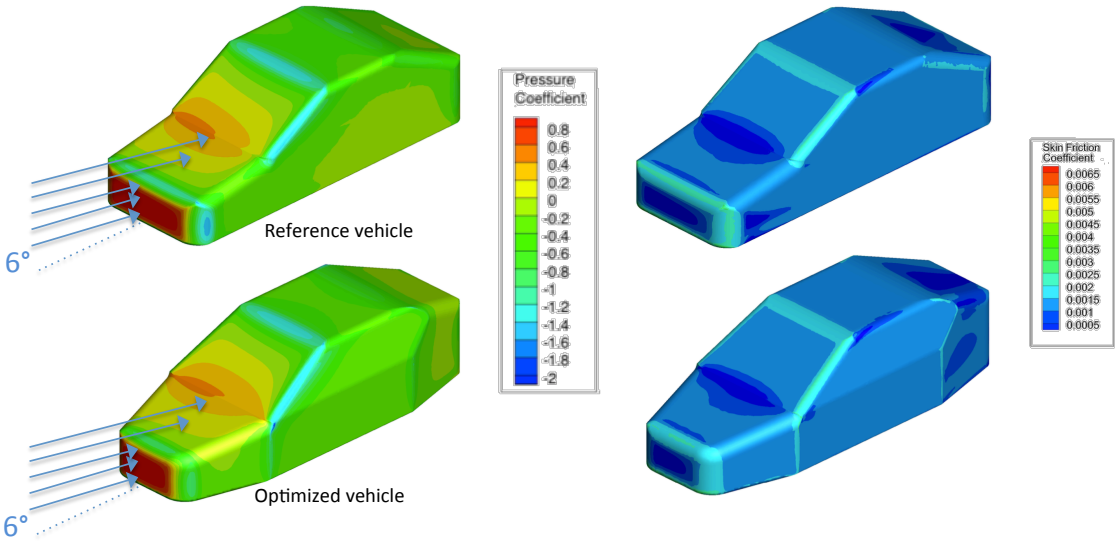

Figure 5.51: Surface pressure and skin friction distribution plots of both the reference and optimized vehicle during 6° cross-wind flow

This results in an increased overall lateral deviation of around 6% compared to the reference vehicle which is shown in figure 5.52.

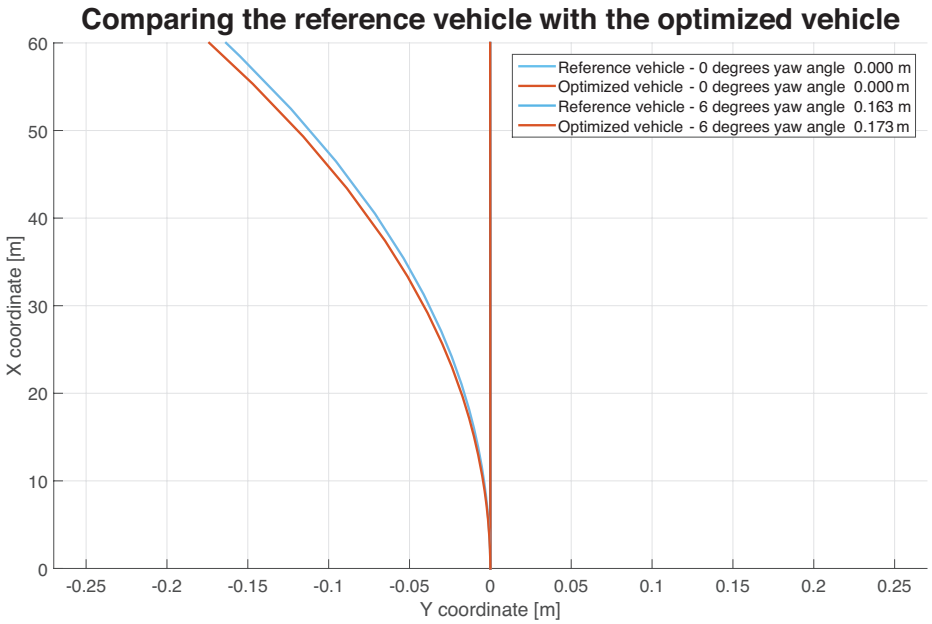

Figure 5.52: Reference and optimized vehicle trajectories with arrowing during 0° and 6° cross-wind flows

It can be concluded that the optimized vehicle is mainly optimized for reducing the drag coefficient. This was expected since the selected values for the proposed different design modifications which result from various trade-offs were mainly in favor of reducing the drag rather than reducing the lateral displacement.

Part IV

Synthesis

Chapter 6

Conclusions and recommendations

Within this report it was aimed to answer the following research question:

What design modifications reduce the drag coefficient of a simplified vehicle model which experiences a cross-wind flow, and how does this affect the lateral dynamic performance?

A simplified vehicle body design was selected for this study in order to exclude the typically complicated (interaction) effects such as wheels and their interactions with the wheel housings, and details such as windscreen wipers and mirrors. It is therefore necessary to note that the results and corresponding conclusions which are drawn within this report are only valid for identifying global trends.

This simplified vehicle was put to test in a series of digital computational fluid dynamics simulations using Stanford's open-source SU^2 software suite. The simulations are performed using a Reynolds Averaged Navier-Stokes solver, in combination with a Spalart-Allmaras turbulence modelling scheme for a cruise velocity of 30 m/s. This software suite has been validated using the SAE reference vehicles and the results reported by Toppinga. Here it was found that the difference the force coefficients results between SU^2 and STAR-CD is in the order of 5%, which was found acceptable for drawing conclusions on aerodynamic metric trends. A mesh dependence study was performed which showed no changes in the force and moment coefficients between 3 and 5 million volume cells. In addition no substantial difference in convergence speed or force and moment coefficients were reported between the Spalart - Allmaras and the SST turbulence scheme.

A vehicle dynamics study was performed which indicated that especially the side force coefficient and yaw moment coefficient are predominant metrics for assessing the lateral deviation of a vehicle during cross-wind flows. In addition to this it was found that the longitudinal position of the center of gravity, the vehicle weight, the mass moment of inertia around the Z axis I_{ZZ}, and the longitudinal velocity substantially influence the lateral deviation of the vehicle. The resulting lateral deviation is in the order of $0.2m$ after 2 seconds of experiencing a cross-wind flow of 6 degrees. This deviation is roughly similar to the situation where the steering

wheel angle is set to 1 degree during 2 seconds. It can be concluded that the lateral deviation of vehicles during cross-wind flow conditions of up to 6 degrees is not of high importance.

Experiments were designed for three different cross-wind flows; 0 degrees, 3 degrees and 6 degrees cross-wind flow for both conventional and electric vehicles. These cross-wind flows were chosen since the typical cross-wind flow which a vehicle is likely to encounter during cruise ranges up to 6 degrees. Using increments of 3 degrees provides enough data to draw conclusions on the differences in flow effects during the 0 to 6 degrees cross-wind flow.

During the results review it became evident that as was pointed out in the literature, shape modifications reducing drag are most effective aft of the vehicle. It was also found that most drag reducing design modifications typically tend to enhance the associated lateral displacement of the vehicle, which is confirmed in literature [18]. The arrowing design modification up to 10 degrees applied on the front of the vehicle appears to have a positive effect on both the drag coefficient and the lateral displacement. When one applies a tapering design modification aft of the vehicle the cross-wind averaged drag coefficient is reduced down by over 25%. Here it was found that most of these drag coefficient improvements happen when the cross-wind angle is larger than 0, i.e. the drag reducing means tend to become more effective during cross-wind flows. A summary of the optimal design modifications is presented within table 6.1. Within this table the indicated drag reduction is the averaged drag coefficient reduction during 0, 3 and 6 degrees cross-wind.

Design modification	Unit	Initial value	Proposed value	C_D reduction
Arrowing angle	[degrees]	0	15	5%
Tapering angle	[degrees]	0	15	27%
Tumblehome angle	[degrees]	0	15	10%
Front window angle	[degrees]	30	25	2%
Rear window angle	[degrees]	25	15	16%
A-pillar radius	[m]	0.10	0.15	4%
C-pillar radius	[m]	0.15	0.15	0%

Table 6.1: Summary on the effect of different design modifications on the drag coefficient

When the proposed values are applied and consequently simulated using SU^2, it was found that a cross-wind averaged drag coefficient reduction of 30% is achieved.

The vehicle dynamics conclusions are simulated using a modified bicycle model representation of a vehicle. Here the steering input has been removed, and yaw and roll stiffness and damping have been added. The model uses the aerodynamic loading in terms of forces and moments generated by the SU^2 CFD solver.

A vehicle dynamics sensitivity study has been performed to investigate the effect of the difference between an electric vehicle and a vehicle with a conventional combustion engine mass distribution. Here it can be concluded that the difference in lateral deviation between a conventional vehicle and an electric vehicle during a longitudinal velocity of $30m/s$ and 6 degrees cross-wind flow is in the order of 20%

in favor of the electric vehicle. This observation is however subject to change when the longitudinal velocity is changed. Up until $30m/s$ the electric vehicle deviates less, where at higher velocities the conventional vehicle outperforms the electric vehicle in terms of minimizing lateral deviation.

Recommendations for future studies

This study can be improved by focussing more on the aerodynamic simulations, where the reference vehicle could be more realistic by adding (rotating) wheels, cooling flow and vehicle details. In addition one could upgrade the vehicle dynamics model into a full 3-D model which could theoretically include a driver steering input. It would also be interesting to study the vehicle performance beyond 6 degrees cross-wind flow. The latter is already being investigated at the Precision and Microsystems Engineering in 3mE under the supervision of Mustafa Arat.

Part V

Appendices

Appendix A: ANSYS Meshing

This subsection discusses the meshing workflow which was used for this study.
The workflow consisted of the following listed stages:

- Construct a parameterized vehicle body
- Construct a parameterized digital control volume
- Setting the main meshing controls
- Create named selections
- Generation of the mesh
- Reviewing the mesh quality
- Improving the mesh quality

These different stages will be discussed individually on the next page.

Construct a parameterized vehicle body

Within ANSYS Design Modeler a new drawing plane was constructed which allowed for a variable angle of the plane towards the principal XZ - plane.
The vehicle side view was drawn inside this new plane because the incident plane angle could be easily varied in order to obtain an incident cross-wind flow angle of $\beta = 0$, 3 and 6 degrees.
The same vehicle geometry is displayed in the ANSYS environment in figure 6.1:

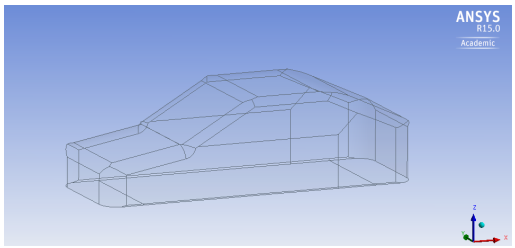

Figure 6.1: Model of the Tesla geometry inside ANSYS Meshing

Construct a parameterized digital control volume

With the vehicle geometry defined a control volume needs to be created in order to define the boundaries of the to be simulated digital domain. This control volume needs to be sufficiently large to capture the most relevant flow phenomena, but increasing the volume will increase the computational expense.

Typical control volumes which are used for vehicles extend 4 car lengths in the longitudinal direction, and advance the vehicle approximately 2 car lengths. [55] Furthermore it is advised to to have 3 car lengths to either side perpendicular to the flow direction, and use 2 car lengths in the vertical Z- direction.[55].

The ground surface of the control volume was set at a height of 200mm underneath the vehicle shape in order to simulate a realistic duct underneath the vehicle.

Once the control volume has been established, it is good practice to perform a boolean subtract operation. [4] This means that the vehicle body volume is subtracted from the control volume, creating a void in the shape of a vehicle inside the square control volume. This is done in order to conveniently assign the boundary walls using named selections. These named selections can then be used in the CFD solver to indicate the required behaviour of the vehicle surface, the road and the walls of the control volume.

The result of the boolean subtract operation can be seen in figure 6.2:

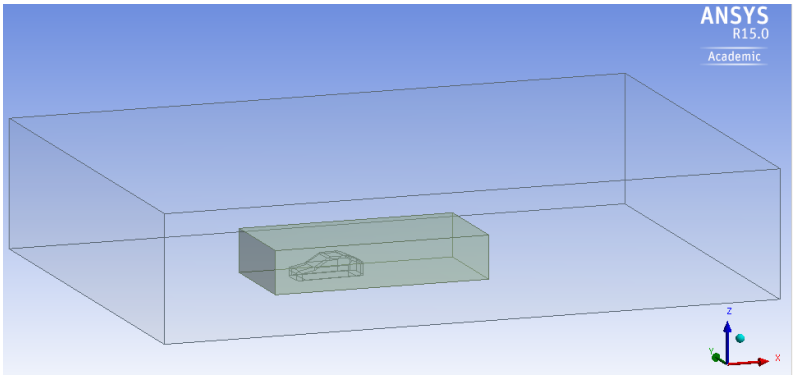

Figure 6.2: Digital control volume with the vehicle geometry inside

The dimensions of the computational domain with respect to the origin which is at the rear base of the vehicle, 200mm below the vechile are as follows:

$[X_{min}, X_{max}]$ = [-14m, 16m] in the longitudinal direction

$[Y_{min}, Y_{max}]$ = [-12m, 12m] in the longitudinal direction

$[Z_{min}, Z_{max}]$ = [0m, 4m] in the longitudinal direction

The vehicle body has a frontal area of $1.5 \cdot 1.19 = 1.785m^2$, which results into a blocking ratio of 0.0119.

Setting the main meshing controls

ANSYS Meshing has main a mesh control menu which features the predominant mesh control parameters. This menu is shown in figure 6.3:

Details of "Mesh"	
Defaults	
Physics Preference	CFD
Solver Preference	Fluent
Relevance	0
Sizing	
Use Advanced Size Fu...	On: Proximity and Curvature
Relevance Center	Coarse
Initial Size Seed	Active Assembly
Smoothing	High
Transition	Fast
Span Angle Center	Fine
Curvature Normal ...	12.0 °
Proximity Accuracy	0.5
Num Cells Across Gap	5
Growth Rate	1.20
Inflation	
Use Automatic Inflation	Program Controlled
Inflation Option	First Layer Thickness
First Layer Height	5.e-005 m
Maximum Layers	20
Growth Rate	1.2
Inflation Algorithm	Pre

Figure 6.3: Meshing control settings used in ANSYS Meshing

ANSYS Meshing offers three predefined automatic mesh controls - coarse, medium and fine. When the user selects either one of these three automatic mesh control functions automatically pre-sets most options.
From literature it was found however that it is advised to set all parameters individually for additional insight and control over the mesh. [4]

Since all options are set manually, this subsection aims at explaining the most important mesh control settings which are shown in figure 6.3.

The Physics preference should be set to CFD, as the study at hand does not require Finite Element Analysis (FEA). FEA only needs to be selected when strength and deformation analysis is desired.
The solver preference does not need to be Fluent as is indicated in the figure, as the mesh will be exported using a .cgns extension. The relevance center is only useful when the user selects either one of the three pre-defined mesh control settings.

Sizing parameters of the mesh

The sizing settings address the sizing of the control points within the mesh, and determine how the mesh should deal with the geometry.

The fist option concerns the advanced sizing function, which can be set to off, proximity, curvature or the combination of proximity and curvature.
During trial and error it was found that the latter yielded better mesh results in terms of additional control point density at regions of additional interest, i.e. the entire vehicle body and areas with steep gradients of the vehicle contour.

Using the relevance center setting the user can select any of the three pre-defined mesh controls - coarse, medium and fine as was discussed on the previous page.

When certain suppressed or hidden features within the assembly need to be included within the mesh the user can use the initial size seed.
For this study this function is not used.

The smoothing can be set to low, medium or high. Again using trial and error it was found the the high smoothing factor results in a higher quality mesh.
Within the subsection *Improving the mesh quality* it is explained how the quality of the mesh can be assessed.

Depending upon which method is used for constructing the mesh it may be relevant to specify an either slow or fast transition of which the rate of adjacent elements will grow. This will again have an effect on the mesh quality metrics. From literature it was found that a slow transition is better suited for CFD calculations [4]

Instead of using the advanced size function the user can specify the span angle center in order to manually create curvature based refinement for edges.
This option is not used within this study because an advanced size function method is used.

ANSYS Meshing default value for curvature normal angle is equals to 12 *degrees* as default value, which from literature is found suitable for vehicle geometries [4]. Changing this value to lower values did not have any effect on the mesh quality metrics, hence for this geometry it is assumed that the default value is sufficient.

The proximity accuracy controls the search range with the maximum size of the distance between two control points and the amount of cells between any gap. Here a setting of 1 is more accurate, but a value of 0 yields faster results.
The default value 0.5 yielded a similar mesh quality compared to the setting this option as 1, therefore 0.5 is used within this study.

Between the vehicle and the ground there is a gap of approximately 200mm. Using the setting *Num cells across gap* the amount of cells in between this gap can be defined. For CFD simulations at least 5 cells between this gap is advised [4].

Using the next 4 settings it is possible to set the global minimum and maximum distances and face sizes between control points. It is good practice to keep both the min/max face size and min/max size identical as is depicted in figure 6.3.
This value can be modified to control the global control point density.

The minimum edge length can be modified to specify the minimum edge length any edge should possess in order to be recognised as an edge. Once an edge is recognised as an edge it can be incorporated within edge sizing functions. This feature is not used within this study.

Inflation layer

Within the next tab all parameters relevant to the inflation layer(s) can be set. An inflation layer is used in order to simulate the flow properties in close proximity to various walls, such as the road and near the vehicle body. This is because the structured high aspect ratio cells which are generated within inflation layers are able to capture the flow within the boundary layer more proficient than would be the case when inflation layers are excluded [4].
Within literature it was found that when using ANSYS Meshing the optimal settings for the inflation layer for vehicle purposes is the first layer thickness with the variables that are listed in figure 6.3.[4]

Create named selections

With the mesh controls now set, it is necessary to create named selections such that the CFD solver can handle the mesh correctly. Named selections are predominantly used to specify specific surfaces, such that different wall behavior can be assigned to the surfaces.
Examples of wall behavior includes wether or not the surface is eligible for heat transfer, allows for viscous effects etc.

Some surfaces are not necessarily walls, but need to be named anyways. This is especially true for e.g. the flow inlet, and the flow outlet. The CFD solver needs to know where these surfaces are in order to perform a correct simulation of the flow.

One can name each individual surface of the vehicle geometry separately for the case that different wall behaviors is desired for different body surfaces.
This could potentially yield more accurate results, but is not applied in this study. This is done mainly in order to reduce the complexity of the mesh, and to start off relatively simple.
Therefore all vehicle surfaces have the same wall behavior and all surfaces together define the vehicle body.

Generation of the mesh

Once the mesh controls are set, and the named selections are defined it is possible to create the first preliminary mesh.
A typical result for the study at hand is shown in figure 6.4:

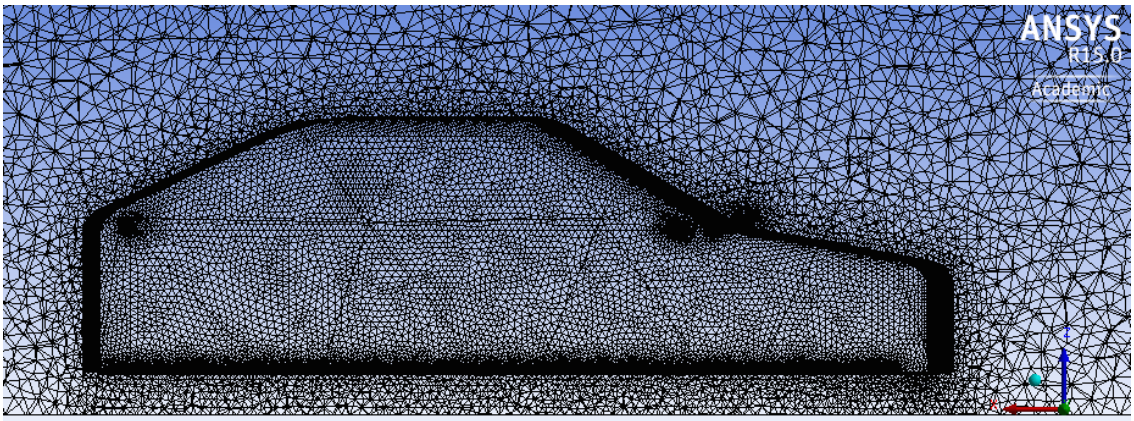

Figure 6.4: Result of the mesh

Improving the mesh quality

The obtained preliminary mesh can be tailored according to the needs of the simulation. For the study at hand it is relevant that the flow around and aft of the vehicle is captured correctly. In order to ensure that this will be the case there are various options. The most obvious choice would be to increase the number of control points to an extent that there is no need for a refinement anywhere. This would however inherently increase the computational resources. Therefore it is more efficient to tailor the mesh where it is most necessary.
This can be achieved by a feature that is available within ANSYS meshing called custom mesh sizing. The custom mesh sizing can be applied to both a body or towards a surface. Both options are discussed within the next paragraph.

Assigning mesh sizing

In order to indicate a zone where additional resolution is required due to the formation of a complex wake flow structure, creating a body of influence around the close vicinity is a good practice [4]. In this specific example the body of influence extends two vehicle volumes downstream of the vehicle, and one vehicle length up front. Furthermore it was chosen to extend the body of influence one halve of a vehicle length to both sides of the vehicle, resulting in a box shaped body as is depicted in figure 6.5.
The importance of a body of influence becomes apparent when a specific sizing of the distance between the control points within this volume is assigned. This allows for constructing a more dense population of control points which ensures that the

relevant flow phenomena are better captured.
The higher density of control points within the mesh is depicted on the right side of figure 6.5:

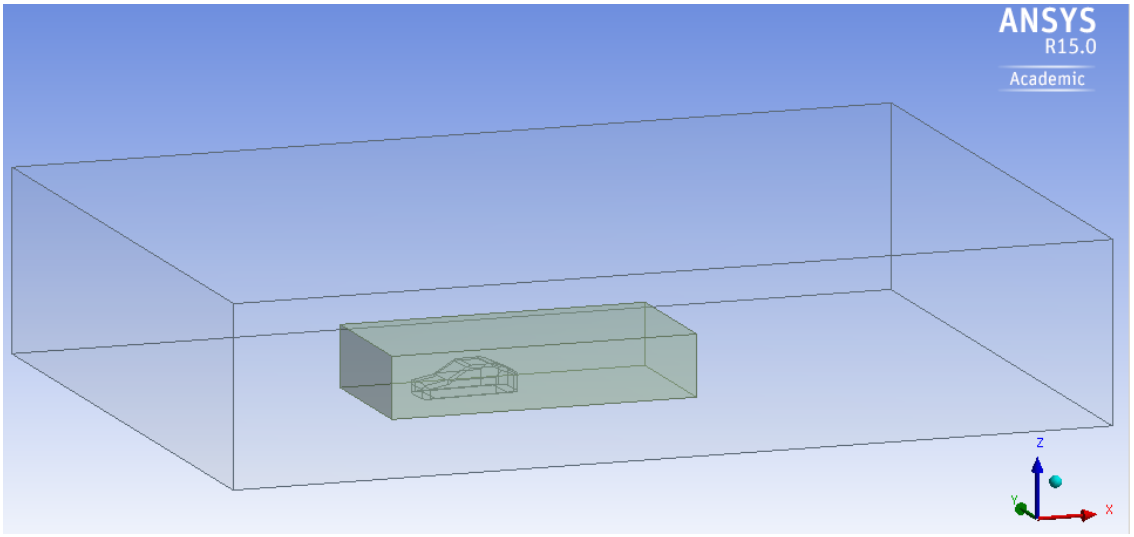

Figure 6.5: Implementing a body of influence for local higher resolution of the mesh

References

[1] Ahmed, S. R., Ramm, G. and Faltin, (1984). *Some salient features of the time-averaged ground vehicle wake*. SAE Special Publication 569, 131.

[2] Alam, F. (2000), *The effects of car a-pillar and windshield geometry on local flow and noise*. Masters thesis, RMIT University.

[3] Anderson Jr., J. D. (2007), *Fundamentals of Aerodynamics*. 4th (international) edition, McLITGraw-Hill. ISBN: 007-125408-0.

[4] ANSYS - Meshing Product documentation

[5] Vehicle Dynamics A course lecture slides - M.A. Arat, 3Me, TU Delft

[6] ANSYS - Fluent. Accessed on 15 october 2014.
http://www.ansys.com/Products/Simulation+Technology/Fluid+Dynamics/Fluid+Dynamics+Products/ANSYS+Fluent

[7] Biancolini, M. E. (2007), *Evaluation of aerodynamic drag of go karts by means of coast down tests and CFD analysis*.
University paper, Department of Mechanical Engineering, University of Rome

[8] Bodeen, C., Accessed on 10 september 2014. *Commerical applications of x-plane - part two. http:// forums.x-plane.org/index.php?showtopic=54758*.

[9] Buchheim, R., Maretzke, J., Piatek, R. (1985),
The control of aerodynamic parameters influencing vehicle dynamics. SAE paper 850279

[10] Cable, M. (2009), *An Evaluation of Turbulence Models for the Numerical Study of Forced and Natural Convective Flow in Atria* .
MSc thesis, Queen's University Kingston, Ontario, Canada.

[11] Cairns, R. S. (1994), *Lateral aerodynamic characteristics of motor vehicles in transient crosswinds*. Doctoral Thesis Cranfield University.

[12] CFD-online forums. Accessed on 25 october 2014.
http://www.cfd-online.com/Forums/su2/127445-tool-convert-openfoam-mesh-su2-mesh-2d-3d.html

[13] CFD-online forums. Accessed on 20 october 2014.
http://www.cfd-online.com/Wiki/K-omega_models

[14] Cogotti, A. (1998), *parametric study on the ground effect of a simplified car model*. SAE Special Publication paper number 980031.

[15] EADE European Aerodynamic Data Exchange (2008),
BMW AG - 320i: Sedan and Station wagon. Chart No 229 and 236.

[16] Edgar, J. (2008), Accessed on 5 September 2014
Analysis road car drag, http://www.autospeed.com/cms/article.html?title=Analysing-Road-Car-DragA=110351.

[17] Braun, M., Lanfrit, M. and Cokljat, D. (2001), *Simulation of the ahmed body.* 9th ERCOFTAC / IAHR Workshop on Refined Turbulence Modeling.

[18] Favre, T. (2011), *Aerodynamics simulations of ground vehicles in unsteady crosswind*. Doctoral Thesis KTH Stockholm, Sweden

[19] Fokker, A.D. (2015), *Investigating the drag sensitivity of a generic road vehicle shape in cross-wind flow*. MSc Literature Study, Delft University of Technology

[20] Gerritsma, M. (2002), *Computational fluid dynamics, Course Reader CFD I.* Aerospace Engineering of Delft University of Technology

[21] Gilhaus, A.M., Renn, V.E. (1986), *Drag and driving-stability-related aerodynamic forces and their interdependence results of measurements on 3/8-scale basic car shapes*. SAE Technical Paper Series. 860211.

[22] Guilmineau, E. (2008), *Computational study of flow around a simplified car body.* Journal of Wind Engineering and Industrial Aerodynamics 96, 12071217.

[23] Haruna, S., Nouzawa, T., Kamimoto, I. and Hiroshi, S. (1990), *An experimental analysis and estimation of aerodynamic noise using a production vehicle.*
SAE Paper number 900316.

[24] Heft, A. I., Indinger, T. and Adams, N. (2012), *Introduction of a new realistic generic car model for aerodynamic investigations*. SAE Paper number: 900316.

[25] Howell, J.P. (1993), *Shape features which influence crosswind sensitivity.*
The Institution of Mechanical Engineers, IMechE 1993-9, Vehicle Ride and Handling.

[26] Hucho, W.-H. (1994), *Aerodynamik des Automobils.*
3th edn, Vieweg und Teubner Verlag. ISBN: 3-18-400970-X.

[27] Hucho, W.-H. and Sovran, G. (1993), *Aerodynamics of road vehicles.*
Annual Review of Fluid Mechanics 25(1), 485537.

[28] Katz, J. (2009), *Race Car Aerodynamics: Designing for Speed.* Bentley Publishers, ISBN: 0-8376-0142-8

[29] Klasson, J. (2001), *A generalised crosswind model for simulation purposes.* Vehicle System Dynamics, 37:350359.

[30] Kloek, L.J.R. (2012), *A validation study on the rooftop flow behaviour of road vehicles.* MSc thesis TU Delft

[31] Körner, C. (2006), *Parallel Lattice Boltzmann Methods for CFD Applications.* University of Erlangen, Germany.

[32] Launder, B. E. and Sharma, B. I. (1974), *Application of the energy dissipation model of turbulence to the calculation of flow near a spinning disc.* Letters in Heat and Mass Transfer 1, 131137.

[33] Lienhart, H., Stoots, C. and Becker, S. (2002), *Flow and turbulence structures in the wake of a simplified car model (Ahmed model).* Notes on Numerical Fluid Mechanics 77, 323330.

[34] Liu, Y. and Moser, A. (2003), *Numerical modeling of airflow over the Ahmed body.* Proceedings of the 11th Annual Conference of the CFD Society of Canada pp. 507512.

[35] Macadam, C. C. (1990), *Crosswind sensitivity of passenger cars and the influence of chassis and aerodynamic properties on driver preferences.* Vehicle System Dynamics, 19 (1990). pp. 201-236.

[36] Menter, F. (1994), *Two-equation eddy-viscosity turbulence models for engineering applications.* AIAA 32(8), 15981605.

[37] Moin, P. (2002), *Advances in large eddy simulation methodology for complex flows.* International Journal of Heat and Fluid Flow 23(5), 710720.

[38] Milliken, W. F. (1995), *Race car vehicle dynamics.* SAE. ISBN: 1-56091-526-9.

[39] Murad, N. M. (2009), *Computational fluid dynamics (CFD) of vehicle aerodynamics and associated acoustics.* Doctoral thesis, Swinburne University of Technology.

[40] NPARC Alliance, Tutorial on CFD verification and validation.

[41] Othmer, C. (2006), *CFD and shape optimisation with adjoint methods.* VDI Internationaler Kongress Fahrzeug- und Verkehrstechnik. Volkswagen AG.

[42] Palacios, F. et al (2013), *Stanford University Unstructured (SU2): An open-source integrated computational environment for multi-physics design and simulations.* Stanford University, Stanford, CA.

[43] Palin, R D'Hooge, A. Rebbeck, L. (2014), *Alternative Simulation Methods for Assessing Aerodynamic Drag in Realistic Crosswind.* Tesla Motors entry in MyTechZone symposium, SAE.

[44] Páscoa, J. et al (2012), *An innovative experimental on-road testing method and its demonstration on a prototype vehicle.*
Journal of Mechanical Science and Technology 26 (6) (2012) 1663 1670.

[45] Peiró, J. *FDM, FEM and FVM methods for partial differential equations.*
University paper, Department of Aeronautics, Imperial College, London, UK

[46] Raemdonk, G. M. (2012), *Design of Low Drag Bluff Road Vehicles.*
Doctoral Thesis TU Delft, The Netherlands

[47] Mark Green (2013), Human reaction time study.
Website: http://www.visualexpert.com/Resources/reactiontime.html

[48] Roache, P. J. (1998), *Verification and Validation in Computational Science and Engineering.* Hermosa Publishers. ISBN: 0-913478-08-3.

[49] Scarano, F. (2007), *Experimental aerodynamics.* Course reader, TU Delft.

[50] Sims-Williams, D. (2011), *Cross winds and transients: Reality, simulations and effects.* SAE Technical Paper Series. 2011-01-0172.

[51] Smagorinsky, J. (1963), *General circulation experiments with the primitive equations.* Monthly Weather Review, 91(3), (1963), 99165.

[52] Strachan, R., Knowles, K. and Lawson, N. (2007), *The vortex structure behind an Ahmed reference model in the presence of a moving ground plane.*
Experiments in Fluids 42, 659 669.

[53] FKFS Stuttgart. Accessed on 10 october 2014. *Aeroacoustics vehicle wind tunnel. http://www.fkfs.de/english/automotive-engineering/wind-tunnel-operation/technical-data/.*

[54] Tamai, G. (1999), *The Leading Edge: Aerodynamic Design of Ultra-Streamlined Land Vehicles.* 1st edn, Bentley Publishers. ISBN: 0837608600.

[55] Toppinga, R. (2012), *Development of a digital aerodynamic modular model for road vehicles.* MSc thesis, TU Delft.

[56] Wickern, G. (2011), *Drag coefficients of the Audi A4 Salon, Audi A4 Avant and the Audi A5 Sportback.* Audi AG.

[57] Wilcox, D. C. (1994), *Turbulence Modeling for CFD.* DCW Industries.

[58] Wojciak, J. D. (2012) *Quantitative Analysis of Vehicle Aerodynamics during Crosswind Gusts.* Doctoral thesis TU München,Germany.

[59] Xiaolong, Y., Kaiyao, H., Tieping, L. and Jia, Y. (2011), *Effect of turbulence model on simulation of trailing vortex around ahmed body.*
Applied Mechanics and Materials 52-54, 1905 1910.

[60] Zhang, X., Toet, W. and Zerihan, J. (2006), *Ground effect aerodynamics of race cars.* Applied Mechanics Reviews 59(1-6), 3349.